Problèmes inverses, application à la reconstruction compensée en mouvement en angiographie rotationnelle X

Alexandre Bousse

▶ **To cite this version:**

Nº d'ordre : 3859

THÈSE

présentée devant

L'UNIVERSITÉ DE RENNES 1

pour obtenir

le grade de : DOCTEUR DE L'UNIVERSITÉ DE RENNES 1

Mention : TRAITEMENT DU SIGNAL ET TÉLÉCOMMUNICATIONS

par

Alexandre BOUSSE

Équipes d'accueil :	LTSI - Unité INSERM UMR 642, Rennes, FRANCE
	LIST, Université du Sud-Est, Nankin, CHINE
	CRIBs, Laboratoire International Associé
École doctorale :	MATISSE
Composante universitaire :	UFR STRUCTURE ET PROPRIÉTÉ DE LA MATIÈRE

Problèmes inverses,

application à la reconstruction compensée en mouvement

en angiographie rotationnelle X

soutenue le 12 décembre 2008 devant la commission d'examen

Président :	J. DEMONGEOT	Pr, Université Joseph Fourier, Grenoble, FRANCE
Directeurs :	J.-L. COATRIEUX	Dir. Rech. INSERM, Rennes, FRANCE
	H. SHU	Pr, Université du Sud-Est, Nankin, CHINE
	C. TOUMOULIN	MCU, Université de Rennes 1, Rennes, FRANCE
Rapporteurs :	J. YANG	Pr, Université des Sciences et des Technologies de Nankin, Nankin, CHINE
	C. ROUX	Pr, TELECOM Bretagne, Brest, FRANCE
Examinateurs :	L. LUO	Pr, Université du Sud-Est, Nankin, CHINE
	D. XIA	Pr, Université des Sciences et des Technologies de Nankin, Nankin, CHINE

Visita interiora terrae, rectificandoque, invenies occultum lapidem.

Maxime maçonnique

Remerciements

Je tiens tout d'abord à remercier Lotfi Senhadji, directeur du LTSI (Laboratoire du Traitement du Signal et de l'Image), et Limin Luo, directeur du LIST (Laboratory of Image Science and Technology), et par ailleurs codirecteur du CRIBs (Centre de Recherche en Information Biomédicale, Laboratoire International Associé), de m'avoir accueilli et pour la confiance et la liberté qu'ils m'ont accordées. Ceci est d'autant plus vrai que cette thèse s'est déroulée dans un contexte international.

Je remercie mes directeurs de thèse, Christine Toumoulin, maître de conférences à l'Université de Rennes 1, Jean-Louis Coatrieux, directeur de recherche INSERM (Institut National de la Santé Et de la Recherche Médicale), et Huazhong Shu, professeur à l'Université du Sud-Est de Nankin. Leur investissement et leur patience m'ont guidé dans la compréhension des applications et m'ont permis de réaliser cette thèse en cotutelle, ce qui fut un vrai défi. De plus, sans leur rigueur et leur vigilance il m'aurait été impossible de publier le moindre article.

Je remercie Jean-Jacques Bellanger, maître de conférences à l'Université de Rennes 1, pour m'avoir accompagné durant ces trois années. Son soutien a été sans faille, sur tous les plans. Il a su me recadrer dans mes recherches lorsque les voies que j'ai choisies étaient fausses (parfois contre ma volonté, ce qui relève de l'exploit). De plus, sa disponibilité, sa patience et son amour de la science ont fait de lui un encadrant idéal.

Je remercie Christian Roux, Professeur à l'Institut Telecom, et Jingyu Yang, Professeur à l'Université du Sud-Est de Nankin, d'avoir accepté de rapporter sur mon manuscript, bien que non rédigé dans leur langue maternelle.

Je suis très reconnaissant à Jacques Demongeot, professeur à l'Université Joseph Fourier, d'avoir accepté de présider mon jury de thèse, et à Deshan Xia, Professeur à l'Université des Sciences et des Technologies de Nankin, d'avoir pris part à la soutenance.

Je remercie Jian Zhou et Guanyu Yang pour leur aide dans mes travaux, notamment pour

les articles qu'ils ont cosignés avec moi.

Je remercie les membres du LIST, de m'avoir aidé à vivre dans le sud de la Chine. Je pense tout particulièrement à Yinning Hu, qui m'a permis de franchir la Grande Muraille de l'administration chinoise.

Je remercie tous les membres du LTSI, doctorants, post-doctorants et titulaires, pour leur amitié : Amar, Simon, Carole, Ahmad, Laurent, Marie-Paule, Muriel, Paul, Soizic, Mathieu, Lionel, Sophie, François... il m'est impossible de les nommer tous.

Je remercie Bernard Delyon, professeur à l'Université de Rennes 1, ainsi que les intervenants du forum du site `http://www.les-mathematiques.net`, qui ont résolu à maintes reprises mes problèmes de mathématiques.

Je ne voudrais pas oublier Yvon Lafranche et Daniel Martin, maîtres de conférences à l'Université de Rennes 1, pour leur précieuse aide à l'utilisation de Fig4TEX, disponible sur `http://perso.univ-rennes1.fr/yvon.lafranche/fig4tex`.

Enfin je remercie mes parents, ainsi que mon frère Erwan et ma sœur Morgane, pour leur soutien permanent.

Contents

Notations

Table 1: Notations for chapter 1

X, Y	infinite-dimensional Hilbert spaces
f	object function defined on X
g	observed function defined on Y
$\mathcal{A}$	linear bounded operator between X and Y
$\mathcal{A}^*$	adjoint operator of $\mathcal{A}$
$\mathcal{A}^\dagger$	generalized inverse of $\mathcal{A}$
$R(\square)$, $N(\square)$, $D(\square)$	range, kernel and domain of an operator $\square$
$G^\perp, \overline{G}$	orthogonal space and closure of a set G
R_γ	regularized operator
Id	identity operator
$(u_k, v_k, \sigma_k)_k$	SVD decomposition of an operator $\mathcal{A}$
(e_γ, v_γ)	mollifier/reconstruction kernel pair
$\widetilde{\mathcal{A}}_\gamma$	approximate inverse of $\mathcal{A}$
$\mathbf{f}$	n-dimensional object vector
$\mathbf{g}$	m-dimensional observed vector
$\mathbf{A}$	$m \times n$ matrix
$\mathbf{I}$	identity matrix
$(\mathbf{u}_k, \mathbf{v}_k, \sigma_k)_k$	SVD decomposition of $\mathbf{A}$
$\mathrm{p}(\mathbf{f})$	*a priori* distribution of $\mathbf{f}$
$\mathrm{p}(\mathbf{g})$	*a priori* distribution of $\mathbf{g}$
$\mathrm{p}(\mathbf{f}|\mathbf{g})$	*a posteriori* distribution of $\mathbf{f}$
$\mathrm{p}(\mathbf{f}, \mathbf{g})$	joint distribution of $\mathbf{f}$ and $\mathbf{g}$

Table 2: Notations for chapter 2

$\mathcal{L}$	set of lines in a 2-D or 3-D space
L_α	line given by parameter α in a 2-D or 3-D space
Ω^n	unit ball in $\mathbb{R}^n$
S^{n-1}	unit sphere in $\mathbb{R}^n$
$\mathcal{X}$	X-ray transform
$\mathcal{R}$	the Radon transform
$\mathcal{R}^*$	backprojection operator
$\mathcal{C}, \mathcal{F}$	cone-beam and fan-beam operator
$\imath$	the complex number such that $i^2 = -1$
Λ	square-root of the negative laplacian
$\mathcal{I}, \mathcal{J}$	voxel and line index sets
(u_i^n, w_i^n)	voxel basis
ϕ_n	object to voxel sampling operator
$\aleph_i$	voxel cube corresponding to the i-th voxel
$\mathbf{P}$	projection matrix

Table 3: Notations for chapter 3

$\mathcal{T}$	acquisition time interval
$\mathfrak{T}$	discretized acquisition time interval
f_t	dynamic object at instant t
g_t	projection corresponding to f_t
$f(\cdot, \vartheta)$	object function at angle ϑ
$\mathbf{f}_t$	volume vector at time t
$\mathbf{g}_t$	projection corresponding to $\mathbf{f}_t$
$\mathcal{R}_d$	dynamic Radon transform
$\mathcal{P}_t$	projection operator at instant t
$\mathbf{P}_\vartheta$	projection matrix at position ϑ
φ_t	support deformation at time t
E_n	set of voxelized functions
$\mathcal{W}_t$	support deformation operator at time t
$\widetilde{W}_t$	support deformation operator composed with ϕ_n
$\mathbf{W}_t$	deformation matrix at time t

Table 4: Notations for chapter 4 (first part)

N	number or cardiac cycles during an acquisition
T	duration of a cardiac cycle
S	number of phases during a cardiac cycle
s	phase index ($s \in \{1, \ldots, S\}$)
$\mathbf{f}_s$	volume vector at phase s
$\mathbf{g}_s$	observation vector at phase s
Θ_s	set of angles corresponding to phase s
$\vartheta_{n,s}$	n-th projection angle corresponding to phase s
$\mathcal{P}_\vartheta^{\mathrm{geom}}$	geometric projection at angle ϑ
$P(\vartheta)$	projection plane at angle ϑ
$\mathscr{C}_n$	extracted 2-D centrelines on $P(\vartheta_{n,1})$
$\mathscr{C}_\vartheta$	extracted 2-D centrelines on $P(\vartheta)$ ($\mathscr{C}_n = \mathscr{C}_{\vartheta_{n,1}}$)
V	miscellaneous 3-D coronary centreline, $V = \{v_1, \ldots, v_L\}$
V_s	3-D coronary centreline at phase s, $V = \{v_1^s, \ldots, v_L^s\}$
$\mathcal{D}_\ell$	line that links the ℓ-th point of $\mathscr{C}_1$ and$S(\vartheta_{1,1})$
$\mathbf{W}_s$	deformation matrix at phase s
$\mathcal{V} = (\mathcal{V}_{\mathrm{br}}, \mathcal{V}_{\mathrm{pos}})$	vessel structure
$\Upsilon(\mathcal{V})$	set of cliques in $\mathcal{V}$
E_s	data fidelity term of a single point
$\mathbf{E}_s$	data fidelity term of the coronary 3-D model
$\mathbf{F}$	regularity cost function of the coronary 3-D model
$\mathbf{D}_s$	total cost function
D_ϑ	distance to the 2-D centreline $\mathscr{C}_\vartheta$
$\mathscr{H}_\vartheta$	projection of any centreline V on $P(\vartheta)$
$\mathscr{H}_\vartheta^1$	projection of V_1 on $P(\vartheta)$
$\mathscr{B}_{\vartheta,j}$	j-th branch of $\mathscr{C}_\vartheta$
$\mathfrak{D}_\ell(v_\ell)$	local displacement of the ℓ-th point in V

Table 5: Notations for chapter 4 (second part)

$\{(x_m, y_m, z_m),\ m \in \mathcal{M}\}$	uniform grid on Ω
$(\alpha_{X,s}^m, \alpha_{Y,s}^m, \alpha_{Z,s}^m)$	motion parameter on $m \in \mathcal{M}$ as phase s
α_s	concatenation of $\left(\alpha_{X,s}^m, \alpha_{Y,s}^m, \alpha_{Z,s}^m\right)$ for all $m \in \mathcal{M}$
α	concatenation of all α_s's
$\mathbf{a}_s$	α_s reshaped as a vector
$\mathbf{W}(\alpha_s)$	deformation matrix in term of α_s (originally $\mathbf{W}_s$)
$\mathbf{PW}(\alpha)$	combination of $\mathbf{P}$ and $\mathbf{W}(\alpha_s)$ for all $s \in \{1, \ldots, S\}$
b_m	cubic B-spline function centered on (x_m, y_m, z_m)
Δ	voxel to vessels distance vector
$\mathrm{p_{vessels}}$	vessel prior
p_β	markov prior

Introduction

It is trivial to talk today on the continuous and impressive advances made in medical imaging. The principles onto which they rely remain however those which have been developed for years. X-ray, MRI, PET, Ultrasound (US), optical modalities are still occupying the main place in clinical settings and compete each other in order to extend their range of applications or to reach new ones. They differ by their spatial and temporal resolution, their potential to provide insights into anatomical or functional information, the acquisition duration, the patient irradiation, the use or not of contrast enhancement product, their cost, etc. It is widely agreed that if MRI is somewhat more flexible, the advantage of X-ray systems rely on the anatomical details that can be obtained. US devices provide a unique time resolution and they are much cheaper than the other techniques. It is also agreed that coupling these systems, a good example being PET-CT now generalized, open new perspectives not only because they complement each other in terms of information but also because they allow taking into account different properties they highlight into reconstruction methods. The developments observed in optics, beyond the classical and intensively used endoscopic devices, open new ways to explore the human body even if the penetration depth remains limited.

Does the emphasis put above on the physics mean that nothing can be expected from other disciplines? Certainly not. The design of new excitation sequences in MRI remains today an active area of research. New probes or radiopharmaceuticals, derived from research in chemistry, are central for molecular imaging, where MRI and PET will have a major role to play. Engineering sciences will always be required as far as we need for solving and integrating complex technologies (mechanics, electronics). These imaging modalities lead to explore the full body in one examination and subsequently more and more data (hundreds of megabytes) are generated, with new challenging issues for storage, processing and interpretation, in other words more computing resources.

These multiple facets of medical imaging include also the reconstruction problems, e.g. how to recover from projection data, the object properties. This topic, called *tomography*, is a major step to accomplish before any processing and clinical use and many works are going on in this area. They deal with static and time-evolving objects. Part of our work is devoted to the former case by revisiting and reformulating some theoretical features. In the latter case, the tracking and the characterization of perfusion in PET for instance is an important issue. Compensating the respiratory motion to avoid the blurring of anatomical details is another problem. But, it is perhaps the reconstruction of fast moving organs, such as the heart, which is the more difficult. X-ray devices have already shown that they can bring significant three-dimensional (3-D) information in that case. Multidetector CT (MDCT) devices provide a lot of details on the different cardiac structures (cavities, myocardium, arteries and veins). Sophisticated reconstruction algorithms are here required with ECG synchronization. Rotational-X (Rot-X) systems, with a full two-dimensional (2-D) detector rotating around the body, offer the possibility to access to the coronary structures. *Dynamic tomography* will then be a second part of our work with a focus on Rot-X and coronary reconstruction.

Chapter 1 deals with *inverse problems* in general. Two cases are identified: infinite- and finite-dimensional inverse problems. In both cases, one wish to reconstruct an object defined by a function (for the infinite-dimensional case) or a vector (for the finite-dimensional case). For the infinite-dimensional inverse problem, we investigate two major aspects: the regularization of the *singular value decomposition* of the observation operator and the *approximate inverse*, which leads to the *filtered backprojection* algorithm in tomography. As for the finite-dimensional inverse problem, the regularization of the singular value decomposition must be analyzed. We also investigated the bayesian formulation, which leads to a maximization *a posteriori* method.

Chapter 2 is an application of the theoretical aspects reported in chapter 1 to computed tomography. This chapter also makes a distinction between the infinite- and finite-dimensional cases. The infinite-dimensional situation is mainly based on the *Radon transform*, the *fan-beam* and the *cone-beam transform*. Two filtered backprojection methods are mentioned. For the finite-dimensional case, we define the voxel discretization process and the projection matrix that is involved in the inverse problem.

In chapter 3 we generalize the notion of tomography in order to include a dynamic compo-

nent, thus, the so-called dynamic tomography. For the infinite-dimensional case, we define the *dynamic Radon transform* and study its properties. We focus on its non-invertibility which is a major issue for image reconstruction. We propose two approaches for finite-dimensional reconstruction: one is based on the reconstruction of the object at each instant assuming that the variations between two consecutive instants are small, and the other one is a motion-compensated tomographic reconstruction based on a object support deformation function *a priori* known.

As the goal of these three first chapters was to propose a global vision of the theoretical tools (and not to implement them), chapter 4 aims at proposing an original algebraic method for the coronary 3-D tomographic reconstruction from a full rotational X-ray sequence. The motion due to the heart beating is estimated thanks to a 3-D coronary non-parametric deformable model which yields the reconstruction of 3-D centrelines at each cardiac phase. A vessel prior is also used to avoid that the reconstruction process converges to local minimum. We called our method *Reconstruction with Motion Compensation using a Vessel Prior*. We tested our method on simulated data, generated from a sequence of 3-D coronary centrelines previously extracted from 20 volumes reconstructed at every 5% of the RR interval from a 64-slices GE LightSpeed CT coronary angiography.

Concluding remarks are then made and some perspectives are given. They include a discussion of the key steps and technology evolution which are central for the future.

Chapter 1

Linear Inverse Problems

1.1 Introduction

Inverse problems appear whenever one seek for an unobserved data $f \in X$ from a measurement $g \in Y$, where X and Y are Banach spaces. In most cases, the measurement g is the result of a transformation of f by an known application $F : X \to Y$. Therefore, an inverse problem can be written as the following equation:

$$F(f) = g. \tag{1.1}$$

The task consists to recover f from g. Two questions then arise: the existence of the inverse transformation $F^{-1} : Y \to X$, and its smoothness. If F is invertible and its inverse is continuous, no special attention is required and we say that inverse problem (1.1) is *well-posed*. If F is not invertible, f cannot be directly recovered. If F is invertible, its inverse F^{-1} may not be continuous. For instance, if X and Y are two Hilbert spaces and F is a compact operator (see [Brezis 1999] for a definition), F^{-1} is unbounded. In practical cases, the data are affected by noise, *i.e.* we observe $g_\varepsilon = F(f) + \varepsilon$ instead of $g = F(f)$. In that situation, one cannot guarantee that the error $\|F^{-1}(g_\varepsilon) - f\|_X$ is small. Starting from these two observations, Hadamard [Hadamard 1902] defined inverse problem (1.1) as an *ill-posed* problem.

Definition 1. *Inverse problem* (1.1) *is said to be* ill-posed according to Hadamard *if one of these statements holds true:*

- *F is not invertible.*

- *F is invertible and F^{-1} is not continuous.*

Facing an ill-posed problem in the sense of definition 1, one can only find a suitable $f^\dagger$ such that $F(f^\dagger) \simeq g$, which leads to a mapping $F^\dagger : D(F^\dagger) \subset Y \to X$, and "approximate" this mapping by a smooth application $F_\gamma^\dagger$. This step is the regularization of the ill-posed problem.

1.2   Linear inverse problems in infinite dimension Hilbert spaces

A common situation is the linear inverse problem, that is to say instead of facing inverse problem (1.1), we deal with the equation

$$\mathcal{A}f = g, \tag{1.2}$$

where $\mathcal{A} : X \to Y$ is a bounded linear operator between two Hilbert spaces. Many examples can be found for integral operators between two functional spaces.

Example 1. The deconvolution problem consists in solving the following equation with respect to $f \in L^2(\Omega)$:

$$\int_\Omega f(x)k(x,y)\mathrm{d}x = g(y),$$

with $g \in L^2(\Omega)$, $k \in L^2(\Omega \times \Omega)$.

Since $\mathcal{A}$ is not invertible, we do not solve the equation (1.2) but we minimize

$$\|\mathcal{A}f - g\|_Y^2. \tag{1.3}$$

The minimization of (1.3) is possible provided that g is in $R(\mathcal{A}) \oplus R(\mathcal{A})^{\perp 1}$ [Louis 1989]. Choosing the minimal-norm minimizer $f^\dagger$ of (1.3) leads to a new mapping called *generalized inverse.*

Definition 2. *The mapping $\mathcal{A}^\dagger : R(\mathcal{A}) \oplus R(\mathcal{A})^\perp \subset Y \to X$ which maps $g \in R(\mathcal{A}) \oplus R(\mathcal{A})^\perp$ to the minimal-norm minimizer of* (1.3) *is called* generalized inverse *or* Moore-Penrose inverse *of $\mathcal{A}$.*

$\mathcal{A}^\dagger$ is well-defined on $R(\mathcal{A}) \oplus R(\mathcal{A})^\perp$ and we have the following fundamental properties [Schuster 2007]:

---

[1] Note that $R(\mathcal{A}) \oplus R(\mathcal{A})^\perp = Y$ if and only if $R(\mathcal{A})$ is closed in Y.

Proposition 1. *Let $\mathcal{A} : X \to Y$ be a linear bounded operator and $\mathcal{A}^\dagger : D(\mathcal{A}^\dagger) = R(\mathcal{A}) \oplus R(\mathcal{A})^\perp \to X$ be its generalized inverse. Let $g \in D(\mathcal{A}^\dagger)$ and $f^\dagger = \mathcal{A}^\dagger g$. Let $\widetilde{\mathcal{A}} : N(\mathcal{A})^\perp \to R(\mathcal{A})$ be the restriction of $\mathcal{A}$ to $N(\mathcal{A})^\perp$. Then,*

1. *$\mathcal{A}^\dagger$ is linear.*

2. *Any minimizer of (1.3) is solution of*

$$\mathcal{A}^*\mathcal{A}f = \mathcal{A}^*g, \tag{1.4}$$

   where $\mathcal{A}^* : Y \to X$ is the adjoint operator of $\mathcal{A}$. $f^\dagger$ is the unique solution of (1.4) in $N(\mathcal{A})^\perp$.

3. *Any minimizer of (1.3) is solution of*

$$\mathcal{A}f = P_{R(\mathcal{A})}g, \tag{1.5}$$

   where P_E denotes the orthogonal projector on E.

4. *$f^\dagger$ is the unique solution of (1.5) in $N(\mathcal{A})^\perp$.*

5. *$\mathcal{A}^\dagger$ is the unique linear extension of $\widetilde{\mathcal{A}}^{-1}$ to $R(\mathcal{A}) \oplus R(\mathcal{A})^\perp$.*

6. *$N(\mathcal{A}^\dagger) = R(\mathcal{A})^\perp$, $R(\mathcal{A}^\dagger) = N(\mathcal{A})^\perp$*

7. *$\mathcal{A}^\dagger$ is bounded if and only if $R(\mathcal{A})$ is closed in Y.*

Proof. We prove here the last statement only. Let $\widetilde{\mathcal{A}} : N(\mathcal{A})^\perp \to R(\mathcal{A})$ the restriction of $\mathcal{A}$ to $N(\mathcal{A})^\perp$. If $\mathcal{A}^\dagger$ is continuous, $\widetilde{\mathcal{A}}^{-1}$ is continuous and $R(\mathcal{A})$ is a Hilbert space. Therefore $R(\mathbf{A})$ is closed in Y. Conversely, if $R(\mathcal{A})$ is closed, then according to Banach theorem [Rudin 1997], $\widetilde{\mathcal{A}}^{-1}$ is continuous, and so $\mathcal{A}^\dagger$ is. $\square$

The last assertion raises a new condition to ensure the continuous dependence of the solution to the data, which leads to a new definition of an ill-posed problem [Nashed 1987].

Definition 3. *Inverse problem (1.2) is called* ill-posed *according to Nashed if $R(\mathcal{A})$ is not closed in Y.*

1.2.1   Compact operators

A important case to consider in a linear inverse problem is compact operator. Such operators are frequently encountered in inverse problem, especially if the observed data g results of an integration operation of f.

Example 2. Let us consider the Banach space $E = \mathcal{C}([0,1])$, with $\forall f \in E, \|f\|_\infty = \sup_{[0,1]} |f(t)|$. Then the integral operator $V : E \to E$ defined by

$$\forall x \in [0,1], \quad V f(x) = \int_0^x f(t)\mathrm{d}t$$

is compact.

In computerized tomography, the operator encountered is the *Radon transform*, which is also compact, as we will see later in chapter 2. A first result is the following :

Proposition 2. *Let $\mathcal{A} : X \to Y$ be a compact operator between two Hilbert spaces such that* $\dim(R(\mathcal{A})) = +\infty$. *Then inverse problem (1.2) is ill-posed according to Nashed.*

Proof. This result is a direct consequence of Banach and Rietz theorems (see [Rudin 1997]).
□

Therefore, the compactness of a bounded operator is source of ill-posedness for equation 1.2. However, a compact operator can be expressed thanks to the *spectral representation theorem*, which shall be very useful to overcome this problem.

Theorem 1. *Let $\mathcal{A} : X \to Y$ be a compact operator between two separable Hilbert spaces such that* $\dim(R(\mathcal{A})) = +\infty$. *There exists a Hilbert base $(u_k)_k$ of $N(\mathcal{A})^\perp$, a Hilbert base $(v_k)_k$ of* $\overline{R(\mathcal{A})}$, *and a sequence $(\sigma_k)_k$ such that $\lim_{k\to+\infty} \sigma_k = 0$ and $\sigma_k > 0$ for all $k \in \mathbb{N}$, and*

$$\forall k \in \mathbb{N}, \quad \mathcal{A}u_k = \sigma_k v_k, \quad \mathcal{A}^* v_k = \sigma_k u_k. \tag{1.6}$$

We call $(\sigma_k, u_k, v_k)_k$ *singular system* of $\mathcal{A}$, and $(\sigma_k)_k$ are the *eigenvalues* of $\mathcal{A}$. We also assume that $\sigma_k \geq \sigma_{k+1}$ for all k. As we saw in this section, the generalized inverse of a bounded operator exists and is well-defined. So far it can be only computed by minimizing (1.3) or by solving (1.4) or (1.5) in $N(\mathcal{A})^\perp$. The singular system of a compact operator allows to express the generalized inverse $\mathcal{A}^\dagger$ of $\mathcal{A}$ in term of v_k and σ_k. Let $g = g_1 + g_2$, with

$(g_1, g_2) \in R(\mathcal{A}) \times R(\mathcal{A})^\perp$, and $f \in N(\mathcal{A})^\perp$ such that $\mathcal{A}f = g_1$. We have $\mathcal{A}^\dagger g = f$ and we can write

$$f = \sum_{k=0}^{+\infty} \langle f, u_k \rangle u_k = \sum_{k=0}^{+\infty} \frac{1}{\sigma_k} \langle g, v_k \rangle u_k = \mathcal{A}^\dagger g. \tag{1.7}$$

This writing of f in terms of $\mathcal{A}f$ is called *Singular Value Decomposition* (SVD) of $\mathcal{A}$. Note that the two sums in (1.7) converge in X since $\sum_{k=0}^{+\infty} \langle f, u_k \rangle^2 = \|f\|_X^2$. However, one can ensure that the sum $\sum_{k=0}^{+\infty} \sigma_k^{-1} \langle g, v_k \rangle u_k$ converges if $g \in R(\mathcal{A}) \oplus R(\mathcal{A})^\perp$. This clearly reflects the unboundedness of $\mathcal{A}^\dagger$ (for instance if g is replaced by noisy data $g_\varepsilon = g + \varepsilon$). The convergence criterion for the sum, which is

$$\sum_{k=0}^{+\infty} \sigma_k^{-2} \langle g, v_k \rangle^2 < +\infty$$

is called the *Picard criterion*, and can be seen as a smoothness condition for the observations g.

1.2.2 The semi-discrete inverse problem

In some situations, inverse problem (1.2) may be inaccurate, especially if we only have a finite number of measurements at our disposal. For instance, if X and Y are functional space, we may only observe g in a finite number of points *i.e.* we observe

$$g_n = (g(x_1), \dots, g(x_n)) \in \mathbb{C}^n.$$

Thus, inverse problem (1.2) has to be replaced by

$$\mathcal{A}_n f = g_n, \tag{1.8}$$

where $\mathcal{A}_n$ is a sampled version of $\mathcal{A}$. $\mathcal{A}_n$ can be interpreted as the product $\Psi_n \mathcal{A}$, where Ψ_n is a sampling operator that acts on elements of Y. Clearly, inverse problem (1.8) is ill-posed due to the non-injectivity of $\mathcal{A}_n$. This model must change our approach for two main reasons. Let us assume for now that X and Y are two L^2 spaces:

- The sampling operator Ψ_n is not defined everywhere on Y: for example, let $(g_1, g_2) \in Y^2$ such that for all $x \in \mathbb{C} \setminus \{x_1, \dots, x_n\}$, $g_1(x) = g_2(x)$ and $g_1(x_i) \neq g_2(x_i)$ for at least one $i \in \{1, \dots, n\}$, then g_1 and g_2 are equal in Y but $\Psi_n g_1 \neq \Psi_n g_2$. $\mathcal{A}_n$ should be defined on a subspace X_1 of X such that its image is contained in a set of regular function $Y_1 \subset Y$. For instance, X_1 and Y_1 can be suitable Sobolev spaces (see [Wloka 1987] for detailed definitions).

- The operator $\mathcal{A}_n : X_1 \subset X \to \mathbb{C}^n$ may not be bounded and its adjoint operator $\mathcal{A}_n^*$ may not be defined.

1.2.3 Regularization of a linear ill-posed problems

In this section, we focus on the construction of *regularization method* in order to approximate $\mathcal{A}^\dagger$ by a sequence of bounded operator, according to the following definition.

Definition 4. *Let $\mathcal{A} : X \to Y$ be a bounded operator between two Hilbert spaces. A family of bounded operators $R_\gamma : Y \to X$ is said to be a* regularization method *or* regularization operator *if for all $g \in D(\mathcal{A}^\dagger)$ there exists a parameter choice $\gamma(\delta, g^\delta)$ fulfilling*

$$\limsup_{\delta \to 0} \{\gamma(\delta, g^\delta) : g^\delta \in Y, \|g^\delta - g\|_Y < \delta\} = 0,$$

such that

$$\limsup_{\delta \to 0} \{\|R_{\gamma(\delta,g^\delta)} g^\delta - \mathcal{A}^\dagger g\|_X : g^\delta \in Y, \|g^\delta - g\|_Y < \delta\} = 0.$$

In other word, R_γ is a regularization method for $\mathcal{A}^\dagger$ provided that

$$\forall g \in D(\mathcal{A}^\dagger), \quad \lim_{\gamma \to 0} \|R_\gamma g - \mathcal{A}^\dagger g\|_X = 0.$$

1.2.3.1 Classical methods of regularization

As it has been pointed out in section 1.2.1, the unboundedness of the generalized inverse of a compact operator is due to small eigenvalues. A natural way to compensate this problem is to replace σ_k^{-1} in (1.7) by $F_\gamma(\sigma_k)\sigma_k^{-1}$, with a suitable filter function $F_\gamma(\sigma_k)$ such that the induced operator R_γ is an approximation method for $\mathcal{A}^\dagger$.

Definition 5. *Let $\mathcal{A} : X \to Y$ be a compact operator between two Hilbert spaces with eigenvalues $(\sigma_k)_k$. The filter function is called* regularizing *if*

$$\sup_k |F_\gamma(\sigma_k)\sigma_k^{-1}| = c(\gamma) \in \mathbb{R}^+, \tag{1.9}$$

$$\forall k \in \mathbb{N}, \quad \lim_{\gamma \to 0} F_\gamma(\sigma_k) = 1 \tag{1.10}$$

and

$$\sup_{k,\gamma} |F_\gamma(\sigma_k)| < +\infty. \tag{1.11}$$

Let $R_\gamma : Y \to X$ be the family of operators induced by F_γ. Equation (1.9) ensures that R_γ is a bounded operator, (1.10) and (1.11) ensure the pointwise convergence to $\mathcal{A}^\dagger$. We can prove [Schuster 2007] that the family of operators $R_\gamma : Y \to X$ induced by F_γ is a regularization method for $\mathcal{A}^\dagger$, with $\|R_\gamma\|_{Y,X} = c(\gamma)$ [Louis 1989].

Example 3. The function F_γ defined by

$$F_\gamma(\sigma) = \begin{cases} 1 \; : \; \sigma \geq \gamma \\ 0 \; : \; \sigma < \gamma \end{cases}$$

is a regularizing filter, called *truncated singular value decomposition.*

Example 4. The function F_γ defined by

$$F_\gamma(\sigma) = \frac{\sigma^2}{\sigma^2 + \gamma}$$

is a regularizing filter. The corresponding regularization R_γ is called *Tikhonov-Phillips regularization.* One can see that R_γ can be expressed as

$$\forall g \in Y, \quad R_\gamma g = (\mathcal{A}^* \mathcal{A} + \gamma Id)^{-1} \mathcal{A}^* g$$

provided that $-\gamma$ is not a spectral value for the self-adjoint compact operator $\mathcal{A}^* \mathcal{A}$. The regularization operator R_γ can also be seen as the unique minimizer of

$$\|\mathcal{A}f - g\|_Y^2 + \gamma^2 \|f\|_X^2. \tag{1.12}$$

As observed in example 4, the regularization of the generalized inverse can be performed by minimizing a functional similar to (1.12) instead of minimizing (1.3). To summarize, we focus on the minimization of

$$\|\mathcal{A}f - g\|_Y^2 + \gamma P(f), \tag{1.13}$$

where $P(f)$ is a smoothness term for f. For example $P(f)$ can be a functional that penalize high variations in f. If f is a discrete image, $P(f)$ can be the minus log-likelihood of a Markov field distribution.

1.2.3.2   Approximate inverse

In this section, we focus on the construction of regularizing methods based on the *approximate inverse* [Louis 1990, Schuster 2007, Rieder 2003a]. We assume that X and Y are L^2 functional

spaces: $X = L^2(\Omega_1, \lambda_1)$ and $Y = L^2(\Omega_2, \lambda_2)$, where Ω_i are open subset of $\mathbb{R}^{n_i}$. Let $\mathcal{A} : X \to Y$ be a bounded operator. We still focus at solving the linear inverse problem (1.2):

$$\mathcal{A}f = g.$$

Instead of approximating f, the approximate inverse aims at computing its moments

$$f_\gamma(y) = \langle f, e_\gamma(\cdot, y) \rangle_X, \tag{1.14}$$

where $e_\gamma \in L^2(\mathbb{R}^{n_1} \times \mathbb{R}^{n_1})$ is a suitable *mollifier, i.e.* a function such that $f_\gamma(y)$ is a good approximation of $f(y)$.

Definition 6. *Let $e_\gamma \in L^2(\mathbb{R}^{n_1} \times \mathbb{R}^{n_1})$ be a function such that*

$$\forall y \in \Omega_1, \quad \int_{\mathbb{R}^{n_1}} e_\gamma(x, y) \mathrm{d}\lambda_1(x) = 1.$$

If the function f_γ defined by (1.14) converges to f in X as γ tends to 0, then we call e_γ a mollifier.

The function $e_\gamma(\cdot, y)$ can be seen as an approximation of the Dirac distribution δ_y. For instance, if $e \in X$ is a smooth function with $\int_{\Omega_1} e(x)\mathrm{d}\lambda(x) = 1$, e_γ can be obtained by computing

$$e_\gamma(x, y) = \gamma^{-n_1} e((x - y)/\gamma).$$

If $e_\gamma(\cdot, y)$ is in the range of $\mathcal{A}^*$, the moments (1.14) can be easily computed by solving the linear equation

$$\forall y \in \Omega_1, \quad \mathcal{A}^* v_\gamma(y) = e_\gamma(\cdot, y) \tag{1.15}$$

with respect to $v_\gamma(y) \in Y$. Indeed, once a suitable function $v_\gamma(y)$ is at our disposal, we have

$$f_\gamma(y) = \langle f, e_\gamma(\cdot, y) \rangle_X = \langle g, v_\gamma(y) \rangle_Y.$$

In a general case, $e_\gamma(\cdot, y)$ is not in the range of $\mathcal{A}^*$ (for example if $N(\mathcal{A})$ is non trivial). Nevertheless, if $e_\gamma(\cdot, y) \in R(\mathcal{A}^*) \oplus R(\mathcal{A}^*)^\perp$, the square error

$$\|\mathcal{A}^* v_\gamma - e_\gamma(\cdot, y)\|_X.$$

can be minimized according to v [Schuster 2007]. This allows a reconstruction of f in $N(\mathbf{A})^\perp$. However, as we will see in section 2.3.1.1 for the Radon transform, we are only interested in the case where the equation (1.15) is solvable.

Definition 7. *For all $y \in \Omega_1$, let $v_\gamma(y)$ be the minimum norm solution of* (1.15). *The mapping $y \mapsto v_\gamma(y)$ is called* reconstruction kernel of $\mathcal{A}$ induced by e_γ.

Note that if $v_\gamma(y)$ is a minimum norm solution of (1.15), then $v_\gamma(y) \in N(\mathcal{A}^*)^\perp$. We can now define the approximate inverse of $\mathcal{A}$.

Definition 8. *Let v_γ be a reconstruction kernel of $\mathcal{A}$ induced by a mollifier e_γ. The linear operator*

$$\widetilde{\mathcal{A}}_\gamma : Y \longrightarrow X \qquad (1.16)$$
$$g \longmapsto \widetilde{\mathcal{A}}_\gamma g$$

such that for all $y \in \Omega_1$,

$$\widetilde{\mathcal{A}}_\gamma g(y) = \langle g, v_\gamma(y) \rangle_Y$$

is called the approximate inverse of $\mathcal{A}$.

$\widetilde{\mathcal{A}}_\gamma$ is well-defined and bounded provided that

$$\int_{\Omega_1} \|v_\gamma(y)\|_Y^2 \, \mathrm{d}\lambda_1(y) < +\infty$$

(see [Schuster 2007]). We have the following convergence property:

Theorem 2. *Let $g \in R(\mathcal{A}) \oplus R(\mathcal{A})^\perp$. Then we have*

$$\lim_{\gamma \to 0} \widetilde{\mathcal{A}}_\gamma g = \mathcal{A}^\dagger g.$$

Proof. Let $(g_1, g_2) \in R(\mathcal{A}) \times R(\mathcal{A})^\perp$ such that $g = g_1 + g_2$, and let $f \in N(\mathcal{A})^\perp$ such that $\mathcal{A}f = g_1$. Then we have that for all $y \in \Omega_1$

$$\widetilde{\mathcal{A}}_\gamma g = \langle g_1 + g_2, v_\gamma(y) \rangle_Y = \langle \mathcal{A}f, v_\gamma(y) \rangle_Y = \langle f, e_\gamma(\cdot, y) \rangle_X = \langle \mathcal{A}^\dagger g, e_\gamma(\cdot, y) \rangle_X,$$

using the fact that $v_\gamma(y) \in N(\mathcal{A}^*)^\perp = \overline{R(\mathcal{A})}$ and the continuity of the mapping $v \mapsto \langle g_2, v \rangle$. With definition 6, we proved the expected convergence. $\square$

The approximate inverse is used in tomography, and is known as the *filtered backprojection,* which shall be detailed in section 2.3.1.1.

1.2.3.3   Semi-discrete approximate inverse

We summarize here the approach proposed in [Schuster 2007, Rieder 2000b, Rieder 2003b] to build an approximate inverse to solve semi-discrete inverse problem. Recall the semi-discrete inverse problem (1.8)

$$\mathcal{A}_n f = \Psi_n \mathcal{A} f = g_n,$$

where $g_n \in \mathbb{C}^n$ and Ψ_n is a sampling operator. As we mention in section 1.2.2, $\mathcal{A}_n$ is not well defined on X and suitable topological subspaces of X and Y have to be considered. Moreover, $\mathcal{A}_n$ is unbounded, which makes the construction of a mollifier/reconstruction kernel pair impossible.

Let X_1 and Y_1 be two subspaces of smooth functions [2] of X and Y respectively, such that $\mathcal{A} : X_1 \to Y_1$ is bounded. In this section, we assume that the bounded operator $\mathcal{A} : X \to Y$ is injective. The non-injective case is treated in [Rieder 2004]. Moreover, we assume the following assertions hold:

- Both injections $X_1 \hookrightarrow X$ and $Y_1 \hookrightarrow Y$ are continuous, that is to say, there exists a positive constant C_X (resp. C_Y) such that for all $f \in X_1$ (resp. $g \in Y_1$), $\|f\|_X \le C_X \|f\|_{X_1}$ (resp. $\|g\|_Y \le C_Y \|g\|_{Y_1}$).

- The sampling operator $\Psi_n : Y_1 \to \mathbb{C}^n$ is bounded[3].

- The sampled observation operator $\mathcal{A}_n = \Psi_n \mathcal{A} : X_1 \to \mathbb{C}^n$ is bounded[4].

Since the observed data are discrete, an interpolation will further be required. Let $(\varphi_{n,k})_{k=1}^n$ be a family of functions in Y such that

$$\frac{1}{n} \sum_{k=1}^n |a_k|^2 \preceq \Big\| \sum_{k=1}^n a_k \varphi_{n,k} \Big\|_Y^2 \preceq \frac{1}{n} \sum_{k=1}^n |a_k|^2. \tag{1.17}$$

where the inequality $a \preceq b$ means that there exists a constant C independent of any index and parameters such that $a \le Cb$. Such a family $(\varphi_{n,k})_{k=1}^n$ is called a *Riesz system*. The interpolation operator is defined as follows:

$$
\begin{aligned}
Q_n : \mathbb{C}^n &\longrightarrow Y \\
a &\longmapsto Q_n a = \sum_{k=1}^n a_k \varphi_{n,k}.
\end{aligned}
$$

---

[2] X_1 and Y_1 are two topological spaces with their own topology, which are different from X and Y.

[3] This holds true if Y_1 is a suitable Sobolev space.

[4] The boundeness is valid for X_1's topology, as in most cases $\mathcal{A}_n = \Psi_n \mathcal{A} : X_1 \subset X \to \mathbb{C}^n$ is unbounded.

Let us define the data interpolation operator:

$$\Pi_n : Y_1 \longrightarrow Y$$
$$g \longmapsto Q_n \Psi_n g.$$

We assume that

$$\|\Pi_n\|_{Y_1, Y} \preceq 1 \tag{1.18}$$

and that Π_n fulfills the approximation property:

$$\forall g \in Y_1, \quad \|g - \Pi_n g\|_Y \preceq \rho_n \|g\|_{Y_1}. \tag{1.19}$$

where ρ_n is a sequence in $\mathbb{R}_+^*$ such that $\rho_n \downarrow 0$. Let $G_n \in \mathbb{C}^{n \times n}$, $(G_n)_{i,j} = \langle \varphi_{n,i}, \varphi_{n,j} \rangle_Y$ the Gram matrix induced by $(\varphi_{n,k})_{k=1}^n$. We have

$$G_n \Psi_n = Q_n^* \Pi_n. \tag{1.20}$$

and, according to (1.17)

$$\|G_n\| \preceq \frac{1}{n}. \tag{1.21}$$

As we have to deal with discrete data, we consider a set of mollifiers $(e_i^d)_{i=1}^d$ instead of a family $e_\gamma(\cdot, y)$ indexed by y. Here e_i^d can be interpreted as an approximation of the dirac function δ_{x_i} as the number of mollifiers d grows. The mollifier's property is defined as follow.

Definition 9. *Let $(b_i^d)_{i=1}^d$ be a set of functions in X which fulfills the Riesz property* (1.17). *The functions e_i^d are said to be* mollifiers *with respect to $(b_i^d)_{i=1}^d$ if the operator*

$$E_d : X \longrightarrow X \tag{1.22}$$
$$f \longmapsto \sum_{i=1}^d \langle f, e_i^d \rangle_X b_i^d$$

fulfills

$$\forall f \in X, \quad \lim_{d \to +\infty} \|E_d f - f\|_X = 0. \tag{1.23}$$

The mollifier/reconstruction kernel pairs are defined as follows: for all $i = 1, \ldots, d$, we look for solutions v_i^d of

$$\mathcal{A}^* v_i^d = e_i^d \tag{1.24}$$

in Y_1.

If e_i^d is not in the range of $\mathcal{A}^*$, we have to assume that Y_1 is dense in Y [Rieder 2000b, Rieder 2003b]. Now for a given family of pairs $(e_i^d, v_i^d)_{i=1}^d$ fulfilling (1.24), we define

$$\begin{aligned} \Sigma_{n,d} : \mathbb{C}^n &\longrightarrow \mathbb{C}^d \\ w &\longmapsto \left(\langle\, w, G_n \Psi_n v_i^d \rangle_{\mathbb{C}^n} \right)_{i=1,\ldots,d} \end{aligned}$$

and

$$\begin{aligned} E : X &\longrightarrow \mathbb{C}^d \\ f &\longmapsto \left(\langle f, e_i^d \rangle_X \right)_{i=1,\ldots,d}. \end{aligned}$$

Here Ef can be interpreted as the moments $\langle f, e_\gamma(\cdot, y) \rangle$ seen in section 1.2.3.2, that we wish to estimate. We are now ready to build the discrete approximate inverse of $\mathcal{A}_n$.

Definition 10. *The* approximate inverse *of $\mathcal{A}_n$ is the operator $\widetilde{\mathcal{A}}_{n,d} : \mathbb{C}^n \to X$ defined by*

$$\forall w \in \mathbb{C}^n, \quad \widetilde{\mathcal{A}}_{n,d} w = \sum_{i=1}^d (\Sigma_{n,d} w)_i b_i^d.$$

First of all, we need to prove the convergence of $\Sigma_{n,d} \mathcal{A}_n f$ to Ef.

Theorem 3. *Let $f \in X_1$. We have*

$$\| \Sigma_{n,d} \mathcal{A}_n f - Ef \|_\infty \preceq \rho_n \max_{i=1,\ldots,d} \| v_i^d \|_{Y_1} \| f \|_{X_1}.$$

Proof. Let $i \in \{1, \ldots, d\}$, $f \in X_1$ and $g = \mathcal{A}f \in Y_1$. We have

$$\begin{aligned} |(\Sigma_{n,d} \mathcal{A}_n f)_i - (Ef)_i| &= |\langle \mathcal{A}_n f, G_n \Psi_n v_i^d \rangle_{\mathbb{C}^n} - \langle f, e_i^d - \mathcal{A}^* v_i^d + \mathcal{A}^* v_i^d \rangle_X| \\ &\leq |\langle \Pi_n \mathcal{A} f, \Pi_n v_i^d \rangle_Y - \langle \mathcal{A}f, v_i^d \rangle_Y| \quad \text{using (1.20) and (1.24)} \\ &\leq \| \Pi_n g - g \|_Y \| \Pi_n v_i^d \|_Y + \| \Pi_n v_i^d - v_i^d \|_Y \| g \|_Y \\ &\preceq \rho_n \| g \|_{Y_1} \| v_i^d \|_{Y_1} + \rho_n \| v_i^d \|_{Y_1} \| g \|_Y \quad \text{using (1.19)} \\ &\preceq \rho_n \| v_i^d \|_{Y_1} \| f \|_{X_1}, \end{aligned}$$

thanks to the boundedness of $\mathcal{A} : X_1 \to Y_1$ and $Y_1 \hookrightarrow Y$. $\qquad\qquad\square$

Finally, we have the following convergence theorem:

Theorem 4. *Let $f \in X_1$, $(e_i^d, v_i^d, b_i^d)_{i=1}^d$ such that $(e_i^d)_{i=1}^d$ is a family of mollifiers with respect to $(b_i^d)_{i=1}^d$ and the pair (e_i^d, v_i^d) fulfills (1.24) for all $i = 1, \ldots, d$. Then*

$$\|\widetilde{\mathcal{A}}_{n,d}\mathcal{A}_n f - f\|_X \preceq \|f - E_d f\|_X + \rho_n \left(\frac{1}{d}\sum_{i=1}^d \|v_i^d\|_{Y_1}^2\right)^{1/2} \|f\|_{X_1}. \tag{1.25}$$

If $d^{-1}\sum_{i=1}^d \|v_i^d\|_{Y_1}^2$ is bounded, then

$$\lim_{n,d\to+\infty} \|\widetilde{\mathcal{A}}_{n,d}\mathcal{A}_n f - f\|_X = 0.$$

If $\mathcal{A}$ is non-injective, a similar result can be obtain by replacing $\|\widetilde{\mathcal{A}}_{n,d}\mathcal{A}_n f - f\|_X$ by $\|\widetilde{\mathcal{A}}_{n,d}\mathcal{A}_n f - P_{N(\mathcal{A})^\perp} f\|_X$ in (1.25) [Rieder 2004].

1.3 Inverse problems in finite dimension

1.3.1 Introduction

In several applications, the object f we wish to reconstruct by solving inverse problem (1.2) is modeled by a vector $\mathbf{f}$. For example, in computerized tomography, the observation is a set of projections of an attenuation/emission function $\mathcal{P}f$ (see section 2.1.1), but it can be only reconstructed as an image or a volume, which is a vector of grey level values located on each pixel or voxel. As the observations are also discrete in practical case, the linear problem (1.2) becomes

$$\mathbf{Af} = \mathbf{g}, \tag{1.26}$$

where $\mathbf{g}$ is the measurement vector, and $\mathbf{A} : \mathbb{R}^n \to \mathbb{R}^m$ is the linear observation operator which, in this case, is a matrix.

In most practical cases $\mathbf{A}$ is a (m, n) rectangular matrix and is not invertible: inverse problem (1.26) is therefore ill-posed. Let the square defect

$$\|\mathbf{Af} - \mathbf{g}\|^2. \tag{1.27}$$

As it has been mentioned in section 1.2, one can only consider the generalized inverse of $\mathbf{A}$ *i.e.* the mapping $\mathbf{A}^\dagger$ which maps $\mathbf{g}$ to the minimal-norm minimizer of (1.27). The generalized inverse $\mathbf{A}^\dagger$ is defined everywhere on $\mathbb{R}^m$ since $\mathbf{A}$ is a finite-rank operator. Let $\mathbf{f}$ be a minimizer of (1.27). With proposition 1, we have that $\mathbf{f}$ is solution of the equation

$$\mathbf{A}^T\mathbf{Af} = \mathbf{A}^T\mathbf{g}, \tag{1.28}$$

where $\mathbf{A}^T$ denotes the transpose of $\mathbf{A}$. If $\mathbf{A}^T\mathbf{A}$ is invertible (which implies that $m \geq n$), the generalized inverse can be easily computed:

$$\mathbf{A}^\dagger\mathbf{g} = (\mathbf{A}^T\mathbf{A})^{-1}\mathbf{A}^T\mathbf{g}.$$

If $n > m$ or if $m \geq n$ and $\text{rank}(\mathbf{A}) < n$, $\mathbf{A}^T\mathbf{A}$ is not invertible and $\mathbf{A}^\dagger$ cannot be directly computed. Computing $\mathbf{A}^\dagger\mathbf{g}$ is then equivalent to finding the minimum-norm solution of (1.26). This can be done in two ways:

- If $n > m$ and $\text{rank}(\mathbf{A}) = m$, the set of vector $\mathbf{f}$ such that (1.26) holds true is infinite and one can compute $\mathbf{A}^\dagger$ by considering the following minimization problem

$$\text{minimize} \quad \|\mathbf{f}\| \quad \text{such that} \quad \mathbf{A}\mathbf{f} = \mathbf{g}. \tag{1.29}$$

- $\mathbf{A}^T\mathbf{A}$ can be approximated by a sequence of invertible matrix. This way to proceed is equivalent as including a regularity term in (1.26) or as considering a regularized version of the SVD decomposition, as we shall see in section 1.3.2.

1.3.2   SVD decomposition and regularization

We begin with the following theorem.

Theorem 5. *Let $\mathbf{A} \in \mathbb{R}^{m,n}$ and σ_k, $k = 1, \ldots, r$, be the non-null the eigenvalues of $\mathbf{A}^T\mathbf{A}$ ($r \leq \min\{m, n\}$). There exists an orthogonal base $(\mathbf{u}_k)_{k=1}^r$ of $N(\mathbf{A})^\perp$ and an orthogonal base $(\mathbf{v}_k)_{k=1}^r$ of $R(\mathbf{A})$ such that*

$$\forall k \in \{1, \ldots, r\}, \quad \mathbf{A}\mathbf{u}_k = \sigma_k\mathbf{v}_k, \quad \mathbf{A}^T\mathbf{v}_k = \sigma_k\mathbf{u}_k.$$

Theorem 5 allows an easy computation of the generalized inverse $\mathbf{A}^\dagger$: let $(\mathbf{g}_1, \mathbf{g}_2) \in \mathbb{R}^m \times \mathbb{R}^m$ and $\mathbf{g} = \mathbf{g}_1 + \mathbf{g}_2$. Let $\mathbf{f} \in N(\mathbf{A})^\perp$ such that $\mathbf{A}\mathbf{f} = \mathbf{g}$. We have

$$\mathbf{f} = \sum_{k=1}^r \langle \mathbf{f}, \mathbf{u}_k \rangle \mathbf{u}_k = \sum_{k=1}^r \frac{1}{\sigma_k} \langle \mathbf{g}, \mathbf{v}_k \rangle \mathbf{u}_k = \mathbf{A}^\dagger\mathbf{g}. \tag{1.30}$$

As in section 1.2.1, we call $(\sigma_k, \mathbf{u}_k, \mathbf{v}_k)$ the singular system of $\mathbf{A}$. Now that we have expressed the generalized inverse, we wish to investigate its stability. As the considered spaces are finite-dimensional, any linear operator is bounded. From this point of view, inverse problem (1.26)

is well-posed according to Nashed. If the observed data are noisy, *i.e.* we observe $\mathbf{g}^\delta = \mathbf{g} + \delta$ instead of $\mathbf{g}$, the error of the generalized inverse is

$$\|\mathbf{A}^\dagger \mathbf{g}^\delta - \mathbf{A}^\dagger \mathbf{g}\|^2 = \sum_{k=1}^{r} \frac{1}{\sigma_k^2} \langle \delta, \mathbf{v}_k \rangle^2.$$

If $\min\{\sigma_k\}$ is not too small, the noise effect is small and the generalized inverse can be applied. In practical case, $\mathbf{A}$ is a discrete version of an operator $\mathcal{A}$ between two Hilbert spaces of infinite dimension, which means that m and n can be arbitrary large. As the number of observations grows, the eigenvalues σ_k become smaller. Thus the generalized inverse becomes instable and a regularization is required. The regularization methods proposed in section 1.2.3.1 can be used. For example, the Tikhonov-Phillips regularization seen in example 4 consists to minimize the penalized square error

$$\|\mathbf{A}\mathbf{f} - \mathbf{g}\|^2 + \gamma \|\mathbf{f}\|^2, \tag{1.31}$$

which leads to solve the equation

$$(\mathbf{A}^T \mathbf{A} + \gamma \mathbf{I})\mathbf{f} = \mathbf{A}^T \mathbf{g}.$$

Let $\mathbf{R}_\gamma$ be the regularization of $\mathbf{A}^\dagger$ corresponding to the Tikhonov-Phillips filter. For γ small enough, we have:

$$\mathbf{R}_\gamma = (\mathbf{A}^T \mathbf{A} + \gamma \mathbf{I})^{-1} \mathbf{A}^T. \tag{1.32}$$

The SVD decomposition of $\mathbf{A}$ leads to

$$\forall \mathbf{g} \in \mathbb{R}^n, \quad \mathbf{R}_\gamma g = \sum_{k=1}^{r} \frac{\sigma_k}{\sigma_k^2 + \gamma} \langle \mathbf{g}, \mathbf{v}_k \rangle \mathbf{u}_k,$$

and the error due to noisy data can be bounded in terms of γ:

$$\begin{aligned}
\|\mathbf{R}_\gamma \mathbf{g}^\delta - \mathbf{A}^\dagger \mathbf{g}\| &\leq \|\mathbf{R}_\gamma\| \|\delta\| + \|\mathbf{R}_\gamma \mathbf{g} - \mathbf{A}^\dagger \mathbf{g}\| \\
&\leq r\|\delta\|\sigma_1/(\sigma_r + \gamma) + \gamma r \|g\| / \left(\sigma_r(\sigma_r^2 + \gamma)\right).
\end{aligned} \tag{1.33}$$

We can easily see in (1.33) the role played by γ: as it grows, the noise effect tends to be null but the approximation quality decreases. The aim is to find out a good tradeoff between the noise compensation and the quality of the approximation.

1.3.3 Bayesian approach

Excluding the semi-discrete approximate inverse where we assumed that f belongs to a subspace $X_1 \subset X$ of regular functions (see section 1.2.3.3), no prior knowledge was taken into

account for the reconstruction. In that section, we shall consider the case where both the observation vector $\mathbf{g}$ and the object $\mathbf{f}$ are random variables. As $\mathbf{g}$ is observed, the aim is to maximize the *a posteriori* distribution $p(\mathbf{f}|\mathbf{g})$ (*i.e.* the distribution of $\mathbf{f}$ when $\mathbf{g}$ remains constant) with respect to $\mathbf{f}$. We have:

$$p(\mathbf{f}, \mathbf{g}) = p(\mathbf{f}|\mathbf{g})p(\mathbf{g}) = p(\mathbf{g}|\mathbf{f})p(\mathbf{f}). \tag{1.34}$$

Thus, if $\mathbf{g}$ is fixed, the maximization of $p(\mathbf{f}|\mathbf{g})$ is equivalent to the maximization of $p(\mathbf{g}|\mathbf{f})p(\mathbf{f})$. $p(\mathbf{g}|\mathbf{f})$ is the likelihood function of the observation, and $p(\mathbf{f})$ is the *a priori* distribution of the object. The process which consists to maximize $p(\mathbf{g}|\mathbf{f})p(\mathbf{f})$ is called *maximization a posteriori* (MAP). By considering $\log(p(\mathbf{f}, \mathbf{g}))$, our problem becomes

$$\text{minimize} \quad -\log(p(\mathbf{g}|\mathbf{f})) - \log(p(\mathbf{f})), \tag{1.35}$$

which is a more general approach than minimizing (1.31).

In general, $p(\mathbf{g}|\mathbf{f})$ is known and depends on the observation device only. The choice of the *a priori* distribution $p(\mathbf{f})$ is more flexible: in some case it may be fully determined by the system (for example in Kalman filtering of a physical process), but it may also depend on which kind of regularity constraints we wish to impose on the object $\mathbf{f}$. For example, in image processing, the distribution $p(\mathbf{f})$ is often given by a *Markov field*:

Definition 11. *Let S a finite set of index, and $\mathbf{f} = (\mathbf{f}_a)_{a \in S}$ be a random vector. Let $V : S \to P(S)$ be a neighborhood structure i.e. a function that maps an element $a \in S$ to a subset $V(a)$ of S such that*

1. $\forall a \in S, a \in V(a)$

2. $\forall (a_1, a_2) \in S \times S, \quad a_1 \in V(a_2) \Leftrightarrow a_2 \in V(a_1)$

$\mathbf{f}$ *is said to be a* Markov field *with respect to V if an only if*

$$\forall a \in S, \quad p(\mathbf{f}_a|\{\mathbf{f}_b, \, b \neq a\}) = p(\mathbf{f}_a|\{\mathbf{f}_b, \, b \neq a, b \in V(a)\}).$$

In order to define a convenient Markov distribution formula, we need to define a set of self-neighboring points:

Definition 12. *Let S be a set of index, and V a neighborhood structure on S. Let $\mathbf{c}$ be a subset of S. $\mathbf{c}$ is said to be a* clique *(with respect to V) if and only if*

$$\forall (a_1, a_2) \in S \times S, \quad a_1 \in V(a_2) \quad \text{and} \quad a_2 \in V(a_1).$$

In image processing, Markov fields are widely used to model an image or a volume. A popular Markov distribution is the following:

$$p(\mathbf{f}) = \frac{1}{Z} \exp\left(\sum_{\mathbf{c}} U_{\mathbf{c}}(\mathbf{f_c})\right), \tag{1.36}$$

where $\mathbf{f_c} = \{\mathbf{f}_a, a \in \mathbf{c}\}$, and Z is a normalization constant.

Example 5.

$$p(\mathbf{f}) = \frac{1}{Z} \exp\left(-\beta \sum_{a \sim a'} \varphi(\mathbf{f}_a - \mathbf{f}_{a'})\right),$$

where $\varphi : \mathbb{R} \to \mathbb{R}^+$ and $\beta > 0$.

Equation (1.36) and example 5 raise two important issues:

- The choice of the neighborhood structure and the β function: in 3D image processing, the neighborhood of a voxel $a \in S$ contains the closest neighboring points to a, usually the 6 closest points or the 26 closest points. Large neighborhoods tend to favour an *a priori* distribution that favours smooth objects.

- The choice of the φ function is of major importance. First of all, $\varphi(\mathbf{f}_a - \mathbf{f}_{a'})$ must take large values when $|\mathbf{f}_a - \mathbf{f}_{a'}|$ is large and small values in the opposite case. Second, the behaviour of $\varphi(x)$, when x is close to 0 or to ∞, is crucial: as $\varphi(x)$ must decrease fast enough when $|x|$ tends to 0 in order to maintain image regularity, its values should not be too large as $|x|$ tends to ∞ to prevent fuzzy image shape reconstruction. In general, φ can be written as $\varphi(x) = |x|^p$. A review of image *a priori* distributions can be found in [Bouman 1993].

1.4   Conclusion

In this chapter we shortly introduced the notion of linear inverse problems and ill-posed problems. A linear inverse $g = \mathcal{A}f$ problem is ill-posed when the observation operator $\mathcal{A}$ is non-invertible or when its inverse is not bounded. In both case, its inverse $\mathcal{A}^{-1}$ or generalized inverse $\mathcal{A}^{\dagger}$ must be regularized. We identified two main categories of inverse problem: infinite and finite-dimensional. Infinite-dimensional inverse problem often involves compact operator, whose generalized inverse are not bounded. We presented several approaches to compute a regularized version of the generalized inverse, like acting on the SVD or computing the

approximate inverse. When dealing with a linear inverse problem in finite-dimensional, *i.e.* $\mathbf{g} = \mathbf{A}\mathbf{f}$ where $\mathbf{A}$ is a matrix, its generalized inverse is bounded but may be sensitive to noisy data if $\mathbf{A}^T\mathbf{A}$ contains small eigenvalues. It can basically be regularized using similar tools as the infinite-dimensional case (excepted the approximate inverse). In addition, stochastic assumption allows to interpret both $\mathbf{f}$ and $\mathbf{g}$ as random vector whose joint distribution $(\mathbf{f}, \mathbf{g})$ is known. The inverse problem can be solved throughout a maximization of the *a posteriori* distribution $p(\mathbf{f}|\mathbf{g})$.

In practical case, the data are represented by finite set of values. Therefore, if an inverse problem is to be posed as an infinite-dimensional inverse problem, the observed and object functions can be only interpreted as coordinates in a finite-dimensional subspace, or as a sample (cf the semi-discrete inverse problem). However, if the operator involved in an inverse problem is well known, its properties can be used to compute a regularized generalized inverse efficiently. In the opposite case, the inverse problem is treated as a matrix inverse problem.

Chapter 2

Tomography

2.1 Introduction

The word *tomography* comes from the ancient Greek word $\tau o \mu o s$, which means "section". Tomography is an engineering tool which aims at reconstructing an object or signal from data acquired along lines or sections, from a device named *tomograph*. Mathematically, tomography consists to recover a function $f : \mathbb{R}^n \to \mathbb{R}$ from its line integrals g_L:

$$g_L = \int_L f(x)\mathrm{d}\sigma(x), \quad L \in \mathcal{L}, \tag{2.1}$$

where $\mathcal{L}$ is a set of lines in $\mathbb{R}^n$ and σ denotes the one-dimensional Hausdorff measure (see [Federer 1969] for a definition). The set of lines $\mathcal{L}$ depends on the tomograph configuration. They can be interpreted as rays that are cast from one or several sources. The physical nature of the rays L and of the object f depends on the application. A non exhaustive list of application is presented in table 2.1. Equation (2.1) is a linear inverse problem similar to (1.2) and can be solved with the tools presented in chapter 1.

Table 2.1: Non-exhaustive list of applications of tomography

physical phenomenon	object nature	applications
X-rays	absorption function	computed tomography
gamma rays	nuclear emission function	single photon emission computed tomography positron emission tomography
seismic phases	wavespeed variations	seismic tomography

2.1.1   Physical models in medical tomography

Here we are interested by tomography in medical imaging only. We briefly introduce thus the two main modalities of tomography in medicine: *X-ray computed tomography* and *emission tomography*.

2.1.1.1   X-ray computed tomography

In X-ray computed tomography one aims at recovering an absorption function of an object. The absorbtion function of the object of interest can be enhanced by means of contrast product injected into the arteries for angiography. The measured X-ray intensity that goes through the object of interest can be calculated thanks to the *Beer-Lambert law* [Ingle 1988]:

$$I_L = I_0 \exp\left(-\int_L f(x)\mathrm{d}\sigma(x)\right), \tag{2.2}$$

where f is the attenuation function we wish to recover, L is a half-line that represents the X-ray, I_0 is the initial X-ray intensity and I_L is the measured intensity. By considering $g_L = \log(I_L) - \log(I_0)$, the inverse problem can be written as (2.1).

2.1.1.2   Emission tomography

Emission tomography aims at recovering an emission function f of the body, by introducing a positron-emitting radionuclide. $f(x)$ denotes the emission intensity at location x, and the radiation is measured by detectors outside the body, according to the following equation:

$$I_L = \int_L f(x) \exp\left(-\int_{L(x)} \mu(y)\mathrm{d}\sigma(y)\right) \mathrm{d}\sigma(x), \tag{2.3}$$

where L is the line where measurement is performed, μ is the attenuation function (which is denoted f in the previous section), $L(x)$ is the section of L between x and the detector. Equation (2.3) can be interpreted as a Beer-Lambert formula with a weight function given by $\exp\left(-\int_{L(x)} \mu(y)\mathrm{d}\sigma(y)\right)$. Therefore, the attenuation function μ has to be estimated prior to the reconstruction of the emission function f.

In positron emission tomography (PET), the positrons are emitted in opposite direction and detected at the same time. Equation 2.3 can be rewritten to

$$\begin{aligned} I_L &= \int_L f(x) \exp\left(-\int_{L^+(x)} \mu(y)\mathrm{d}\sigma(y) - \int_{L^-(x)} \mu(y)\mathrm{d}\sigma(y)\right) \mathrm{d}\sigma(x) \\ &= \exp\left(-\int_L \mu(y)\mathrm{d}\sigma(y)\right) \int_L f(x)\mathrm{d}\sigma(x), \end{aligned}$$

where $L^+(x)$ and $L^-(x)$ are the two half line sections that link x to the two opposite detectors. For the two integrals in the exponential can merge together and $L^+(x) \cup L^-(x) = L$ for all x, the weight function does not depend on x anymore and can be moved out of the main line integral. The new formula is therefore similar to the general tomographic equation (2.1).

2.2 Mathematical Models

Tomographic phenomenon can be modeled in both finite and infinite dimensions. The infinite dimension case is the most general: the object we wish to reconstruct is a function that belongs to a separable Hilbert space (square integrable function). In the n-dimensional case, the *Radon transform* is commonly used: it consists to perform integrals along and infinite set of hyperplanes which are cast parallelly. Its properties are well-known and widely used for tomographic reconstruction. For the finite dimension case, the object function is discretized in a vector $\mathbf{f}$ and the line integral operator is represented by a matrix that calculates the sums of $\mathbf{f}$ values along a finite set of lines.

2.2.1 The infinite dimension case

2.2.1.1 The X-ray transform

A natural operator in tomography is the *X-ray transform*. It calculates the integrals of an object function f in $L^2(\Omega^n)$ along lines $L_{x,\vartheta} = \{x + t\vartheta,\, t \in \mathbb{R}\}$ where the pair (x, ϑ) is such that $x \in \vartheta^\perp$.

Definition 13. *Let $T^n = \Omega^n \times S^{n-1}$. The operator $\mathcal{X} : L^2(\Omega^n) \to L^2(T^n)$ which maps any function $f \in L^2(\Omega^n)$ to $\mathcal{X}f \in L^2(T^n)$ defined by*

$$\forall (x, \vartheta) \in T^n, \quad \mathcal{X}f(x, \vartheta) = \int_{L_{x,\vartheta} \cap \Omega^3} f(y) \mathrm{d}\sigma(y),$$

where $L_{x,\vartheta}$ in a line of $\mathbb{R}^3$ defined above, is called the X-ray *transform.*

The X-ray transform $\mathcal{X} : L^2(\Omega^n) \to L^2(T^n)$ has the following properties [Natterer 1986]:

Proposition 3. *1. $\mathcal{X}$ is well defined.*

2. $\mathcal{X}$ is bounded.

3. $\mathcal{X}$ is injective.

This operator is more suitable to our vision of tomography, which aims at reconstructing an object function from its line integrals. However, it cannot be used in practice for $n \geq 3$ because it requires the knowledge of integrals of the object along every lines.

2.2.1.2 The Radon transform

The Radon transform in the n-dimensional is defined as follows (see [Natterer 1986, Natterer 1999] for details):

Definition 14. *Let Ω^n be the unit ball in $\mathbb{R}^n$ and S_+^{n-1} be the half unit sphere in $\mathbb{R}^n$. Let $Z^n =] -1, 1[\times S_+^{n-1}$ and for all $(s, \vartheta) \in Z^n$, let $\Pi_{s,\vartheta} = \{x \in \mathbb{R}^n, x \cdot \vartheta = s\}$ and σ_{n-1} be the $(n-1)$-dimensional Hausdorff measure. The operator $\mathcal{R} : L^2(\Omega^2) \to L^2(Z)$ which maps any function $f \in L^2(\Omega^n)$ to the function $\mathcal{R}f \in L^2(Z)$ defined by*

$$\forall (s, \vartheta) \in Z^n, \quad \mathcal{R}f(s, \vartheta) = \int_{\Pi_{s,\vartheta} \cap \Omega^n} f(x) \mathrm{d}\sigma_{n-1}(x)$$

is called the n-dimensional Radon transform.

The Radon transform is an operator that calculates the hyperplanes integrals of any function f in $L^2(\Omega^n)$. The parameter $\vartheta \in S_+^{n-1}$ can be interpreted as the position device from where the rays are cast, and for a fixed ϑ, $(\Pi_{s,\vartheta})_{s \in]-1,1[}$ is a family of parallel hyperplanes. For this reason, the use of the Radon transform is often related to *parallel tomography*. In 3-D tomography, the data at our disposal consists of line integrals of f. They can be grouped in integrals over planes in order to compute the Radon transform of the object and to use its mathematical properties. In 2-D tomography, the Radon transform of f is

$$\forall (s, \vartheta) \in] -1, 1[\times]0, \pi[, \quad \mathcal{R}f(s, \vartheta) = \int_{L_{s,\vartheta} \cap \Omega} f(x) \mathrm{d}\sigma(x),$$

where $L_{s,\vartheta} = \{x \in \mathbb{R}^2, \omega(\vartheta)^T \cdot x = s\}$ with $\omega(\vartheta) = (\cos(\vartheta), \sin(\vartheta))^T$ and Ω is the unit disk in $\mathbb{R}^2$. Here the half unit circle S_+^1 is replaced by $]0, \pi[$ and ϑ is an angle that gives a position on S_+^1. The set of parameters $Z =] -1, 1[\times]0, \pi[$ thus defined fits the definition 14 (figure 2.1). The Radon transform $\mathcal{R} : L^2(\Omega^n) \to L^2(Z^n)$ has the following properties [Rieder 2003a]:

Proposition 4. *1. $\mathcal{R}$ is well defined on $L^2(\Omega^n)$.*

2. $\mathcal{R}$ is injective.

3. $\mathcal{R}$ is linear a bounded operator and $\|\mathcal{R}\|^2 \leq 2\pi$.
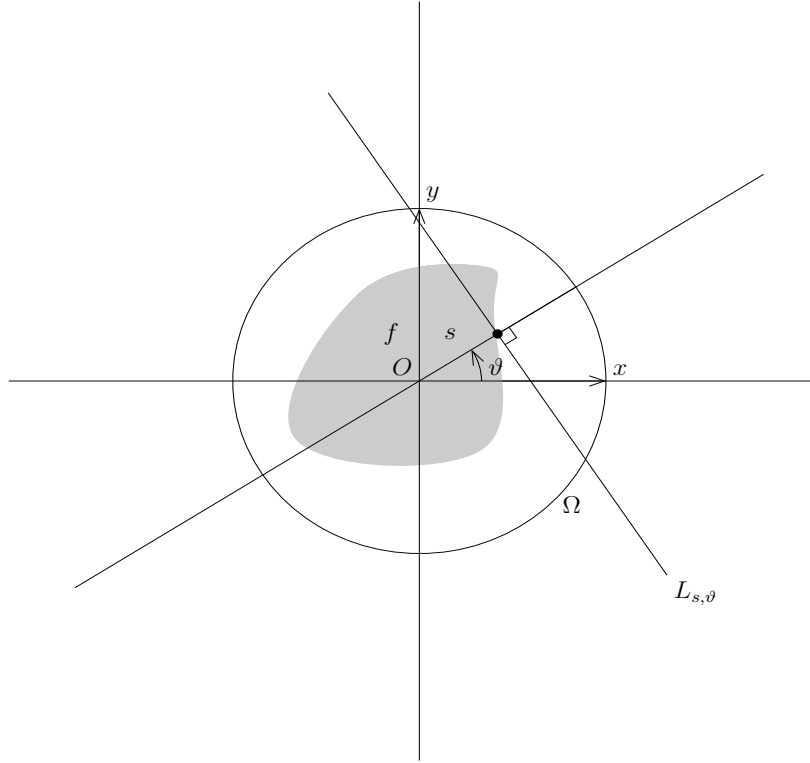
Figure 2.1: The 2-D Radon transform

4. $\dim(R(\mathcal{R})) = +\infty$

5. $\mathcal{R}$ *is a compact operator.*

The properties given in proposition 4 allow us to use the results from chapter 1. First of all, since $\mathcal{R}$ is bounded, it has an adjoint operator $\mathcal{R}^* : L^2(Z^n) \to L^2(\Omega^n)$, called the *backprojection* operator, and is defined as follows (see [Natterer 1986]):

$$\forall g \in L^2(Z^n),\ \forall x \in \Omega^n, \quad \mathcal{R}^* g(x) = \int_{S_+^{n-1}} g(x \cdot \vartheta, \vartheta) \mathrm{d}\sigma_{n-1}(\vartheta).$$

For $n = 2$, the backprojection projector is written as follows:

$$\forall g \in L^2(Z),\ \forall x \in \Omega, \quad \mathcal{R}^* g(x) = \int_{]0,\pi[} g(x \cdot \omega(\vartheta), \vartheta) \mathrm{d}\lambda(\vartheta),$$

where λ denotes the 1-dimensional Lebesgue measure. Secondly, the injectivity of $\mathcal{R}$ shows that the range of the generalized inverse $\mathcal{R}^\dagger$ is the full space $L^2(\Omega^n)$. More explicitly, we have the following inversion formula [Radon 1917, Smith 1977, Natterer 1986]:

Theorem 6. *Let $f \in L^2(\Omega^n)$ and Λ be the square root of the negative laplacian. We have*

$$f = (2\pi)^{1-n} \mathcal{R}^* \Lambda^{n-1} \mathcal{R} f. \tag{2.4}$$

For a definition of Λ refer to [Natterer 1986]. One can therefore compute the generalized inverse of the Radon transform by projecting the observation function g on the range of $\mathcal{R}$ and apply (2.4). Unfortunately, due to the compactness of the Radon transform, inverse problem

$$g = \mathcal{R} f \tag{2.5}$$

is ill-posed according to Nashed and the generalized inverse $\mathcal{R}^\dagger$ given by (2.4) has to be regularized. This cannot be done using SVD tools for the Radon transform $\mathcal{R} : L^2(\Omega^n) \to L^2(Z)$ as defined above since it has no singular value decomposition known explicitly. However, it can be shown that $\mathcal{R}$ maps $L^2(\Omega^n)$ compactly to $L^2(\widetilde{Z}^n, w^{1-n})$ (see [Davison 1981, Natterer 1986, Rieder 2000b]), where $\widetilde{Z}^n =]-1, 1[\times S^{n-1}$ and the weight is given by $w(s) = (1 - s^2)^{1/2}$ (it acts on the first variable only)[1], and its SVD decomposition can be fully expressed. Here we give the formulation of the SVD decomposition for the 2-D Radon transform [Rieder 2003a].

Proposition 5. *Let $\{u_{m,l} : m \in \mathbb{N}^*, |\ell| \le m, m + \ell \in 2\mathbb{Z}\} \subset L^2(\Omega)$ and $\{v_{m,l} : m \in \mathbb{N}^*, |\ell| \le m, m + \ell \in 2\mathbb{Z}\} \subset L^2(\widetilde{Z}, w^{-1})$ with*

$$u_{m,l}(x) = \sqrt{\frac{m+1}{\pi}} e^{\imath \ell \arg(x)} \|x\|^{|\ell|} P_{\frac{m-|\ell|}{2}}^{(0,|\ell|)} (2\|x\|^2 - 1)$$

and

$$v_{m,l}(s, \vartheta) = \frac{1}{\pi} w(s) U_m(s) e^{\imath \ell \vartheta},$$

where $U_m(s) = \sin((m+1) \arccos(s)) / \sin(\arccos(s))$ and $(P_n^{\alpha,\beta})_{n \in \mathbb{N}^*}, \alpha, \beta > -1$ denotes the Jacobi polynomials. Let

$$\sigma_m = \sqrt{\frac{\pi}{m+1}}, \quad m \in \mathbb{N}^*.$$

Then $\{u_{m,\ell}, v_{m,\ell}, \sigma_m : |\ell| \le m, m + \ell \in 2\mathbb{Z}\}$ is a singular value decomposition for $\mathcal{R} : L^2(\Omega) \to L^2(\widetilde{Z}, w^{-1})$

To our knowledge, the SVD decomposition of the Radon transform is seldom used for tomographic reconstruction. The main tool to compute a regularized generalized inverse of $\mathcal{R}$ is based on the approximate inverse seen in section 1.2.3.2, which leads to the filtered

---

[1]Here the full unit sphere S^{n-1} is considered, and depart from our definition of the Radon transform where only the half sphere S_+^{n-1} is considered.

backprojection, as we shall see in section 2.3.1.1. Note that the compacity of $\mathcal{R} : L^2(\Omega) \to L^2(Z)$ is proven thanks to this SVD decomposition, which shows that the Radon transform is the limit of a finite-rank operators sequence.

2.2.1.3 The cone-beam projector

The *cone-beam projector* is widely used in tomography. It calculates integrals of a function $f \in L^2(\Omega^3)$, where rays are cast from a single source $s(\vartheta)$ moving along a curve, such that $\|s(\vartheta)\| > 1$. The position of the emitting source is given by a parameter ϑ in $[a, b]$. The object f is projected on a plane $P(\vartheta)$ perpendicular to the axis $(O, s(\vartheta))$ (see figure 2.2) by performing the following line integrals:

$$\forall(\alpha, \vartheta) \in S^2 \times]0, \pi[, \quad \mathcal{C}f(\alpha, \vartheta) = \int_{L_{\alpha,\vartheta} \cap \Omega^3} f(x)\mathrm{d}\sigma(x), \tag{2.6}$$

where $L_{\alpha,\vartheta} = \{s(\vartheta) + t\alpha, t \in \mathbb{R}^+\}$ is emitted from a source $s(\vartheta)$. In rotational X-ray, the
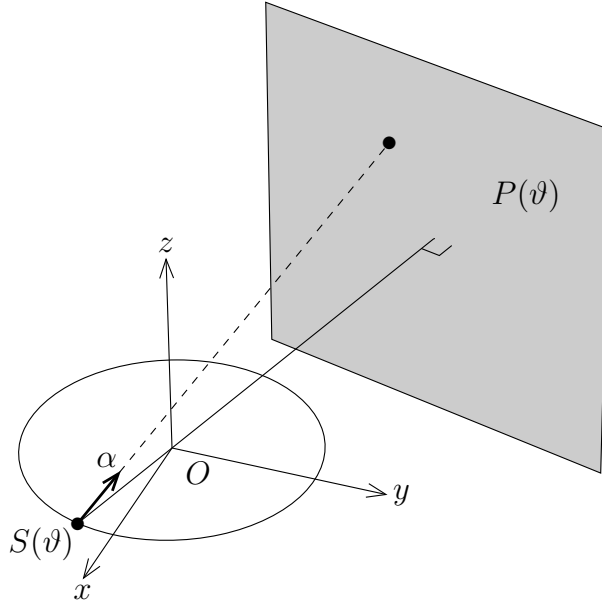

Figure 2.2: Cone-beam geometry in the case of a circular source's trajectory

source's trajectory $s : [a, b] \to \mathbb{R}^3$ is located on a circle that surrounds the object support. If s is a spiral, we deal with *helicoidal tomography*. An inversion formula is available provided that the source trajectory satisfies the *Tuy's condition*: formula (2.6) is invertible provided

that:

$$\forall (x, \alpha) \in \Omega^3 \times S^2, \quad \exists \vartheta \in [a, b], \quad (s(\vartheta) - x) \cdot \alpha = 0, \quad s'(\vartheta) \cdot \vartheta \neq 0.$$

In other words, it requires that for all x in Ω^3, each plane containing x must intersect the curve s transversally. Under these assumptions, we have the following inversion formula [Tuy 1983]:

Theorem 7. *Let* $f \in C_0^\infty (\Omega^3)$ *and* $\mathcal{C}_\vartheta$ *be the operator defined by:*

$$\forall \alpha \in S^2, \quad \mathcal{C}_\vartheta f(\alpha) = \mathcal{C} f(\alpha, \vartheta).$$

Then

$$f(x) = (2\pi)^{-3/2} \imath^{-1} \int_{S^2} (s'(\vartheta) \cdot \alpha)^{-1} \frac{\partial}{\partial \vartheta} \widehat{\mathcal{C}_\vartheta f}(\alpha) \mathrm{d}\alpha, \tag{2.7}$$

where $\vartheta = \vartheta(x, \alpha)$ *is given buy the Tuy's condition and the Fourier transform is performed with respect to* α.

The Tuy's conditions allows to use inverse formula (2.4) [Natterer 1986]. Other inversion formula of the cone-beam projector whose source's trajectory satisfies Tuy's condition can be found in [Defrise 1994] and [Katsevich 2003].

Unfortunately, the source's trajectory for the rotational X-ray projector does not satisfy Tuy's condition. For example, any plan parallel to the trajectory do not intersect the source's curve transversally. For this reason we shall not rely on this formula to compute a reconstruction algorithm.

2.2.2 The finite dimension case

2.2.2.1 The voxel representation

As mentioned in section 1.3, tomography can also be seen as finite-dimensional inverse problem: measurements consist of a finite set of values and volumes are intensity values associated to voxels. However, the real object f whose measurements are performed is infinite-dimensional. In section 1.2.2, we proposed the semi-discrete inverse problem, which consists to model the inverse problem as finite observations of a infinite-dimensional object that we reconstruct via the semi-discrete approximate inverse (section 1.2.3.3). This approach is convenient for theoretical reasons because it allows a reconstruction of the object as a function defined of Ω^n.

Another suitable approach is the following: as in practice tomography reconstructs a finite number of values, the real object $f \in L^2(\Omega)$ can thus be represented by its mean values

at each voxel index [Grangeat 2002a]. Let $\mathcal{I} = \{1, \ldots, n\}$ be the set of voxels index, and $\phi_n : L^2(\Omega) \to L^2(\Omega)$ be the *object to voxel sampling operator*, defined as follows:

$$\forall f \in L^2(\Omega), \quad \phi_n f = \sum_{i=1}^{n} u_i^n(f) w_i^n,$$

where $(w_i^n)_{i \in \mathcal{I}}$ is a set of smooth functions such that each w_i^n's support is a bounded subset of Ω which contains voxel i, and $u_i^n : L^2(\Omega) \to \mathbb{R}$.

Definition 15. *Let us assume that the pairs (w_i^n, u_i^n) are such that:*

- *$\phi_n f$ converges to f in $L^2(\Omega)$.*

- *The u_i^n's are linear operators.*

- *The w_i^n's are linearly independent with respect to i.*

- *$u_i^n(w_j) = 1$ if $i = j$ and $u_i^n(w_j) = 0$ otherwise*

Such a $(w_i^n, u_i^n)_{i \in \mathcal{I}}$ family is called a voxel basis *and $\phi_n f$ is a* voxel representation *of f.*

Example 6. Let $\aleph_i^n \subset \Omega$ be the voxel cube corresponding to voxel index i. The family of functions given by

$$\forall i \in \mathcal{I}, \quad w_i^n(x) = \begin{cases} 1 & \text{if } x \in \aleph_i^n \\ 0 & \text{otherwise} \end{cases}$$

and

$$u_i^n(f) = \frac{1}{\text{vol}(\aleph_i^n)} \int_{\aleph_i^n} f(x) \mathrm{d}\lambda(x)$$

is a voxel basis.

One can see the voxel decomposition as a particular case of the molofier decomposition $\sum_{i=1}^{d} \langle f, e_i \rangle_X b_i$ for the semi-discrete approximate inverse (section 1.2.3.3), where the e_i^d's are mollifiers and the b_i^d's are interpolation functions. However, we are interested here in the $u_i^n(f)$'s values for a given n and not for any convergence results in $L^2(\Omega^3)$, in opposition to the approximate inverse.

2.2.2.2 The projection operator

The projection operator can also be sampled in order to fit practical situations. In this section we, shall define two projection operators. The first operator, named the *object to volume*

image projection operator is a functional that maps a function of $L^2(\Omega^3)$ to a finite set of line integrals of its voxels representation. The second operator that we call the *finite dimensional projection operator* is a linear mapping between two finite-dimensional space that maps a voxel representation of a volume to a finite set of its line integrals.

Let $(w_i^n)_{i\in\mathcal{I}}$ be a voxel basis and ϕ_n be its associated volume to voxel sampling operator and let $(L_j)_{j\in\mathcal{J}}$ be a finite set of 3-D lines, where $\mathcal{J} = \{1,\ldots,m\}$. We define two operators:

- $\mathcal{P}_m : L^2(\Omega^3) \rightarrow \mathbb{R}^m$ defined by

$$\forall f \in L^2(\Omega^3), \ \forall j \in \mathcal{J}, \quad (\mathcal{P}_m f)_j = \int_{L_j \cap \Omega^3} \phi_n f(x) \mathrm{d}\sigma(x).$$

  Note that $\mathcal{P}_m$ is well defined due to the presence of ϕ_n which produces a smooth function.

- $\mathcal{P}_m^n : R(\phi_n) \rightarrow \mathbb{R}^m$ defined by

$$\forall f_n = \phi_n f \in R(\phi_n), \quad \mathcal{P}_m^n f_n = \mathcal{P}_m \phi_n f$$

Since $\dim(R(\phi_n)) = n$ and

$$(\mathcal{P}_m^n f_n)_j = \sum_{i=1}^{n} u_i^n(f) \int_{L_j \cap \aleph_i^n} w_i^n(x) \mathrm{d}\sigma(x)$$

(in the case where the support of each voxel function w_i^n is the voxel cube $\aleph_i^n$), $\mathcal{P}_m^n$ can be seen as a linear operator that maps a vector $\mathbf{f}$ of $\mathbb{R}^n$ to a vector $\mathbf{g}$ of $\mathbb{R}^m$, and therefore can be written as a $m \times n$ matrix $\mathbf{P}$, with

$$\forall (i,j) \in \mathcal{I} \times \mathcal{J}, \quad \mathbf{P}_{j,i} = \int_{L_j \cap \aleph_i^n} w_i^n(x) \mathrm{d}\sigma(x), \tag{2.8}$$

and

$$\mathbf{f} = \begin{bmatrix} u_1^n(f) \\ \vdots \\ u_n^n(f) \end{bmatrix}. \tag{2.9}$$

From now on, thanks to the voxel representation, the tomographic inverse problem can be written as a finite dimensional linear inverse problem similar to (1.26):

$$\mathbf{Pf} = \mathbf{g}, \tag{2.10}$$

and can be solved using the tools we presented in section 1.3. Depending on the tomograph and of the representation tools, the projections and object dimensions may be different. As

n and m grow, the voxel representation of the object becomes more and more accurate. One can conjecturate about the convergence of a minimal-norm solution of (2.10) to a minimal-norm solution of the infinite-dimensional inverse problem as n grows. Rigourous proof of this conjecture might be performed using tools similar as the semi-discrete approximate inverse.

2.3 Tomography: an inverse Problem

2.3.1 The infinite dimension case

Inverse problem (2.5) is ill-posed according to Nashed due to the compactness of the radon transform $\mathcal{R}$ that leads to the unboundedness of its generalized inverse. A possible interpretation of this phenomenon is that inversion formula (2.4) is unstable because of the presence of the Λ operator, which amplifies small variations of $\mathcal{R}f$. Without loss of generality, we shall focus in this section on the 2-D Radon transform.

2.3.1.1 Filtered backprojection

The *filtered backprojection* method (FBP) was first introduced by Bracewell and Riddle in 1967 in radio astronomy [Bracewell 1967]. It was later applied in medical imaging in 1974 by Shepp and Logan [Shepp 1974]. The FBP with a suitable filter can be seen as a regularization of inversion formula (2.4). It can be more rigouresly be based on the approximate inverse reconstruction: from a given mollifier function, a reconstruction kernel function is computed and convoluted with the observation data in order to estimate a smoothed version of the object. Instead of reconstructing the original function, we wish to compute its moment given by (1.14).

First let us rewrite equation (1.14) in a convolution product:

$$f_\gamma = f \star e_\gamma, \tag{2.11}$$

where $\star$ denotes the convolution product and e_γ is a mollifier. The reconstruction kernel associated to e_γ is a function v_γ such that

$$\mathcal{R}^* v_\gamma = e_\gamma.$$

Note that the convolution writing of the approximate inverse allows us to drop the y variable. The mollifier/reconstruction kernel pair can be computed by solving

$$\mathcal{R}^* v = e, \tag{2.12}$$

where e is a non-negative function with compact support that contains 0. Note that if e is a radial function, v depends on s only.

Example 7.

$$e(x) = \frac{2}{\pi}(1 - \|x\|^2)\mathbb{1}_{[0,1]}(\|x\|)$$

and

$$v(s) = \frac{1}{2\pi^2} \begin{cases} 4{}_2F_1(1, -1; 1/2; s^2) & : \quad |s| \leq 1 \\ \\ -{}_2F_1(1, 3/2; 3; 1/s^2)/s^2 & : \quad |s| > 1 \end{cases},$$

where ${}_2F_1$ denotes the hyper-geometric function. More examples can be found in [Rieder 2001].

We have the following fundamental result.

Proposition 6. *Let $e : \mathbb{R}^2 \to \mathbb{R}$ be a non-negative radial fonction with compact support that contains 0 and $v : \mathbb{R} \to \mathbb{R}$ such that its restriction to $]-1, 1[$ is in $L^2(]-1, 1[)$. Let us assume that the pair (e, v) satisfies (2.12). Then we have*

$$f \star e = \mathcal{R}^*(v \star_s \mathcal{R}f), \tag{2.13}$$

where $\star_s$ denotes the convolution product with respect to the s variable only.

Let

$$e_\gamma(x) = e(x/\gamma)/\gamma^2 \quad \text{and} \quad v_\gamma(s) = v(s/\gamma)/\gamma^2. \tag{2.14}$$

we can show that if the pair (e, v) satisfies (2.12), then the same property holds for (e_γ, v_γ):

$$\mathcal{R}^* v_\gamma = e_\gamma.$$

We finally computed an approximation of the object f from its Radon transform $\mathcal{R}f$:

$$f \star e_\gamma = \mathcal{R}^*(v_\gamma \star_s \mathcal{R}f). \tag{2.15}$$

It has be shown in section section 1.2.3.2 that the approximation given in equation (2.15) converges to f in $L^2(\Omega)$, and is stable provided that for all γ, the restriction of v_γ to $]-1, 1[$ is in $L^2(]-1, 1[)$. We call filtered backprojection any method that aims at evaluating $\mathcal{R}^*(v_\gamma \star_s g)$, where g are the observed data.

2.3.1.2 Computation of the filtered backprojection

In practical case, we are dealing with sampled data. Let us assume that the sampling of the observations are uniform, that is to say we observe $(\mathcal{R}f(s_i, \vartheta_j))_{i,j}$ at:

$$s_i = i/q, \quad \vartheta_j = j\pi/p, \quad i = -q, \ldots, q, \quad j = 0, \ldots, p-1,$$

where q and p are the sampling size with respect to s and ϑ. A natural way to estimate $\mathcal{R}^*(v_\gamma \star_s g)$ is to compute the sum

$$\mathcal{R}^*(v_\gamma \star_s g)(x) \approx \frac{\pi}{pq} \sum_{j=0}^{p-1} \sum_{i=-q}^{q} v_\gamma \left((x^T \omega(\vartheta_j) - s_i \right) g(s_i, \vartheta_j). \tag{2.16}$$

Thus written the computation time of (2.16) is very high since the kernel $(v_\gamma ((\omega(\vartheta_j) \cdot x - s_i))_{i,j}$ has to be computed for all (i, j) and for all pixels x of the image. One way to overcome this difficulty is to interpolate the sequence

$$w_\ell = \frac{1}{q} \sum_{i=-q}^{q} v_\gamma(s_\ell - s_i) g(s_i, \vartheta)$$

with respect to ℓ (see [Rieder 2001]), with B-spline functions $b(s)$:

$$\frac{1}{q} \sum_{\ell=-q}^{q} w_\ell b(qs - \ell) = \sum_{\ell=-q}^{q} \sum_{i=-q}^{q} g(s_i, \vartheta) v_\gamma(s_\ell - s_i) b(qs - \ell), \tag{2.17}$$

and then introduce (2.17) into (2.16). We finally obtain a filtered backprojection algorithm to reconstruct $f \star e_\gamma$ from g:

$$f_{fbp}(x) = \frac{\pi}{qp} \sum_{j=0}^{p-1} \sum_{\ell=-q}^{q} \left(\sum_{i=-q}^{q} g(s_i, \vartheta_j) v_\gamma(s_\ell - s_i) \right) b(qx^T \cdot \omega(\vartheta_j) - \ell). \tag{2.18}$$

The coefficients $v_\gamma(s_\ell - s_i)$ can be pre-computed and the computation speed of (2.18) is greatly improved. The gamma value in (2.18) has to be chosen carefully, depending on the sampling size. In [Rieder 2001], a method to compute an optimum γ value with respect to p and q is proposed.

2.3.1.3 Filtered backprojection for fan-beam data

Until now, we focus on a Radon transform-based tomography, which means that we assumed the acquisition geometry of the tomograph is parallel-beam. This mathematical context is ideal for it provides us good mathematical properties (existence of an inversion formula and

of a mollifier/reconstruction kernel pair). In practical case, we have to deal with non-parallel beam data: the rays are cast from a single source that rotate around the object support Ω and its position is given by the parameter $\beta \in]0, \pi[$, and its distance to the origin is fixed and is equal to r. For a given β, a single ray is given by an angle $\alpha \in] -\pi/2, \pi/2[$. Thus, we define a new projection operator $\mathcal{F}$, called the *fan-beam projector*:

$$\forall (\alpha, \beta), \quad \mathcal{F}f(\alpha, \beta) = \int_{L_{\alpha,\beta}} f(x)\mathrm{d}\sigma(x),$$

where $L_{\alpha,\beta}$ is a line defined by the parameters (α, β), according to the geometry described above (see figure 2.3). The estimation of f from $g = \mathcal{F}f$ with a filtered backprojection-like

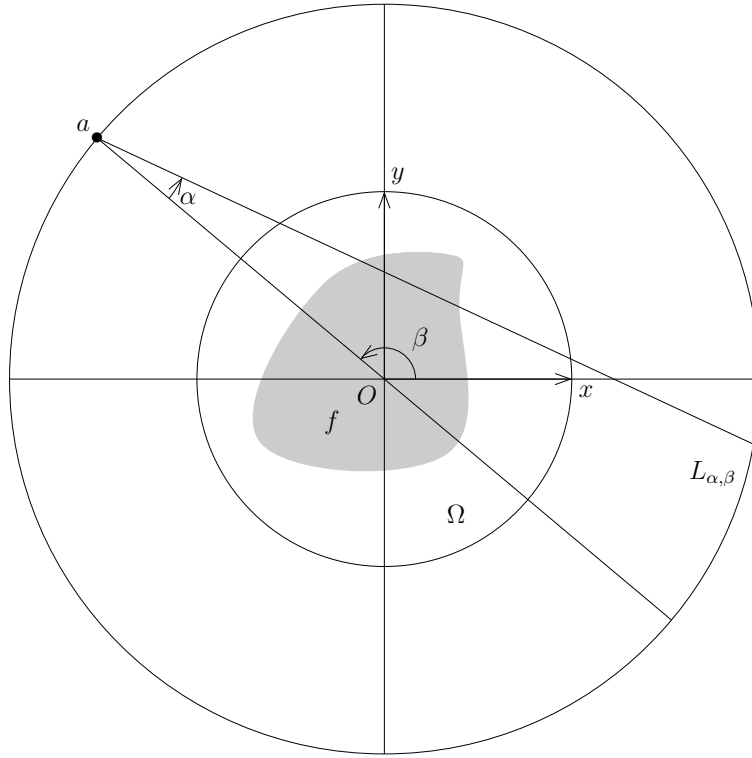Figure 2.3: The 2-D fan-beam transform

algorithm consists in a data rebinding process in order to approximate equation (2.15). First of all, any line $L_{\alpha,\beta}$ in fan-beam geometry can be associated to a line $L_{s,\vartheta}$ in parallel-beam geometry via the following parameter relationship [Natterer 1986]:

$$s = r\sin(\alpha), \quad \vartheta = \beta + \alpha - \pi/2. \tag{2.19}$$

Let (e_γ, v_γ) be a mollifier/reconstruction kernel pair for the Radon transform $\mathcal{R}$. Using (2.19), equation (2.15) can be rewritten in term of fan-beam data [Natterer 1986]:

$$\mathcal{R}^*(\mathcal{R}f \star_s v_\gamma)(x) = r \int_{]0,2\pi[} \|x - a\|^{-2} \int_{]-\pi/2,\pi/2[} v_{\|x-a\|/\gamma}(\sin(\tau(x,a) - \alpha)$$
$$\times \mathcal{F}f(\alpha, \beta) \cos(\alpha) d\lambda(\alpha) d\lambda(\beta),$$

(2.20)

where $a = r\omega(\beta)$ is the ray source position and $\tau(x, a)$ is the angle between $x - a$ and $-a$. As $v_{\|x-a\|/\gamma}$ appears in the double integral, the computation of (2.20) is far too complex and requires simplifications. First, as γ tends to zero, $\|x - a\|/\gamma$ can be replaced in (2.20) by a uniform bound $c = (1 + r)/\gamma$, which leads to

$$\mathcal{R}^*(\mathcal{R}f \star_s v_\gamma) = r \int_{]0,2\pi[} \|x - a\|^{-2} \int_{]-\pi/2,\pi/2[} v_c(\sin(\tau(x,a) - \alpha) \mathcal{F}f(\alpha, \beta) \cos(\alpha) d\lambda(\alpha) d\lambda(\beta).$$

(2.21)

Second, $\tau(x, a)$ remains present in the double integral, and should be pre-computed. This process can be performed in three steps:

1. The first integral can be approximated by

$$w_{j,k} = \frac{\pi}{2q} \sum_{\ell=-q}^{q} v_c\left(\sin(\alpha_k - \alpha_\ell)\right) \mathcal{F}f(\beta_j, \alpha_\ell) \cos(\alpha_\ell).$$

2. For each reconstruction point x, we calculate

$$k = |[q\tau(x, a_j)/2\pi]|, \quad u = |\{q\tau(x, a_j)/2\pi\}|,$$

where $a_j = r\omega(\beta_j)$.

3. The image is reconstructed with filtered backprojection:

$$f_{fbp}(x) = \frac{2r\pi}{p} \sum_{j=1}^{p} \|x - a_j\|^{-2} \left((1 - u)w_{j,k} + uw_{j,k+1}\right).$$

(2.22)

The computation of an approximate inverse from fan-beam data is more or less equivalent to data rebinding in order to recover the Radon transform.

For rotational X-ray tomography, Tuy's conditions are not satisfied, which means that such a rebinding of the cone-beam projections $\mathcal{C}f(\alpha, \vartheta)$ is impossible. To our knowledge, there are no filtered backprojection algorithm for fully 3-D reconstruction from rotational X-ray

data. Reconstruction in the cone-beam projector's orthogonal space may be possible using a suitable mollifier/reconstruction kernel pair (see [Rieder 2004] for the computation of the approximate inverse for a non-injective operator). Another approach consists to reconstruct f slice by slice: let γ_1 and γ_2 be α's angular coordinates in S^2 (γ_1 for latitude and γ_2 for longitude). The set of values $\mathcal{C}f(\alpha(\gamma_1, \gamma_2), \vartheta)$ for γ_1 fixed car be interpreted as fan-beam's projections of f on a plane parallel to the $(\overrightarrow{x}, \overrightarrow{y})$ plane, whose position is given by γ_1. f can therefore be approximatively reconstructed slice by slice using the filtered backprojection algorithm mentioned above with a suitable correction [Feldkamp 1984].

2.3.1.4 Local tomography

Local tomography aims at reconstructing Λf instead of f ($\Lambda = (-\Delta)^{1/2}$ is the square root of the negative Laplacian), and was presented for the first time in [Smith 1984]. It is applied in image processing when one wishes to reconstruct the shape of an object only. Since f and Λf have the same discontinuity, the shape of f can be obtained by reconstructing Λf only. Moreover, the reconstruction of Λf requires local data only. Local tomography is based on the inversion formula [Smith 1977]:

Theorem 8. *Let $f \in L^2(\Omega)$ and $\alpha \in \mathbb{R}$, we have:*

$$\Lambda^{-\alpha} f = (2\pi)^{-1} \mathcal{R}^* \Lambda^{1-\alpha} \mathcal{R} f. \tag{2.23}$$

The inversion formula (2.23) is a generalization of inversion formula (2.4). The computation of $\Lambda^{-\alpha} f$ can be performed with filtered backprojection (see [Ramm 1996, Rieder 2000a]).

2.3.1.5 Moment method

In previous sections we presented how to compute a regularization of the generalized inverse of the Radon transform by reconstructing its moments

$$\langle f, e_\gamma(\cdot, y) \rangle$$

on a suitable set of mollifiers. Another approach is to estimate

$$\langle f, H_n \rangle, \quad n \in \mathbb{N},$$

where $(H_n)_{n \in \mathbb{N}}$ is set of polynomials of $L^2(\Omega)$. With a suitable polynomial H_n, $\langle f, H_n \rangle$ can be expressed in terms of moments of the Radon transform $\mathcal{R}f$ on a polynomial basis of $L^2(Z)$

[Wang 2001]. More specifically, in [Shu 2006], the author proposes to reconstruct the moment

$$\lambda_{n,m}(f) = \int_\Omega P_n(x_1)P_m(x_2)f(x)\mathrm{d}\lambda_2(x),$$

where $x = (x_1, x_2)$, λ_2 is the Lebesgue measure on $\mathbb{R}^2$, and $(P_n)_{n\in\mathbb{N}}$ is a Hilbert basis of $L^2(]-1,1[)$. Note that $(P_n \otimes P_m)_{(n,m)\in\mathbb{N}^2}$ is a Hilbert basis of $L^2(\Omega)$, that is to say

$$f = \sum_{(n,m)\in\mathbb{N}^2} \lambda_{n,m}(f)P_nP_m,$$

the limit being taken in $L^2(\Omega)$. Let $g = \mathcal{R}f$ and for all ϑ in $]0,\pi[$, for all p in $\mathbb{N}$, let

$$L_p(g)(\vartheta) = \int_{]-1,1[} P_p(s)g(s,\vartheta)\mathrm{d}\lambda(s)$$

be the p-th moment of g with respect to the variable s. We have the following equality.

Theorem 9. *For all p in $\mathbb{N}$, for all ϑ in $]0,\pi[$,*

$$L_p(g)(\vartheta) = \sum_{n=0}^{p} \sum_{m=0}^{p-n} \lambda_{n,m}(f)\mu_{n,m}(p,\vartheta), \tag{2.24}$$

where $\mu_{n,m}(p,\vartheta)$ is a p-th order polynomial in $(\cos(\vartheta), \sin(\vartheta))$.

A proof of theorem 9 and a full description of $\mu_{n,m}(p,\vartheta)$ can be found in [Shu 2006].

2.3.2 The finite dimension case

2.3.2.1 Introduction

Let us recall the finite dimensional inverse problem (2.10): from a measurement vector $\mathbf{g}$, we wish to recover a volume vector $\mathbf{f}$ such that

$$\mathbf{g} = \mathbf{Pf}.$$

In section 1.3 we established the basis of the linear inverse problem in finite dimension, which aims at finding a regular version of the generalized inverse $\mathbf{A}^\dagger$, and is closely related to a regularization of the SVD decomposition of the linear operator $\mathbf{A}$. This regularization is more or less equivalent to the minimization of the regularized square error (1.31) [Louis 1989]. As such a minimizer cannot be computed directly, iterative methods are proposed.

More generally, as we have seen in section 1.3.3, instead of computing a regularization of the generalized inverse $\mathbf{A}^\dagger$, one can consider the minimization of the log-likelihood of the observation. These minimizations are mainly performed via gradient-based methods and depend on the considered distributions (section 2.3.2.3).

2.3.2.2 Resolution of the discrete tomographic inverse problem with no regularization

Solving inverse problem (1.26) can be performed by computing the generalized inverse $\mathbf{A}^{\dagger}\mathbf{g}$ of the observation vector $\mathbf{g}$. Kaczmarz's method [Kaczmarz 1937] aims at computing the generalized inverse of the following inverse problem:

$$\mathbf{g}_j = \mathbf{A}_j\mathbf{f}, \quad j = 1, \ldots, m. \tag{2.25}$$

It consists in the construction of a sequence

$$\mathbf{f}^{(k)} = \mathbf{P}_\varsigma \mathbf{f}^{(k-1)}, \tag{2.26}$$

where

$$\mathbf{P}_\varsigma = \mathbf{P}_{\varsigma,p} \ldots \mathbf{P}_{\varsigma,1}, \quad \mathbf{P}_{\varsigma,j} = (1 - \varsigma)\mathbf{I} + \varsigma\mathbf{P}_j,$$

$\mathbf{P}_j$ being the orthogonal projection on the subspace $\{\mathbf{A}_j\mathbf{f} = \mathbf{g}_j\}$ and ς is a constant relaxation parameter. Let

$$\mathbf{A} = \begin{bmatrix} \mathbf{A}_1 \\ \vdots \\ \mathbf{A}_m \end{bmatrix}.$$

If (2.26) has a solution (which is mostly the case if the inverse problem is under-determined), it can be proven that if $\mathbf{f}^{(0)}$ is in $R(\mathbf{A}^T)$ and if $\varsigma \in]0, 2[$, then $\mathbf{f}^{(k)}$ converges to the minimal norm solution of (2.26) [Natterer 1986].

In tomography, Kaczmarz's method is commonly named *Algebraic Reconstruction Technique* (ART). It consists to take $\mathbf{A}_j = \mathbf{P}_j$, the jth row of the projection matrix $\mathbf{P}$ we described in section 2.2.2.2. Although it is easy to compute and its convergence is fast, it is very sensitive to noisy data, for it converges to the generalized inverse. An improved version of this algorithm, including an object prior knowledge added to the error term, is applied in [Hansis 2007] in rotational X-ray angiography.

2.3.2.3 Resolution of discrete tomographic inverse problem with Tikhonov regularization

In section 1.3 we saw that a stable computation of the generalized inverse can be performed by minimizing the penalized least-squares error (1.31):

$$\|\mathbf{A}\mathbf{f} - \mathbf{g}\|^2 + \gamma\|\mathbf{f}\|^2,$$

For a regularization parameter γ small enough, the unique minimizer of (1.31) is given by (1.32):

$$\mathbf{R}_\gamma \mathbf{g} = (\mathbf{A}^T \mathbf{A} + \gamma \mathbf{I})^{-1} \mathbf{A}^T \mathbf{g}.$$

In tomography, the matrix $\mathbf{A}$ is replaced by a projection operator $\mathbf{P}$. Unfortunately, its dimensions can be extremely large, especially in the case of 3-D tomographic reconstruction problem, and one cannot compute the inversion of the matrix $(\mathbf{P}^T \mathbf{P} + \gamma \mathbf{I})^{-1}$. The main idea to overcome this difficulty consists to minimize (1.31) iteratively. Let us denote

$$\psi_\gamma(\mathbf{f}, \mathbf{g}) = \|\mathbf{P}\mathbf{f} - \mathbf{g}\|^2 + \gamma \|\mathbf{f}\|^2. \tag{2.27}$$

The unique minimizer of $\psi_\gamma(\mathbf{f}, \mathbf{g})$ with respect to $\mathbf{f}$ can be approximated by computing its gradient

$$\nabla \psi_\gamma(\mathbf{f}, \mathbf{g}) = 2(\mathbf{P}^T(\mathbf{P}\mathbf{f} - \mathbf{g}) + \gamma \mathbf{f}) \tag{2.28}$$

and by performing the following algorithm:

$$\mathbf{f}^{(k+1)} = \mathbf{f}^{(k)} - \delta t \nabla \psi_\gamma(\mathbf{f}^{(k)}, \mathbf{g}), \tag{2.29}$$

where δt is a non-negative constant. This algorithm is called *gradient descent* algorithm.

2.3.2.4 Resolution of discrete inverse problem with bayesian approach

In section 1.3.3, we mentioned how to model a linear inverse problem using statistical tools, such as the likelihood of the observations and the *a priori* distribution of the discretized object. Let us recall the optimization problem (1.35):

$$\text{minimize} \quad -\log(\mathrm{p}(\mathbf{g}|\mathbf{f})) - \log(\mathrm{p}(\mathbf{f})).$$

In tomography, the choice of a Markov *a priori* distribution (see (1.36)) is common since one wish to recover regular images or volumes. The choice of the observation likelihood strongly depends on the application.

In X-ray computerized tomography, the gaussian distribution is widely used. For a fixed object vector $\mathbf{f}$, we have

$$\mathbf{g}|\mathbf{f} \sim \mathcal{N}\left(\mathbf{P}\mathbf{f}, \Gamma\right),$$

where Γ denotes the covariance matrix of the observations. If Γ can be written $\Gamma = \sigma^2 \mathbf{I}$ (which is mostly the case when the observations are independent), then the minimization problem

(1.35) is a penalized least squares minimization problem, where the penalty term being the log-distribution of the object vector $\mathbf{f}$:

$$\text{minimize} \quad \frac{1}{\sigma^2}\|\mathbf{Pf} - \mathbf{g}\|^2 - \log(\mathrm{p}(\mathbf{f})).$$

If $\mathrm{p}(\mathbf{f})$ can be written as in example 1.36, then the task is

$$\text{minimize} \quad \|\mathbf{Pf} - \mathbf{g}\|^2 + \beta\sigma^2 \sum_{a\sim a'} \varphi(\mathbf{f}_a - \mathbf{f}_{a'}).$$

In practical case, the σ and β are unknown. They can be pre-estimated or estimated together with $\mathbf{f}$ as a hyper-parameter, in a joint-estimation algorithm. They can also be fixed by the user, as a tradeoff parameter between regularity of the reconstructed object and the data fidelity, as for the parameter γ in (1.31).

In emission tomography (PET or SPECT), Poisson distribution is often used to model the observation vector $\mathbf{g}$: if each projection are independently distributed we have

$$\mathbf{g}_j|\mathbf{f} \sim \text{Poisson}(\lambda_j), \quad \mathrm{p}(\mathbf{g}|\mathbf{f}) = \prod_{j=1}^{m} \mathrm{e}^{-\lambda_j} \frac{\lambda_j^{\mathbf{g}_j}}{\mathbf{g}_j!}, \quad \lambda_j = \sum_{i=1}^{n} (\mathbf{Pf})_{j,i}.$$

For both likelihood functions, one can perform a gradient based algorithm for the optimization problem (1.35). It can also be performed via a bayesian EM algorithm [Green 1990].

2.4   Conclusion

As for inverse problems, tomography can be separated into two main categories: infinite-dimensional and finite-dimensional. In infinite dimension, reconstruction methods strongly depend on our knowledge of the projection operator. In this chapter, we focused on the filtered backprojection for parallel and fan-beam projections for two-dimensional image reconstruction. The filtered backprojection allows a fast reconstruction of the object function from a mollifier/reconstruction kernel pair, for the reconstruction kernel can be pre-computed. In three dimensions, the fan-beam operator for rotational X-ray does not satisfy the Tuy's conditions so there are no direct inversion formula. The computation of an approximate inverse requires data-rebinding to recover the Radon transform, which cannot be exactly performed for our application (see the Feldkamp approximation in section 2.3.1.3). Moreover, the filtered backprojection requires to calculate integral over $]0, \pi[$, which cannot be approximated if the object is observed over a limited range. This problem is partially solved using the moment method.

The finite-dimensional tomography is much easier to manipulate. The projection operator can be modeled by a matrix as long as the locations of each line are known. The inverse problem therefore becomes less dependent of the tomograph configuration, and can be solved by a penalized least-squares minimization problem or a maximization *a posteriori* of the joint distribution of the observations and the volume. The artifact reconstruction are due to the low rank of the observation matrix, and can be compensated by using a suitable image prior, interpreted here as a regularity penalty term in the case of a least-squares minimization problem, or by an *a priori* distribution on the volume. In the next chapter we will see how to deal with dynamic object in tomographic reconstruction problem, and how to compute an object support deformation in a matrix inverse problem formulation.

Chapter 3

Dynamic Tomography

3.1 Problem statement

As tomography aims at reconstructing an object from a set of its line integral, issues encountered, except instabilities of the generalized inverses, are related to the non-injectivity of the projection operator when this set of line is not large enough (see section 2.2.1.3 for the cone-beam operator that violates Tuy's conditions for a circular source's trajectory). More difficulties appear when the object is time-dependent, for example because of organs motions or the non-stationarity of the absorption function. Those issues fall within the field of *dynamic tomography*. They correspond to a systematic "loss of injectivity" of the projection operator. It may be useful to distinguish the two following situations:

1. In PET [Jacobson 2006], all projections are performed simultaneously, but this process has to be performed over a time period that is too large to consider that the object is invariant.

2. In X-ray tomography, only a "subset of projections" can be performed simultaneously over a time interval short enough so that the object may be considered invariant, but variations between two acquisitions are too large to be neglected.

Rotational X-ray tomography, which is the topic of this work, is subject to the second kind of issues.

Let $\mathcal{P}$ be a projection operator defined over a functional space (it can be for example the Radon transform or any other projection operator). The tomographic inverse problem as we

mentioned in the previous chapter is to recover f from the measurement g such that

$$g = \mathcal{P}f. \tag{3.1}$$

Let us assume now that the object of interest f is time-dependent, that is to say f is rewritten f_t where t is a time parameter that belongs to a given time interval, which is observed through a dynamic tomographic device $\mathcal{P}_t$:

$$\forall t \in \mathcal{T}, \quad g_t = \mathcal{P}_t f_t, \tag{3.2}$$

where $\mathcal{T} = [0, T_{\mathrm{acq}}]$ is the time interval over which the projections are performed. Equation (3.2) can be interpreted as follows: the position of the tomograph is time-dependent and is therefore denoted $\mathcal{P}_t$. As the tomograph is performing projection at different position, the object is affected by a dynamic phenomenon (support deformation and intensities variation) and the measured object f_t is different from one tomograph's position to another. If one wish to reconstruct the object f_0 at time $t = 0$, the set of observed data $(g_t)_{t \in \mathcal{T}}$ as stated in (3.2) cannot be directly used and requires some pre-processing.

The main approach is to introduce a dynamic *a priori* knowledge in equation (3.2), which takes the form of an application $\mathcal{W}_t$ which maps the object f_t at time $t = 0$ to the object at any time of the acquisition process. Using this knowledge leads to a modified version of equation (3.2), which is

$$\forall t \in \mathcal{T}, \quad g_t = \mathcal{P}_t \mathcal{W}_t(f_0). \tag{3.3}$$

If $\mathcal{W}_t$ is a linear operator, equation (3.3) leads to a new linear inverse problem. Solving this new inverse problem is called *tomographic reconstruction with motion compensation*, and requires that the dynamic phenomenon is *a priori* known. The estimation of the mapping $\mathcal{W}_t$ is called *motion estimation*, and can be performed before or together with the tomographic reconstruction process.

As for inverse problem and for tomography, modeling the dynamic tomography is separated into two main categories: the infinite dimension case and the finite dimension case. In the infinite-dimensional case, we shall introduce a new projection operator, that we shall name *dynamic Radon transform*, which takes into consideration the dynamic aspects of the object. In filtered backprojection, equation (2.15) can be adapted to include the mapping $\mathcal{W}_t$ in order to solve (3.3) (see [Grangeat 2002b, Bonnet 2003, Roux 2004]).

For the finite-dimensional case, we shall focus on support deformations of the object which shall lead us to a new matrix formulation of inverse problem (2.10).

3.2 Infinite dimension

For theoretical purpose and better readability, we shall focus on 2-D tomography this section. First we shall define the dynamic Radon transform and present its fundamental properties. Its formulation is based on definition 14, with a dynamic component. As mentioned above, the position of the tomograph is time dependent. In 2-D tomography, its position is given by an angle $\vartheta \in]0, \pi[$. That is why, from now on, the time parameter t will be replaced by the angle parameter ϑ thanks to the following equality:

$$\forall t \in \mathcal{T}, \quad \vartheta(t) = \varrho \cdot t, \quad \vartheta(0) = 0, \quad \vartheta(T_{\mathrm{acq}}) = \pi, \tag{3.4}$$

where ϱ denotes the rotation speed that is assumed to be constant. A dynamic object $f_t(x)$, $t \in \mathcal{T}$ will therefore be denoted $f(x, \vartheta)$ for all $(x, \vartheta) \in \Omega \times]0, \pi[$. We assume in this work that for a given position ϑ, the projections $\mathcal{R}f(\cdot, \vartheta)(s, \vartheta)$ are acquired simultaneously for all $s \in]-1, 1[$.

Definition 16. *Let us recall notation from section 2.2.1.2 and let $\widetilde{\Omega} = \Omega \times]0, \pi[$. The dynamic Radon transform $\mathcal{R}_d : L^2(\widetilde{\Omega}) \to L^2(Z)$ is the mapping defined by*

$$\forall f \in L^2(\widetilde{\Omega}), \ \forall (s, \vartheta) \in Z, \quad \mathcal{R}_d f(s, \vartheta) = \int_{L_{s,\vartheta} \cap \Omega} f(x, \vartheta) \mathrm{d}\sigma(x).$$

The fundamental properties of the dynamic Radon transform are given in proposition 7 and theorem 10:

Proposition 7. *1. $\mathcal{R}_d$ is linear.*

2. $\mathcal{R}_d : L^2(\widetilde{\Omega}) \to L^2(Z)$ is bounded.

3. Its adjoint operator $\mathcal{R}_d^* : L^2(Z) \to L^2(\widetilde{\Omega})$ is given by

$$\forall (x, \vartheta) \in \widetilde{\Omega}, \ \forall g \in L^2(Z), \quad \mathcal{R}_d^* g(x, \vartheta) = g(x \cdot \omega(\vartheta), \vartheta). \tag{3.5}$$

4. $\mathcal{R}_d$ is non-injective.

Proof. The two first points are trivial and do not need to be proven. Let $H : L^2(Z) \to L^2(\widetilde{\Omega})$ such that

$$\forall (x, \vartheta) \in \widetilde{\Omega}, \ \forall g \in L^2(Z), \quad Hg(x, \vartheta) = g(x \cdot \omega(\vartheta), \vartheta).$$

Let f and g be two functions of $L^2(\widetilde{\Omega})$ and $L^2(Z)$ respectively. We now prove that $H = \mathcal{R}^*$:

$$
\begin{aligned}
\langle \mathcal{R}_d f, g \rangle_{L^2(Z)} &= \int_{]-1,1[} \int_{]0,\pi[} \left(\int_{L_{s,\vartheta} \cap \Omega} f(x,\vartheta) \mathrm{d}\sigma(x) \right) g(s,\vartheta) \mathrm{d}\lambda(\vartheta) \mathrm{d}\lambda(s) \\
&= \int_{]-1,1[} \int_{]0,\pi[} \int_{L_{s,\vartheta} \cap \Omega} \mathbb{1}_{\{x \cdot \omega(\vartheta) = s\}} f(x,\vartheta) g(s,\vartheta) \mathrm{d}\sigma(x) \mathrm{d}\lambda(s) \mathrm{d}\lambda(\vartheta) \\
&= \int_{]-1,1[} \int_{]0,\pi[} \int_{L_{s,\vartheta} \cap \Omega} f(x,\vartheta) g(\omega(\vartheta) \cdot w, \vartheta) \mathrm{d}\sigma(x) \mathrm{d}\lambda(s) \mathrm{d}\lambda(\vartheta) \\
&= \int_{]0,\pi[} \int_{\Omega} f(x,\vartheta) g(\omega(\vartheta) \cdot x, \vartheta) \mathrm{d}\lambda(x) \mathrm{d}\lambda(\vartheta) \\
&= \langle f, Hg \rangle_{L^2(\widetilde{\Omega})},
\end{aligned}
$$

using the fact that

$$
\forall h \in L^1(\Omega), \ \forall \vartheta \in]0, \pi[, \quad \int_{]-1,1[} \int_{L_{s,\vartheta} \cap \Omega} h(x) \mathrm{d}\sigma(x) \mathrm{d}\lambda(s) = \int_{\Omega} h(x) \mathrm{d}\lambda(x).
$$

For the non-injectivity of $\mathcal{R}_d$, it is sufficient to build a function f in $L^2(\widetilde{\Omega})$ with

$$
\mathcal{R}_d f = 0 \quad \text{and} \quad f \neq 0. \tag{3.6}
$$

One can consider a dynamic object f such that f rotates together with the detector and that returns line integrals equal to 0 almost everywhere. For example, let f in $L^2(\widetilde{\Omega})$ be defined by

$$
\forall \vartheta \in]0, \vartheta[, \quad f(x,\vartheta) = \begin{cases} 1 & \text{if } x \text{ is on the right side of the line spanned by } \omega(\vartheta + \pi/2) \\ -1 & \text{otherwise} \end{cases}
$$

(see figure 3.1).

It is obvious that f fulfils (3.6). $\qquad \square$

Theorem 10.

$$
N(\mathcal{R}_d)^\perp = \left\{ f \in L^2(\widetilde{\Omega}), \exists h \in L^2(Z), f(x,\vartheta) = h(x \cdot \omega(\vartheta), \vartheta) \right\}.
$$

Proof. First we have

$$
N(\mathcal{R}_d)^\perp = \overline{R(\mathcal{R}_d^*)}.
$$

Thanks to (3.5), we only have to prove that $R(\mathcal{R}_d^*)$ is closed in $L^2(\widetilde{\Omega})$. Let $(h_n)_n$ be a sequence of $L^2(Z)$ such that the sequence of function $(f_n)_n$ in $L^2(\widetilde{\Omega})$ defined by

$$
\forall (x,\vartheta) \in \widetilde{\Omega}, \quad f_n(x,\vartheta) = h_n(x \cdot \omega(\vartheta), \vartheta),
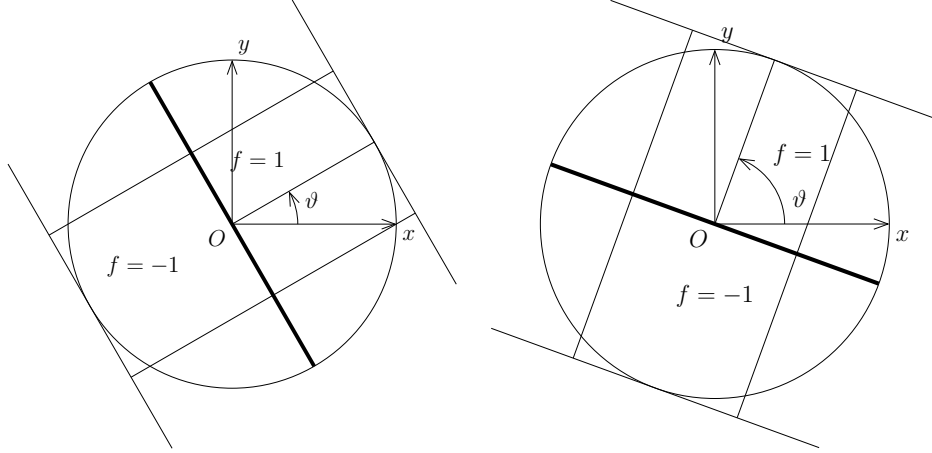$$

Figure 3.1: Non-injectivity of the dynamic Radon transform.

such that f_n converge to a given function f in $L^2(\widetilde{\Omega})$. There exists a sub-sequence $(n_k)_k$ such that f_{n_k} converges to f almost everywhere and f is measurable with respect to the sigma-field spanned by the mapping $(x, \vartheta) \mapsto (x \cdot \omega(\vartheta), \vartheta)$. Therefore there exists a function h in $L^2(Z)$ such that the limit f can be written as

$$\forall (x, \vartheta) \in \widetilde{\Omega}, \quad f(x, \vartheta) = h(x \cdot \omega(\vartheta), \vartheta).$$

$R(\mathcal{R}_d^*)$ is closed in $L^2(\widetilde{\Omega})$ and the proof is over. $\qquad\square$

Let us now consider the following inverse problem: given a function g in $L^2(Z)$, we wish to find f in $L^2(\widetilde{\Omega})$ such that

$$g = \mathcal{R}_d f. \tag{3.7}$$

Solving inverse problem (3.7) means we aim at recovering the dynamic object at each instant of the acquisition. However, one can only reconstruct a dynamic object in $N(\mathcal{R}_d)^\perp$ due to the non-injectivity of $\mathcal{R}_d$. Let f be a function in $N(\mathcal{R}_d)^\perp$. It can be noticed to notice that for a given ϑ in $]0, \pi[$, the function $f(\cdot, \vartheta)$ is constant along each line $L_{s,\vartheta}$ since $L_{s,\vartheta} = \{x \in \mathbb{R}^2, \omega(\vartheta)^T \cdot x = s\}$. Therefore inverse problem (3.7) cannot be directly solved and one must focus on the estimation of the mapping $f(\cdot, 0) \mapsto f(\cdot, \vartheta)$ or the estimation of $f(\cdot, \vartheta)$ for a given ϑ.

Although several methods of image motion compensated reconstruction on FBP-based methods have been investigated [Crawford 1996, Grangeat 2002b, Bonnet 2003, Roux 2004],

the proposed algorithms are strongly dependant of the analytical inversion (or approximation of the inversion) formula. For instance, an inversion formula that holds true in parallel-beam geometry may have no equivalent for other geometries. Moreover, the classes of transformations are often very limited (affine or piecewise-affine transformation) in order to fit inversion formulas, and do not allow non-rigid transformations. For these reasons we chose not to work in infinite-dimensional space and to focus on the finite-dimensional case.

3.3   The finite dimensional case

As for the finite dimensional case in static tomography, one can also consider the finite dimensional case in dynamic tomography. The issues we encounter are basically the same as in the infinite-dimensional case: as the tomograph is rotating around the object support, it performs projections of a different object at each position. In section 2.2.2.2 we defined the projection operator $\mathbf{P}$ as

$$\forall (i,j) \in \mathcal{I} \times \mathcal{J}, \quad \mathbf{P}_{j,i} = \int_{L_j \cap \aleph_i^n} w_i^n(x) \mathrm{d}\sigma(x).$$

where the w_i^n's are a voxel basis and the $\aleph_i^n$'s are the voxel cubes. Each row j of $\mathbf{P}$ gives the contribution of each voxel i to the j-th projection. In order to model the motion's effects in finite-dimensional tomography, the continuous observation time interval $\mathcal{T} = [0, T_{\mathrm{acq}}]$ must be discretized to

$$\mathfrak{T} = \{t_1 = 0, \ldots, t_K = T_{\mathrm{acq}}\} \subset \mathcal{T}.$$

Let us denote $\mathcal{K} = \{1, \ldots, K\}$. We define the following items:

- For all $k \in \mathcal{K}$, let $\vartheta_k \in]0, \pi[$ be the tomograph position corresponding to instant t_k, according to (3.4).

- For all $\vartheta \in]0, \pi[$, let $\mathbf{P}_\vartheta$ be the projection operator at angle ϑ.

- For all $k \in \mathcal{K}$, let $\mathcal{J}_k = \{1, \ldots, m_k\}$ be the set of lines corresponding to the device position k.

Here $L_{j,k}$ denotes the j-th ray cast from the tomograph at position k. For example, in 2-D parallel tomography, the pair of index (j, k) corresponds to a pair (s, ϑ). The projection matrix $\mathbf{P}$ can be rewritten as a concatenation of matrix $\mathbf{P}_{\vartheta_k}$'s, each of them being a (m_k, n) matrix

corresponding to a projection at position k:

$$\mathbf{P} = \begin{bmatrix} \mathbf{P}_{\vartheta_1} \\ \vdots \\ \mathbf{P}_{\vartheta_K} \end{bmatrix}.$$

The volume object $\mathbf{f}$ introduced in static modeling has to be redefined to a dynamic sequence of volume object $(\mathbf{f}_{t_k})_{t \in \mathcal{K}}$. Each volume $\mathbf{f}_{t_k}$ corresponds to a tomograph position ϑ_k, are are different from a position to another. Let us denote $\mathbf{g}_{t_k}$ the observed projections at position ϑ_k, that is to say

$$\forall k \in \mathcal{K}, \quad \mathbf{g}_{t_k} = \mathbf{P}_{\vartheta_k} \mathbf{f}_{t_k}. \tag{3.8}$$

The inverse problem associated to (3.8) consists to recover each volume vector $\mathbf{f}_{t_k}$ from the projection vectors $\mathbf{g}_{t_k}$. In section 3.3.1, we propose a method inspired from [Jin 2005] to solve this inverse problem. Another approach is to reconstruct $\mathbf{f}_{t_1}$, using a support deformation model inspired from [Jacobson 2006], which leads to a new linear inverse problem, is described in section 3.3.2.

3.3.1 Volume estimation at each state

In this section we shall give a short introduction to a method which aims at solving inverse problem (3.8). The main issue we have to deal with is the heavy ill-posedness aspect of (3.8). Indeed, the size of the observation vector $\mathbf{g} = ((\mathbf{g}_{t_1})^T, \ldots, (\mathbf{g}_{t_K})^T)^T$ is the same as in inverse problem (2.10) but the size of the object we wish to reconstruct is K times larger: instead of recovering a single volume $\mathbf{f}$ we aim at recovering a full sequence $(\mathbf{f}_{t_k})_{k \in \mathcal{K}}$. The first approach that could be considered would be to compute the regularized generalized inverse of each operator $\mathbf{P}_{\vartheta_k}$. As the rank of each matrix $\mathbf{P}_{\vartheta_k}$ is very low, this way to proceed is not accurate enough.

More generally, we can obviously notice that solving (3.8) cannot be performed unless if some assumptions on the dynamic volume $(\mathbf{f}_{t_k})_{k \in \mathcal{K}}$ are made. If the mapping $\mathbf{f}_{t_k} \mapsto \mathbf{f}_{t_{k+1}}$ is unknown as in most cases, we still can assume that the transformation is smooth *i.e.*

$$\forall k \in \{1 \ldots, K-1\}, \quad \mathbf{f}_{t_k} \sim \mathbf{f}_{t_{k+1}}. \tag{3.9}$$

In term of an optimization problem, we wish to maintain each difference $\|\mathbf{f}_{t_k} - \mathbf{f}_{t_{k+1}}\|$ low. Let

us denote $\mathbf{f} = (\mathbf{f}_{t_k})_{k \in \mathcal{K}}$ the dynamic volume and consider the minimization of the cost function

$$\psi_{\gamma,\eta}(\mathbf{f}, \mathbf{g}) = \sum_{k=1}^{K} \|\mathbf{g}_{t_k} - \mathbf{P}_{\vartheta_k} \mathbf{f}_{t_k}\|^2 + \gamma \sum_{k=1}^{K} \|\mathbf{f}_{t_k}\|^2 + \eta \sum_{k=1}^{K-1} \|\mathbf{f}_{t_{k+1}} - \mathbf{f}_{t_k}\|^2. \qquad (3.10)$$

The cost function $\psi_{\gamma,\eta}(\mathbf{f}, \mathbf{g})$ can be interpreted as the dynamic version of $\psi_\gamma(\mathbf{f}, \mathbf{g})$ in (2.27). The regularization terms $\gamma \sum_{k=1}^{K} \|\mathbf{f}_{t_k}\|$ and $\eta \sum_{k=1}^{K-1} \|\mathbf{f}_{t_{k+1}} - \mathbf{f}_{t_k}\|^2$ can be replaced by other suitable cost functions (see section 2.3.2 and [Jin 2005]).

3.3.2   Volume support deformation for motion compensation

Let us recall notations from section 3.1: at each instant $t \in \mathcal{T}$, we observe the object f_t throughout its projections g_t with projection operator $\mathcal{P}_t$

$$\forall t \in \mathcal{T}, \quad g_t = \mathcal{P}_t f_t,$$

and each object f_t is the image of the initial object f_0 throughout the transformation $\mathcal{W}_t$:

$$\forall t \in \mathcal{T}, \quad f_t = \mathcal{W}_t(f_0).$$

Let us now assume now that $\mathcal{W}_t$ is a known support deformation operator: for all t in $\mathcal{T}$ there exists a diffeomorphism $\varphi_t : \mathbb{R}^3 \to \mathbb{R}^3$ such that

$$\mathcal{W}_t(f_0) = f_0 \circ \varphi_t^{-1}. \qquad (3.11)$$

One can easily notice that $\mathcal{W}_t(f_0) = \mathcal{W}_t f_0$ is a linear transformation of f_0, and that inverse problem

$$\forall t \in \mathcal{T}, \quad g_t = \mathcal{P}_t \mathcal{W}_t f_0$$

is linear. In order to deal with a finite-dimensional linear inverse problem, the transformation $\mathcal{P}_t \mathcal{W}_t f_0$ must be transformed in a matrix product. First of all, the Hilbert space containing f_0 has to be finite dimensional. Let us consider the finite-dimensional Hilbert space E_n defined by

$$E_n = \left\{ f = \sum_{i=1}^{n} u_i^n(f) w_i^n \right\},$$

where the set of functions $(w_i^n, u_i^n)_{i=1}^{n}$ is a voxel basis (see definition 15). Thus, any function f in E_n is fully determined by its coordinates $(u_1^n(f), \ldots, u_n^n(f))$. Let f_0 the function in E_n

introduced to model the object at time $t = 0$ and let us denote

$$\mathbf{f}_0 = \begin{bmatrix} u_1^n(f_0) \\ \vdots \\ u_n^n(f_0) \end{bmatrix}.$$

The transformation $\mathcal{W}_t$ restricted to E_n can be expressed as

$$\forall f \in E_n, \quad \mathcal{W}_t f = \sum_{i=1}^n u_i^n(f) w_i^n \circ \varphi_t^{-1}. \tag{3.12}$$

Let us define the endomorphism $\widetilde{\mathcal{W}}_t : E_n \to E_n$ by

$$\forall f \in E_n, \quad \widetilde{\mathcal{W}}_t f = \phi_n \mathcal{W}_t f, \tag{3.13}$$

where $\phi_n : L^2(\Omega) \to E_n$ is the object to voxel sampling operator (see section 2.2.2.1). Let us redefine the deformed object function f_t as the voxelized version of the deformation of f_0 by the support deformation function φ_t:

$$\forall t \in \mathcal{T}, \quad f_t = \widetilde{\mathcal{W}}_t f_0. \tag{3.14}$$

Combining (3.12), (3.13), (3.14) and the linearity of the u_i^n's gives us

$$\begin{aligned} f_t &= \sum_{j=1}^n u_j^n \left(\sum_{i=1}^n u_i^n(f_0) w_i^n \circ \varphi_t^{-1} \right) w_j^n \\ &= \sum_{j=1}^n \left(\sum_{i=1}^n u_i^n(f_0) u_j^n(w_i^n \circ \varphi_t^{-1}) \right) w_j^n. \end{aligned}$$

For all t in $\mathcal{T}$, let us denote

$$\mathbf{f}_t = \begin{bmatrix} u_1^n(f_t) \\ \vdots \\ u_n^n(f_t) \end{bmatrix}. \tag{3.15}$$

According to definition 15 and (3.15), we have

$$\forall t \in \mathcal{T}, \quad \mathbf{f}_t = \mathbf{W}_t \mathbf{f}_0, \tag{3.16}$$

where $\mathbf{W}_t$ is a $n \times n$ matrix whose coefficients are

$$\forall (i,j) \in \{1, \ldots, n\}^2, \quad (\mathbf{W}_t)_{j,i} = u_j^n(w_i^n \circ \varphi_t^{-1}). \tag{3.17}$$

Note that if $t = 0$, $\varphi_0 = Id$ and $\mathbf{W}_0 = \mathbf{I}$. Therefore, the computation of the deformation of an image volume is equivalent to the computation of each $u_j^n(w_i^n \circ \varphi_t^{-1})$. Let us recall notations from section 3.3.2. The dynamic tomographic inverse problem we wish to solve is to find a suitable vector $\mathbf{f}_0$ such that

$$\forall k \in \mathcal{K}, \quad \mathbf{g}_{t_k} = \mathbf{P}_{\vartheta_k} \mathbf{W}_{t_k} \mathbf{f}_0. \tag{3.18}$$

Inverse problem (3.18) is linear and can be solved using methods we proposed in section 2.3.2.

3.4 Conclusion

The non-injectivity of the dynamic Radon transform is a major issue for dynamic tomographic reconstruction. FBP-like algorithm can solve this problem partially, but only a limited class of transformations can be considered. Working in finite-dimensional spaces is another approach that is not subject to this kind of limitations. In section 3.3.1 we briefly introduced a simple way to estimate the volume at each phase of its evolution. This method can be improved by introducing more prior knowledge, for example on the miscellaneous considered distributions. In section 3.3.2 we showed how to introduce a support deformation function in a finite dimensional dynamic tomographic inverse problem. This approach has several decisive advantages:

- The support deformation function $\varphi : \mathbb{R}^3 \to \mathbb{R}^3$ has no restriction provided it is invertible. However, in section 4.4.1 we show how to avoid this difficulty in the case of motion compensation for coronary arteries tomographic reconstruction.

- This approach is independent of the tomograph geometry: it can be applied for any projection matrix $\mathbf{P}$.

For the the two last statements hold true we chose this approach for the next chapter.

Chapter 4

Coronary arteries reconstruction from a full rotational X-ray sequence

4.1 Introduction

Coronary arterial diseases remain a major cause of mortality in Europe and in the US. Quantitative and accurate characterization (location, extent, shape, etc.) of abnormal vascular patterns (stenoses, calcifications, etc.) within the whole coronary network is thus of major importance for diagnosis and treatment. The coronary motion (related to the myocardium one) should also bring clues on irregular and/or regional abnormal dynamic beats and provide objective markers of disorders. Of course, several imaging devices, beyond X-ray systems, should be considered to fully analyze the behaviour of the beating heart like Magnetic Resonance Angiography (MRA) and 3-D ultrasound. Our work however is focussed on the X-ray based devices and its past and present contexts may be studied from different viewpoints: technology evolution, reconstruction algorithms, diagnosis and therapeutic expectations. The reconstruction problem through projections when the object is static has been addressed in previous chapters. It is much more difficult when the objective is to recover a moving object observed through sparse and sequential projections.

For a long time, the mono- and bi-plane X-ray techniques (either one source-one detector or a pair of source-detector) were available to deal with this problem. They consist to a source-

detector which can be moved by the user to acquire two or more projections at different time intervals or, for the bi-plane system (a pair of source-detector) acquired during the same time interval (thus avoiding the need for post-synchronization of the image sequences). These systems, still in use, have several advantages. They provide high quality projection images with a high time sampling rate. They also offer an efficient tool for interventions (dilation of stenoses, stent setting, etc.). If at the beginning, a subtraction technique was needed in order to eliminate the background contributions (other organs contributing to the X-ray attenuation), the recent detector advances made possible to avoid this "mask" acquisition. Background removal remains nevertheless required in current applications [Hiroshima 2001, Blondel 2006]. The major drawback of these mono or biplane techniques relies on the fact that only 2-D data are available, making difficult to precisely estimate the local lesion features.

Pioneering 3-D reconstruction attempts have been here conducted based on computer vision approaches relying on epipolar techniques and feature matching (refer to [Coatrieux 1994] for a review). They dealt first with the static reconstruction problem from two views (*i.e.* projections). To face the ill-posedness condition, prior knowledge was used with different level of granularity, from local shapes [Fessler 1989, Pellot 1994, Wahle 1996, Blondel 2006] to structural labeled tree descriptions [Smets 1990, Fessler 1991, Garreau 1991, Coppini 1991, Chen 2000]. The fragility inherent to these methods is directly related to the intra-image segmentation (see [Koller 1995, Yang 2006]) and the inter-image matching [Faugeras 1996] on one hand and on the other hand, to the validity of the models used.

Following the same line, motion estimation schemes for 3-D reconstruction and tracking have been proposed in [Ruan 1993, Ruan 1994, Shechter 2002]. The key idea behind the former work, using a biplane system, assumed that a first static reconstruction was available and from there a mixed approach, with reprojection-2-D motion tracking-3-D reconstruction of centrelines, was carried out and associated to a further refinement step. This method led to a fast and efficient scheme to recover the centrelines over the entire time sequence.

The recent availability of Rotational X (Rot-X) and Multi-Detector CT (MDCT) devices renews today the interest of the early attempts. It must be emphasized however that a first prototype, called the Dynamic Spatial Reconstructor (DSR) designed in the Mayo Clinic by E. Ritman and his team ([Block 1984] see for instance) has opened the road for such evolution. A few years later, the Morphometer project, a national initiative in France conducted between the University of Rennes 1, the LETI, CGR (Thomson) and later General Electric Medical

Systems, was launched. Its main feature was a full 2-D, standard detector rotating around the patient. The pilot device was mainly applied to static vascular networks, in particular the brain arteries. Today, marketed MDCT imaging modality can be seen basically as a diagnosis tool and makes use of electrocardiogram (ECG) gated reconstruction techniques. They provide full insights on the 3-D anatomical structures of the heart and up to 20 volumes per cardiac cycle. Although mainly devoted to diagnosis, these characteristics allow the design of pre-operative planning (see for instance [Haigron 2004]). The MDCT are not however free of artifacts due to fast heart movements and the inhomogeneities in the contrast medium distribution. Rot-X with its full 2-D detector offers joint pre-operative and intra-operative solutions. It provides during the rotation of the C-arm (over 120–220 degrees within 5–7 seconds) a high number of projections (80–160). These projections can be synchronized through ECG-gating in order to define the beating phases. Set in a given position, it is equivalent to a monoplane system. The issue is of course for us to reconstruct the coronary structures from Rot-X data projections. Several approaches can be adopted for that by:

1. Estimate the dynamic component together with the image or volume at a reference time in a joint estimation algorithm (see [Jacobson 2006] for MAP reconstruction in PET)

2. Estimate the dynamic component prior to the tomographic reconstruction, using a general dynamic model not related to the application [Crawford 1996, Grangeat 2002b, Roux 2004]

3. Carrying out a first motion estimation of the coronary tree space based on computer vision algorithms before undertaking the tomographic process (as reported in [Blondel 2004, Blondel 2006])

4. First working out the tomographic reconstruction from few views corresponding to the same heart phase [Hansis 2007, Zhou 2008] (see appendix A for [Zhou 2008]) and then estimating the motion over the sequence of reconstructed vessels for further refinement

All of them may find interest in some applications and have advantages and drawbacks in terms of robustness, accuracy, computation time, etc. The first approach mainly consists in estimating the volume and the motion iteratively until convergence. It is satisfying for theoretical reasons, for the image and the motion are estimated together, but can be also time consuming. The second approach uses information in the projection domain to estimate the dynamic

component that interfere in the reconstruction process. However, as for the first approach, models are generic and not related to the main application: a lose of crucial information about the dynamic phenomenon may occur. The third way to address the problem makes use of the principles already mentioned for biplane angiography: in short, coronary tree motion field estimation is achieved before tomographic reconstruction. The last solution consists to reverse this process: reconstruction is carried out first and a combined motion-reconstruction is then applied. The first step of this approach has been developed in [Hansis 2007, Zhou 2008] and has shown that it should offer a sound basis to work on.

Let us emphasize some other important features. We have first to deal with an extremely high volume data not only because the number of projections is high (with 2-D image size of 512×512) but also due to the volumes to reconstruct ($512 \times 512 \times 512$). In our work, due to resources limitations, we shall only deal with $192 \times 192 \times 192$ volumes. The projection geometry is a cone-beam geometry with a circular trajectory around the object od interest (see section 2.2.1.3). We may also think that in many cases, only the shapes of vessels are needed (*i.e.* the interior density values reflect the dye product concentration but does not bring relevant information except if we want to track its flow which is not the case here) but the presence of calcifications for instance obliges to accede to the density values. The product contrast is generally considered as stationary but this assumption does not hold and its validity depends on the acquisition protocol (injection mode in relation to acquisition time window). Although we will use such assumptions to solve the reconstruction problem, these limitations must be kept in mind.

In this chapter we give full details about the method we present in [Bousse 2008] and in [Bousse 2009]. Our work use both of these aspects of 3-D angiography (geometry and density values), and use a full rotational X-ray sequence. As the final reconstruction is based on motion compensated tomography (section 4.4.5), a deformable coronary 3-D model (section 4.4) is used to estimate the coronary motion that occurs during the acquisition process, and as a vessel image prior for tomographic reconstruction.

4.2 Model and assumptions

4.2.1 Preliminaries

In previous chapter 2 and chapter 3 we discussed about static and dynamic tomographic reconstruction. Both of these reconstruction problem were interpreted as linear inverse problem that could be more or less solved using approaches proposed in chapter 2. In both static and dynamic tomography we mentioned two main models: the infinite-dimensional and the finite-dimensional model.

In this chapter we shall focus on the tomographic reconstruction of coronary arteries from a single rotational X-ray sequence. As we are dealing with 3-D reconstruction only, the object support $\Omega^3 \subset \mathbb{R}^3$ shall be renamed to Ω. The object we wish to recover is an absorption function (see 2.1), from its rotational X-ray tomographic data. The injection of contrast product increases the absorption values of the coronary arteries. If we assume that there is no background effect *i.e.* the coronary arteries are immersed in an empty domain Ω with no absorption phenomenon then we can assume that the object support exactly coincides with the interior of the coronary arteries. As it has been said in section 4.1, the tomographic inverse problem cannot be directly solved and one must consider the dynamic factor.

For practical purposes, mainly for the computation of the motion compensation (see section 3.3.2), we chose to perform the tomographic reconstruction of coronary arteries using finite dimensional methods. We shall then deal with the dynamic discrete tomographic inverse problem (see (3.8)):

$$\forall k \in \mathcal{K}, \quad \mathbf{g}_{t_k} = \mathbf{P}_{\vartheta_k} \mathbf{f}_{t_k}. \tag{4.1}$$

4.2.2 ECG gating

One thing we can notice in inverse problem (4.1) is that for one instant t_k in $\mathfrak{T}$ there is only one projection $\mathbf{P}_{\vartheta_k} \mathbf{f}_{t_k}$. If we compare equation (2.10) with equation (3.2), we can see that the dynamic tomographic inverse problem involves $K = |\mathfrak{T}|$ times more unknown components than the static tomographic inverse problem. In order to reduce this K factor, several projections projections can be gathered to correspond to a same cardiac phase, which implies that the cardinal of $\mathfrak{T}$ must be lowered so that several projections can be associated to a same object state $\mathbf{f}_{t_k}$.

The main idea to lower this ratio is ECG gating. Since the motion of the coronary arteries

is due to the heart motion, we can assume that the time-dependant vector $\mathbf{f}_t$ is periodical with respect to t. Let us assume that the heart motion is T-periodical, *i.e.*

$$\forall t \in [0, (N-1)T], \quad \mathbf{f}_{t+T} = \mathbf{f}_t, \tag{4.2}$$

and that the projections are performed within the time interval $[0, NT]$, where N denotes the number of cardiac cycles during the acquisition process, and T is the duration of a cardiac cycle. In term of notations in section 4.2.1, we have

$$t_0 = 0, \quad t_K = NT, \quad \forall k \in \{1, \ldots, K\},\, t_k \in [0, NT].$$

Let S be the number of projections during a cardiac cycle. We can easily notice that $K = NS$. The time-dependant vector $\mathbf{f}_t$ is observed at regular instants $t_k = kT/S$ and equation (4.2) can be turned to

$$\forall k \in \{1, \ldots, (N-1)S\}, \quad \mathbf{f}_{t_{k+S}} = \mathbf{f}_{t_k}.$$

We can now rewrite $\mathbf{f}_{t_k}$ to $\mathbf{f}_s$, with $s = k \bmod(S)$, which shall now denotes the volume vector at phase s of the cardiac cycle.

For a given phase s in $\{1, \ldots, S\}$, let

$$\Theta_s = \{\vartheta_{1,s}, \ldots, \vartheta_{N,s}\}$$

be the projection angles corresponding to the phase s and for all subset $\Xi = \{\xi_1, \ldots, \xi_N\}$ of $]0, \pi[$, let

$$\mathbf{P}_\Xi = \begin{bmatrix} \mathbf{P}_{\xi_1} \\ \vdots \\ \mathbf{P}_{\xi_N} \end{bmatrix}$$

be the cone-beam projector at angles $\Xi = \{\xi_1, \ldots, \xi_N\}$. The volume vector $\mathbf{f}_s$ is projected N times at angles $\Theta_s = \{\vartheta_{1,s}, \ldots, \vartheta_{N,s}\}$ with the projector $\mathbf{P}_{\Theta_s}$. The gated cone-beam inverse problem at each phase s is

$$\mathbf{g}_s = \mathbf{P}_{\Theta_s} \mathbf{f}_s. \tag{4.3}$$

Thus stated, inverse problem (4.3) involves N times less unknown components than in (4.1). However, objective in this work is not to reconstruct the full sequence $(\mathbf{f}_s)_{s \in S}$. **From now on, we will focus on the reconstruction of the volume as the first cardiac phase**, that is to say we wish to estimate $\mathbf{f}_1$ at $s = 1$ from all the $\mathbf{g}_s$'s.

4.3   Static reconstruction of coronary arteries

4.3.1   Tomographic reconstruction from gated data

A natural solution for tomographic reconstruction consists in ignoring the motion effects by using gated projections at a reference time s, which is to solve inverse problem (4.3):

$$\mathbf{g}_s = \mathbf{P}_{\Theta_s}\mathbf{f}_s.$$

Let us denote $\mathbf{g}_s = ((\mathbf{g}_s)_s, \ldots, (\mathbf{g}_s)_{m_s})^T$. In [Zhou 2008], the inverse problem is solved by minimizing the *Kullback-Leiber* distance between $\mathbf{h}_s$ and $\overline{\mathbf{h}}_s(\mathbf{f}_s)$, where

$$\forall j \in \{1, \ldots, m_s\}, \quad (\overline{\mathbf{h}}_s(\mathbf{f}_s))_j \propto \exp\left(-(\mathbf{P}_{\Theta_s}\mathbf{f}_s)_j\right)$$

is the projection of $\mathbf{f}_s$ according to the Beer-Lambert law (2.2) and

$$\forall j \in \{1, \ldots, m_s\}, \quad (\mathbf{h}_s)_j \propto \exp\left(-(\mathbf{g}_s)_j\right)$$

are the observations. The aim is to minimize

$$\mathrm{KL}(\mathbf{h}_s, \overline{\mathbf{h}}_s(\mathbf{f}_s)) + \gamma \mathrm{p}(\mathbf{f}_s)$$

where

$$\mathrm{KL}(\mathbf{x}, \mathbf{y}) = \sum_j \left(x_j \log(x_i/y_i) - x_i + y_i\right).$$

The penalty $\mathrm{p}(\mathbf{f}_s)$ is given by

$$\mathrm{p}(\mathbf{f}_s) = \sum_{i \sim j} |(\mathbf{f}_s)_i - (\mathbf{f}_s)_j|^{\beta},$$

with $\beta = 1$ instead of $\beta = 2$ in order to preserve object edges. The optimization is performed by an expectation-maximization like block iterative algorithm which offers a fast convergence and a sound introduction of the non-negativity constraint for vessel attenuation coefficients. Later in this work, we will come back to this aspect by comparing gated tomographic reconstruction to our motion compensated reconstruction method (see section 4.5.4.2).

4.3.2   Vessels centrelines reconstruction using the epipolar constraint

4.3.2.1   Introduction

In this section we shall focus on the reconstruction of 3-D centrelines of coronary arteries. Instead of estimating a volume vector $\mathbf{f}_1$ at the first state $s = 1$ of the cardiac cycle, we

wish to recover a subset of 3-D points V_1 of the support Ω. This set V_1 is supposed to be a sequence of point located on the support of the coronary arteries. It can be interpreted as a set of sampled 3-D curves. In opposition to the tomographic inverse problem which aims at reconstructing a function defined on Ω, this problem is geometric.

In order to explain this problem, we need to introduce more notations, that shall also be used later along this chapter. For all angle ϑ, let us denote $P(\vartheta)$ the corresponding projection plane. A projection plane is a subset of $\mathbb{R}^3$ on which the volume in Ω is projected with the cone-beam projector. It can be interpreted from this point of view: for a given phase angle ϑ and a volume vector $\mathbf{f}$, $P(\vartheta)$ is a plane where is displayed the projection $\mathbf{P}_\vartheta \mathbf{f}$ vector values reshaped in a matrix. Now let us now define the geometric projector $\mathcal{P}_\vartheta^{\mathrm{geom}}$:

$$
\begin{aligned}
\mathcal{P}_\vartheta^{\mathrm{geom}} : \mathbb{R}^3 &\longrightarrow P(\vartheta) \\
v &\longmapsto \frac{a}{b + v_x \cos(\vartheta) + v_y \sin(\vartheta)} \left[\begin{array}{c} v_x \sin(\vartheta) - v_y \cos(\vartheta) \\ v_z \end{array} \right],
\end{aligned} \tag{4.4}
$$

where a (resp. b) is the distance of the X-ray source to the detector (resp. the center of Ω). For all $(n, s) \in \{1, \ldots, N\} \times \{1, \ldots, S\}$, let $g_{\vartheta_{n,s}}$ be the tomographic cone-beam projection of $\mathbf{f}_s$ at angle $\vartheta_{n,s}$, that is to say we have

$$
\mathbf{g}_s = \left[\begin{array}{c} g_{\vartheta_{1,s}} \\ \vdots \\ g_{\vartheta_{N,s}} \end{array} \right]
$$

where $\mathbf{g}_s$ is defined in (4.3). For this task, we also need need to have the vessels 2-D centrelines extracted on each projection plane $P(\vartheta_{1,1}), \ldots, P(\vartheta_{N,1})$ at the first cycle state: using the 2-D images corresponding to vectors $g_{\vartheta_{1,1}}, \ldots, g_{\vartheta_{N,1}}$, the 2-D centrelines are extracted on each projection plane $P(\vartheta_{1,1}), \ldots, P(\vartheta_{1,N})$. Let us denote $\mathscr{C}_1 \subset P(\vartheta_{1,1}), \ldots, \mathscr{C}_N \subset P(\vartheta_{N,1})$ the N corresponding 2-D centrelines. Note that the s index for the 2-D centrelines has been dropped for the $\mathscr{C}_n$'s since we only care about the reconstruction of the 3-D centrelines at state $s = 1$. However, the s index has been kept for the projection planes and the geometric projector, for further use.

4.3.2.2   The epipolar constraint

Let $V_1 \subset \Omega$ be the 3-D centreline we wish to reconstruct, and let us denote $\{x_1, \ldots, x_L\} = \mathscr{C}_1$ the L points of $\mathscr{C}_1$. Let us assume the following fundamental hypothesis:

$$\mathscr{C}_1 = \mathcal{P}^{\mathrm{geom}}_{\vartheta_{1,1}}(V_1), \tag{4.5}$$

which means that the 2-D centreline $\mathscr{C}_1$ comes from the geometric projection of V_1. For all ϑ, let us denote $s(\vartheta)$ the X-ray source of the cone-beam projector. For all $\ell \in \{1, \ldots, L\}$, let us denote $\mathcal{D}_\ell$ the line that joins the source $s(\vartheta_{1,1})$ to the projected point x_ℓ. According to equation (4.5), the ℓ-th point of V_1, which is denoted v_ℓ, must belong to the line $\mathcal{D}_\ell$. This constraint is commonly called the *epipolar constraint*. Therefore one must look for a solution on the line $\mathcal{D}_\ell$. Let $\{w^1_\ell, \ldots, w^M_\ell\}$ be an uniformly distributed sample of the line $\mathcal{D}_\ell$. A good candidate w^m_ℓ on $\mathcal{D}_\ell$ must have the following property: for all $n \in \{2, \ldots, N\}$, its geometric projections $\mathcal{P}^{\mathrm{geom}}_{\vartheta_{n,1}}(w^m_\ell)$ must fit the 2-D extracted centrelines $\mathscr{C}_n$ on $P(\vartheta_{n,1})$, one must look for a minimizer of the epipolar cost

$$E_{\mathrm{epipolar}}(w^m_\ell) = \frac{1}{N-1} \sum_{n=2}^{N} d^2(\mathcal{P}^{\mathrm{geom}}_{\vartheta_{n,1}}(w^m_\ell), \mathscr{C}_n) \tag{4.6}$$

with respect to m. Here $d^2(x, \mathscr{C}_n)$ is a distance function between x and $\mathscr{C}_n$. It can be for example the square distance between x and its closest point in $\mathscr{C}_n$, or more generally a mean value of the square distances between x and its closest points in $\mathscr{C}_n$. If we wish to avoid centrelines extraction on each projection plane $P(\vartheta_{n,1})$, one may consider to replace $d^2(\mathcal{P}^{\mathrm{geom}}_{\vartheta_{n,1}}(w^m_\ell), \mathscr{C}_n)$ by a response filter in the 2-D image $g_{\vartheta_{1,s}}$ which enhance values on voxels that are located on linear structures (see [Blondel 2006, Blondel 2004] and [Yang 2006] for the 3 dimensional case).

4.3.2.3   Epipolar reconstruction with vessel smoothness control

A major weakness in the reconstruction process we mentioned above is that it does not take into consideration the smoothness of the reconstructed coronary tree. More over, the number of cycles N during an acquisition process is generally small, which has the major consequence that the data cost (4.6) may lead to a wrong reconstruction. Indeed, if m is an index in $\{1, \ldots, M\}$ such that (4.6) is minimal, the number of projections $N-1$ used to evaluate if w^m_ℓ is likely to be a good candidate may not be enough. Therefore, a solution to overcome these

difficulties is to add a smoothness term which control the distance between two neighboring points in a 3-D centerline $V = \{v_1, \ldots, v_L\}$. Without loss of generality, let us assume that V is a 3-D centreline of a single vessel. In the case where V contains more than one vessel, the same method can be repeated for each vessel independently. The smoothness can be controlled by evaluating the sum of square distance between two neighboring points in V:

$$E_{\text{smooth}}(V) = \frac{1}{L-1} \sum_{\ell=2}^{L} d^2(v_\ell, v_{\ell-1}).$$

If we wish to take this sum into consideration, the criterium we wish to minimize must be calculated over all the vessel V instead of calculating a cost point by point, that is to say we wish to find a sequence $(m_\ell)_{r=\ell}^{L}$ in $\{1, \ldots, M\}^L$ which minimize the cost function

$$\frac{1}{L} \sum_{\ell=1}^{L} E_{\text{epipolar}}(w_\ell^{m_\ell}) + \lambda \frac{1}{L-1} \sum_{\ell=2}^{L} d^2(w_\ell^{m_\ell}, w_{\ell-1}^{m_\ell}). \tag{4.7}$$

The minimization of (4.7) cannot be done analytically because it is performed with respect to a variable that is discrete. However, one can interpret (4.7) as the total cost of a valued graph whose vertex are the candidates w_ℓ^m along each line $\mathcal{D}_\ell$. For $m \geq 2$ and $(m, m') \in \{1, \ldots, M\}^2$, the cost of the arc that link w_ℓ^m and $w_{\ell+1}^{m'}$ is

$$\frac{1}{L} \sum_{\ell=1}^{L} E_{\text{epipolar}}(w_{\ell+1}^{m'}) + \lambda \; d^2(w_\ell^m, w_{\ell+1}^{m'}).$$

Therefore, the minimization of (4.7) can be treated as a minimum path finding problem with a Dijkstra algorithm (see [Cormen 2001]).

4.3.3 Vessels centrelines reconstruction using a particular swarm method

The method we briefly introduce here is a preliminary work to the deformable model method we will further present in section 4.4.3. Before the reader may get confused, this method has nothing to do with particle swarm in optimization (see [Clerc 2006]). This method aims at recovering a 3-D centreline of the coronary tree from a few gated projections. As in section 4.3.2, we wish to estimate the 3-D centreline V_1 at the first cardiac phase $s = 1$. We also assume that the 2-D centrelines $\mathscr{C}_1, \ldots, \mathscr{C}_N$ have been extracted on each projection plane $P(\vartheta_{1,1}), \ldots, P(\vartheta_{1,N})$. For this purpose, we consider a swarm of mobile points $\{p_1, \ldots, p_M\} \subset \mathbb{R}^3$, uniformly distributed in a cube that contains the centreline V_1, that are "attracted" to areas where the centreline V_1 is likely to appear. As V_1 is not directly observed, this "attraction force"

is calculated according to the extracted 2-D centreline $\mathscr{C}_1, \ldots, \mathscr{C}_N$. For all m in $\{1, \ldots, M\}$, we calculate the potential of a particle p_m:

$$E(p_m) = \frac{1}{N} \sum_{n=1}^{N} d^2(\mathcal{P}_{\vartheta_{n,1}}^{\mathrm{geom}}(p_m), \mathscr{C}_n)$$

which is the mean square distance between p_m's projections on $P(\vartheta_{1,1}), \ldots, P(\vartheta_{1,1})$ to the extracted centrelines $\mathscr{C}_1, \ldots, \mathscr{C}_N$. The potential function $E : \mathbb{R}^3 \to \mathbb{R}^+$ induce an attraction field $\overrightarrow{a}$ defined by:

$$\forall x \in \mathbb{R}^3, \quad \overrightarrow{a}(x) = -\lambda \nabla \overrightarrow{E(x)},$$

where λ is a positive real value. Each particle p_m is displaced independently and iteratively in the direction of $\overrightarrow{a}(x)$, according following algorithm 1. Thus each particle is displaced

---

Algorithm 1 Particle swarm evolution algorithm

Initialize $\{p_1^{(0)}, \ldots, p_M^{(0)}\} = \{p_1, \ldots, p_M\}$

for $q = 0$ to q_{end} **do**

   for $m = 1$ to M **do**

      Compute $p_m^{(q+1)} = p_m^{(q)} + \overrightarrow{a}(p_m^{(q)})$

   end for

end for

---

until it reaches a minimal-potential area in $\mathbb{R}^3$, which corresponds to a centreline position according to the 2-D centrelines on each projection plane. Note that the loop with respect to q and m are independent and can be reversed. If the initial swarm is large enough, the 3-D centreline V_1 should be well-covered by the particles. However, in our experiments, we noticed that particles tend to converge to areas with a larger attraction potential, such as vessel bifurcations. Therefore, the particles have to be displaced with additional constraints which ensure that they remain well-distributed as they reach their target. This issue will be treated in section (4.4), by considering a vessel structure over this set of points instead of letting them move independently.

4.4 Deformable models for motion estimation

4.4.1 Introduction

In section 3.3.2 we briefly introduced how to import an object support deformation in a linear inverse problem, in order to recover the object vector $\mathbf{f}_0$ at time $t = 0$. The linear inverse problem (3.18) has been expressed in terms of coordinates of the object in a voxel basis $(w_i^n, u_i^n)_{i=1}^n$.

In section 4.2.2 we assumed that the projections could be gated according to the ECG. The dynamic volume vector $\mathbf{f}_s$ corresponds to the volume vector at phase s of the cardiac cycle, and for $s = 1$, $\mathbf{f}_1$ contains the coordinates of a function f_1 in $L^2(\Omega)$ in a voxel basis $(w_i^n, u_i^n)_{i=1}^n$:

$$\mathbf{f}_1 = \begin{bmatrix} u_1^n(f_1) \\ \vdots \\ u_n^n(f_1) \end{bmatrix}.$$

Equation (3.18) can be therefore be rewritten in term of cardiac phase:

$$\forall s \in \{1, \ldots, S\}, \quad \mathbf{g}_s = \mathbf{P}_{\Theta_s} \mathbf{W}_s \mathbf{f}_1, \tag{4.8}$$

where $\mathbf{W}_s$ is a a $n \times n$ matrix whose coefficients are

$$\forall (j, i) \in \{1, \ldots, n\}^2, \quad (\mathbf{W}_s)_{j,i} = u_j^n(w_i^n \circ \varphi_s^{-1}). \tag{4.9}$$

and $\varphi_s : \mathbb{R}^3 \to \mathbb{R}^3$ is the volume support deformation from the first cardiac phase to phase s.

Once inverse problem (4.8) has been formulated, the question that arises is how to estimate the motion function φ_s. This falls within the field of image registration. First of all, each function φ_s must belong to a suitable parametric model, in order to make the estimation. As here we are dealing with non-rigid deformations, a B-spline parametric model is suitable. However, in 4.8 only the inverse φ_s^{-1} is involved and therefore the parametric model has to be invertible (see [Narayanan 2007] for a review). The computation of such a motion is complex, and this is why we preferred to work with a motion function φ_s which maps the support of the object vector at phase any s to the support at the first phase $s = 1$. In equation (4.8), $\mathbf{W}_s$ is then redefined as follows:

$$\forall (j, i) \in \{1, \ldots, n\}^2, \quad (\mathbf{W}_s)_{j,i} = u_j^n(w_i^n \circ \varphi_s).$$

In these conditions, non-invertible B-spline models are suitable (see [Jacobson 2005, Chui 2003, Xie 2004]). In our work, we shall use cubic B-spline over a uniform grid of Ω, for the same purpose as in [Jacobson 2006], which is motion compensation in tomography. Our estimation method will be explained in section 4.4.4.

4.4.2 Coronary 3-D model

In this section we will give the definition of a *coronary 3-D model*. Basically, A coronary centreline is a set of 3-D points $V = \{v_1, \ldots, v_L\}$ that are supposed to represent a coronary tree. In order to define a coronary 3-D model based on V, we have to define a *vessel structure*.

Definition 17. *Let $\mathfrak{L} = \{1, \ldots, L\}$ be a set of index on a centreline. Let $J \in \mathbb{N}^*$ and $(I_j)_{j=1}^J \in (\mathbb{N}^*)^J$ such that*

$$\sum_{j=1}^{J} I_j = L.$$

Let $\mathfrak{O}$ be the set of pairs $(j, i) \in \{1, \ldots, J\} \times \mathbb{N}^*$ such that

$$i \in \{1, \ldots, I_j\}$$

holds true. A vessel structure on V *is an application*

$$
\begin{aligned}
\mathcal{V} : \mathfrak{L} &\longrightarrow \mathfrak{O} \\
\ell &\longmapsto (\mathcal{V}_{\mathrm{br}}(\ell), \mathcal{V}_{\mathrm{pos}}(\ell))
\end{aligned}
$$

which is a bijection. For all ℓ in $\mathfrak{L}$, $\mathcal{V}_{\mathrm{br}}(\ell)$ denotes ℓ's branch number and $\mathcal{V}_{\mathrm{pos}}(\ell))$ denotes its position on a branch. Moreover, two index ℓ and ℓ' are said to be neighbours with respect to $\mathcal{V}$ *if and only if*

$$\mathcal{V}_{\mathrm{br}}(\ell) = \mathcal{V}_{\mathrm{br}}(\ell') \quad \text{and} \quad |\mathcal{V}_{\mathrm{pos}}(\ell) - \mathcal{V}_{\mathrm{pos}}(\ell')| = 1,$$

i.e. ℓ and ℓ' are consecutive index on the same branch.

Thus we define a vessel structure $\mathcal{V}$ as a "partitioning" of a centreline: each index ℓ is given a branch number and a position on this branch. For all j, I_j is the number of elements in the j-th branch. We can now define a coronary 3-D model.

Definition 18. *Let $V = \{v_1, \ldots, v_L\}$ be a coronary centreline and $\mathcal{V}$ a vessel structure on V. The pair $(V, \mathcal{V})$ is called a* coronary 3-D model.

4.4.3 The proposed deformation model

In section 4.3.2 we defined V_1 as the 3-D centreline corresponding do the volume $\mathbf{f}_1$ at the first cardiac phase. More generally, we denote V_s the centreline of each volume $\mathbf{f}_s$ at any phase s. In order to estimate each motion function φ_s, we propose the following process. Each coronary 3-D centrelines $V_s = \{v_1^s, \ldots, v_L^s\}$ at phases $s \in \{2, \ldots, S\}$ are estimated from successive deformations of V_1, using the gated projections at angles Θ_s, **assuming V_1 is already known**. Proceeding this way allows each point v_ℓ^1 of V_1 to be tracked in time and to build a time-sequence $v_\ell^1 \in V_1, \ldots, v_\ell^S \in V_S$ for each $\ell \in \{1, \ldots, L\}$, which makes the estimation of a motion function $\varphi_s : \mathbb{R}^3 \to \mathbb{R}^3$ more simple. This knowledge is unavailable if the 3-D centrelines V_s are to be reconstructed one by one independently, for example using the epipolar constraint at each phase s, unless if a one to one correspondence between each V_s and V_1 is established afterwards. **From now on we assume that each coronary 3-D model has the same vessel structure $\mathcal{V}$**, *i.e.* each centreline V_s's branches and neighbouring points are defined the same way. Therefore, for all s in $\{1, \ldots, S\}$, V_s denotes the coronary 3-D model as phase s with the vessel structure $\mathcal{V}$.

The deformation to estimate V_s from V_{s-1} is based on the minimization of a cost function $\mathbf{D}_s$, and its minimization is performed via a gradient-based algorithm. This cost function is written as the following sum

$$\mathbf{D}_s(V) = \mathbf{E}_s(V) + \kappa \mathbf{F}(V), \tag{4.10}$$

where $\mathbf{E}_s(V)$ is the data fidelity term with respect to the projections at angles Θ_s and $\mathbf{F}$ is a smoothness cost on V. Here we chose to let $\mathbf{F}(V)$ independent of s because we assumed that the regularity of a 3-D model does not depend on the cardiac phase. During the minimization process, each point v_ℓ^{s-1} of V_{s-1} are displaced under the constraint the cost function $\mathbf{D}_s$ properties, and for all ℓ in $\{1, \ldots, L\}$ a sequence $(v_\ell^{(q)})_{q \in \mathbb{N}}$ describe the displacement of v_ℓ^{s-1}, where q denote the iteration number. For a q value large enough, the algorithm has converged and $v_\ell^{(q)}$ has reached its final target, which becomes v_ℓ^s

4.4.3.1 Data fidelity

Let us denote $V = \{v_1, \ldots, v_L\} \subset \Omega$ a coronary 3-D model, with vessel structure $\mathcal{V}$, and let us assume that we wish to estimate V_s, the 3-D centreline model at phase s. For all ϑ in $]0, \pi[$, let $D_\vartheta : P(\vartheta) \to \mathbb{R}_+^*$ be a function such that $D_\vartheta(x)$ is small when x is located in the

neighborhood of a projected vessel in $P(\vartheta)$ and large when x is in the background. We can now define the data cost of a point v in Ω with respect to the projections at phase s:

$$E_s(v) = \frac{1}{N} \sum_{n=1}^{N} D_{\vartheta_{n,s}}(\mathcal{P}_{\vartheta_{n,s}}^{\mathrm{geom}}(v)). \tag{4.11}$$

According to E_s definition, it returns small values for v's such that their projections fit the projected vessels on planes $P(\vartheta_{1,s}), \ldots, P(\vartheta_{1,s})$. The data fidelity cost $\mathbf{E}_s(V)$ is thus given by:

$$\mathbf{E}_s(V) = \frac{1}{|V|} \sum_{v \in V} E_s(v).$$

We now define the "distance" function D_ϑ used in (4.11). First let us consider the case where branches are not identified on the 2-D projections and there are no correspondence established between the extracted branches and the branches of the 3-D deformable model. Let v_ℓ be a point of V, and $h_{\vartheta,\ell} = \mathcal{P}_\vartheta^{\mathrm{geom}}(v_\ell)$ be its projection on $P(\vartheta)$. Let us denote $\mathcal{H}_\vartheta = \mathcal{P}_\vartheta^{\mathrm{geom}}(V)$ the projection of V on $P(\vartheta)$. Since we assumed that the centrelines have been extracted on each projection plane $P(\vartheta)$, we can calculate a distance function between $h_{\vartheta,\ell}$ and the extracted centrelines. Let $\mathcal{C}_\vartheta \subset P(\vartheta)$ be the set of points of the extracted centrelines on projection plane $P(\vartheta)$. A natural way to define a distance between each point $h_{\vartheta,\ell} \in \mathcal{H}_\vartheta$ and $\mathcal{C}_\vartheta$ would be $D_\vartheta(h_{\vartheta,\ell}) = \min_{c \in \mathcal{C}_\vartheta} \|h_{\vartheta,\ell} - c\|^2$. However, this distance depends of the point $c \in \mathcal{C}_\vartheta$ that minimizes $\|h_{\vartheta,\ell} - c\|$ and c may belong to a wrong branch. To overcome this difficulty, we propose another distance function. Let us assume we are estimating V_s from V_{s-1}. Let $v_\ell^{(q)}$ be a point of a 3-D coronary skeleton $V^{(q)}$ at iteration q of the deformation algorithm, and $h_{\vartheta,\ell}^{(q)} = \mathcal{P}_\vartheta^{\mathrm{geom}}(v_\ell^{(q)})$. Remember that $v_\ell^{(q)}$ is a result of a displacement of $v_\ell^{s-1} \in V_{s-1}$, which is the last element of the sequence $v_\ell^1 \in V_1, \ldots, v_\ell^{s-1} \in V_{s-1}$. Let $c_1(\vartheta, \ell, q), \ldots, c_{n_{\min}}(\vartheta, \ell, q)$ be the $n_{\min}$ closest points to $h_{\vartheta,\ell}^{(q)}$ in $\mathcal{C}_\vartheta$: we define $D_\vartheta(h_{\vartheta,\ell}^{(q)})$ by the weighted sum

$$D_\vartheta(h_{\vartheta,\ell}^{(q)}) = \frac{1}{\Gamma(\vartheta, \ell, q)} \sum_{i=1}^{n_{\min}} \gamma_i(\vartheta, \ell, q) \|h_{\vartheta,\ell}^{(q)} - c_i(\vartheta, \ell, q)\|^2, \tag{4.12}$$

where $\Gamma(\vartheta, \ell, q) = \sum_{i=1}^{n_{\min}} \gamma_i(\vartheta, \ell, q)$. A high $\gamma_i(\vartheta, \ell, q)$ value means that $c_i(\vartheta, \ell, q)$ is likely to be a good target for $h_{\vartheta,\ell}^{(q)}$. The weights $\gamma_i(\vartheta, \ell, q)$ may depend of local properties of $\mathcal{C}_\vartheta$ and of $\mathcal{H}_\vartheta^1 = \mathcal{P}_\vartheta^{\mathrm{geom}}(V_1)$, the projection of the initial coronary skeleton, such as the vessel local direction. Let $\overrightarrow{\mathrm{dir}}(h_{\vartheta,\ell}^1|\mathcal{H}_\vartheta^1)$ be the vessel direction of $\mathcal{H}_\vartheta^1$ at $h_{\vartheta,\ell}^1$ and $\overrightarrow{\mathrm{dir}}(c_i(\vartheta, \ell, q)|\mathcal{C}_\vartheta)$ be the direction of $\mathcal{C}_\vartheta$ at $c_i(\vartheta, \ell, q)$: we choose $\gamma_i(\vartheta, \ell, q) = 1/\left(\|\overrightarrow{\mathrm{dir}}(h_{\vartheta,\ell}^1|\mathcal{H}_\vartheta^1) - \overrightarrow{\mathrm{dir}}(c_i(\vartheta, \ell, q)|\mathcal{C}_\vartheta)\|_1 + 1\right)$.

If the branches are labeled on each projections (see [Garreau 1991] for the vessels labeling on projections), one can use this crucial information for the calculation of D_ϑ. Let us assume

that $\mathscr{C}_\vartheta$ can be separated in J 2-D branches $\mathscr{B}_{\vartheta,1}, \ldots, \mathscr{B}_{\vartheta,J}$ such that each $\mathscr{B}_{\vartheta,j}$ corresponds to the j-th 3-D branch according to vessel structure $\mathcal{V}$. Let v_ℓ be a point of V, such that $\mathcal{V}_{\mathrm{br}}(\ell) = j$: v_ℓ corresponds to the 2-D branche $\mathscr{B}_{\vartheta,j} = \left\{ b^\vartheta_{j,1}, \ldots, b^\vartheta_{j,I_{j,\vartheta}} \right\}$. One can define D_ϑ by

$$D_\vartheta(\mathcal{P}^{\mathrm{geom}}(v_\ell)) = \min_{i=1,\ldots,I_{j,\vartheta}} \left\{ d^2(\mathcal{P}^{\mathrm{geom}}(v_\ell), b^\vartheta_{j,i}) \right\}. \tag{4.13}$$

4.4.3.2 Vessels smoothness

A major issue in the process we described in section 4.4.3 is the choice of a smoothness cost function F. As each 3-D model V_s is estimated from successive deformations of the original 3-D model, one may feel concern that for a high s value, the 3-D estimated centreline might be degenerate. For example, as s grows, subsets of points v^s_ℓ of V_s may tend to concentrate in some regions of Ω where 3-D points have a small E_s value, and the distribution of the 3-D points may become not regular.

A first natural smoothness function can be defined by penalizing a 3-D model whose neighboring points are far from each others. Let us recall the vessel structure $\mathcal{V}$ and denote

$$\Upsilon(\mathcal{V}) = \{ \iota = \{\iota_1, \iota_2\} \subset \{1, \ldots, L\}, \, \iota_1 \sim \iota_2 \}$$

the set of cliques in $\{1, \ldots, L\}$, according to the topological structure we defined above in definition 17. Moreover, let $\psi : \mathbb{R}^+ \to \mathbb{R}^+$ be a non-decreasing function. We now define the cost function $\mathbf{F}_1$ by

$$\mathbf{F}_1(V) = \frac{1}{|\Upsilon(\mathcal{V})|} \sum_{\iota \in \Upsilon(V)} \psi(\|v_{\iota_1} - v_{\iota_2}\|). \tag{4.14}$$

However, the cost function $\mathbf{F}_1$ as stated in (4.14) cannot be directly used, because its minimizers do not satisfy the regularity properties we are aiming to obtain. For example, if V is such that $\forall(\ell, \ell') \in \{1, \ldots, L\}^2$, $v_\ell = v_{\ell'}$, then $\mathbf{F}_1(V) = 0$. Therefore all points of V may converge to a same point that fit the projection data at phase s. In section 4.4.3.3 we shall present a solution to compensate this issue, by acting on endpoints of each branches.

Another approach is to design the smoothness cost function $\mathbf{F}$ such that its minimizers maintain the same distance between two neighboring point for all clique, that is to say

$$\exists C \in \mathbb{R}^+, \quad \forall \iota \in \Upsilon(\mathcal{V}), \quad d(v_{\iota_1}, v_{\iota_2}) = C. \tag{4.15}$$

Naturally, such a C constant is unknown, but fulfilling (4.15) can be performed from a stochastic point of view. Let $\xi_V : \Upsilon(\mathcal{V}) \to \mathbb{R}^+$ which maps a clique ι to the square distance between

the 3-D points indexed by ι_1 and ι_2:

$$\forall \iota \in \Upsilon(\mathcal{V}), \quad \xi_V(\iota) = \psi(\|v_{\iota_1} - v_{\iota_2}\|).$$

One can interpret ξ_V as a random variable defined on the probability space $(\Upsilon(\mathcal{V}), P(\Upsilon(\mathcal{V})), \mu)$ where $P(\Upsilon(\mathcal{V}))$ denotes the sigma-field of $\Upsilon(\mathcal{V})$'s subsets and μ denotes the uniform discrete probability measure on $(\Upsilon(\mathcal{V}), P(\Upsilon(\mathcal{V})))$. Fulfilling (4.15) is then equivalent to

$$\mathbb{V}(\xi_V) = \frac{1}{|\Upsilon(\mathcal{V})|} \sum_{\iota \in \Upsilon(V)} (\xi_V(\iota) - \mathbb{E}(\xi_V))^2 = 0,$$

where

$$\mathbb{E}(\xi_V) = \frac{1}{|\Upsilon(\mathcal{V})|} \sum_{\iota \in \Upsilon(\mathcal{V})} \xi_V(\iota)$$

is the mean value of ξ_V. A smoothness cost function can be then given by

$$\mathbf{F}_2(V) = \sqrt{\mathbb{V}(\xi_V)}. \tag{4.16}$$

As for the previous smoothness cost function, we can notice that a coronary 3-D model whose points are all concentrated on a single point satisfies $\mathbf{F}_2(V) = 0$. We shall also rely on section 4.4.3.3 for this issue.

The final approach we propose is a cost function $\mathbf{F}_3$ which aims at regularizing the 3-D model displacement from the starting 3-D model V_1. For all $\ell \in \{1, \ldots, L\}$, we can calculate the motion vector function $\mathfrak{D}_\ell$ at each point v_ℓ of the deformable 3-D model V:

$$\mathfrak{D}_\ell(v_\ell) = v_\ell - v_\ell^1.$$

Finally, we propose a smoothness cost function can be given by

$$\mathbf{F}_3(V) = \frac{1}{|\Upsilon(\mathcal{V})|} \sum_{\iota \in \Upsilon(V)} \psi(\|\mathfrak{D}_{\iota_1}(v_{\iota_1}) - \mathfrak{D}_{\iota_2}(v_{\iota_2})\|). \tag{4.17}$$

4.4.3.3 Endpoints

In section 4.4.3.2 we mentioned a fundamental issue du to the fact that the points of a 3-D model V may converge to a single point in Ω which fits the projections. This is mainly because the total cost function $\mathbf{D}_s$ does not take into consideration the length of the vessels. Therefore, a special treatment must be assigned to both endpoints of each vessel. We need to assume that on each projection plane $P(\vartheta_{n,s})$ the localization of endpoints are approximately known.

Thus, we can redefine the energy function E_s of a border point: let $v_{\ell_{\text{start}}}$ be the first point in the j-th branch of V, and $v_{\ell_{\text{end}}}$ the last point:

$$\mathcal{V}_{\text{br}}(\ell_{\text{start}}) = j, \qquad \mathcal{V}_{\text{br}}(\ell_{\text{end}}) = j,$$
$$\mathcal{V}_{\text{pos}}(\ell_{\text{start}}) = 1, \qquad \mathcal{V}_{\text{pos}}(\ell_{\text{end}}) = I_j$$

(see definition 17 for the notations). The energy of $v_{\ell_{\text{start}}}$ and $v_{\ell_{\text{end}}}$ at phase s we used are

$$E_{s,j}^{\text{start}}(v_{\ell_{\text{start}}}) = \sum_{n=1}^{N} \zeta_{j,\text{start}}^{n,s} \| \mathcal{P}_{\vartheta_{n,s}}^{\text{geom}}(v_{\ell_{\text{start}}}) - b_{j,\text{start}}^{n,s} \|^2$$

and

$$E_{s,j}^{\text{end}}(v_{\ell_{\text{end}}}) = \sum_{n=1}^{N} \zeta_{j,\text{end}}^{n,s} \| \mathcal{P}_{\vartheta_{n,s}}^{\text{geom}}(v_{\ell_{\text{end}}}) - b_{j,\text{end}}^{n,s} \|^2$$

where $b_{j,\text{start}}^{n,s}$ (resp. $b_{j,\text{end}}^{n,s}$) denotes an estimation of the first (resp. the last) point of the extracted branch j on projection plane $P(\vartheta_{n,s})$, and where $\zeta_{j,\text{start}}^{n,s}$ (resp. $\zeta_{j,\text{end}}^{n,s}$) is a non-negative normalized sequence (with respect to n) which takes large values if $b_{j,\text{start}}^{n,s}$ (resp. $b_{j,\text{end}}^{n,s}$) is likely to be a correct starting (resp. ending) point for the branch j on $P(\vartheta_{n,s})$ and small values otherwise.

4.4.3.4 Proposed algorithm

The algorithm we propose to minimize $\mathbf{D}_s$ is mainly based on the gradient-descent method. Each point v_ℓ of the deformable model V are moved one by one, in the direction of $\nabla_\ell \mathbf{D}_s(V)$, which denotes the gradient of $\mathbf{D}_s$ with respect to v_ℓ. Let V_s^κ be a minimizer of $\mathbf{D}_s$ (see (4.10) for the definition of κ). Depending on the κ value, V_s^κ should satisfy

$$\mathbf{E}_s(V_s^\kappa) \simeq 0. \tag{4.18}$$

It is obvious that (4.18) is fulfilled provided that $\kappa = 0$. On the contrary, if κ is large, the regularization cost will have more importance in the minimization of $\mathbf{D}_s$ and (4.18) will have no chance no hold. In practical case, κ is a small parameter, so we can assume reasonably that (4.18) is fulfilled. Therefore, a suitable gradient step for each gradient direction $\nabla_\ell \mathbf{D}_s(V)$ would be $\lambda E_s(v_\ell^{(q)})^{1/2}$, where λ is a positive real value and q is the iteration number. Such a gradient step value would allow the point displacement to slow down as they are closing to their target, and then prevent any oscillation effect around the minimizer location. We propose algorithm 2 for our deformable model. For each phase $s \geq 2$, the number of iteration is equal to q_{end}.

Algorithm 2 3-D model deformation algorithm

   for $s = 2$ to S **do**

     Initialize $V^{(0)} = V_{s-1}$

     for $q = 0$ to q_{end} **do**

       for $\ell = 1$ to L **do**

         $\delta_{q,\ell} = E_s(v_\ell^{(q)})$

         $v_\ell^{(q+1)} = v_\ell^{(q)} - \delta_{q,\ell}\lambda\nabla_\ell\mathbf{D}_s(V^{(q)})$

       end for

     end for

     $V_s = V^{(q)}$

   end for

4.4.4 Motion estimation

Point matching registration differs from classical image registration. As image registration focus on the estimation of a diffeomorphism $\varphi : \mathbb{R}^p \to \mathbb{R}^p$ (with $p = 2$ or $p = 3$) which approximatively maps the support of an given source image $f_1 : \mathbb{R}^p \to \mathbb{R}$ to a given target image $f_2 : \mathbb{R}^p \to \mathbb{R}$, *i.e.*

$$f_2 \simeq f_1 \circ \varphi^{-1},$$

(see [Peckar 1998, Kybic 2003, Jacobson 2005, Xie 2004] for non-rigid registration, [Maes 1997, Roche 1998, Klein 2000, Sabuncu 2005] for rigid registration), point matching registration deals with geometric entities (points, curves, etc.): given a 2-D or 3-D source object $O_1 \subset \mathbb{R}^p$ and a target object $O_2 \subset \mathbb{R}^p$, we wish to estimate a function $\varphi : \mathbb{R}^3 \to \mathbb{R}^3$ such that

$$\varphi(O_1) \simeq O_2.$$

The estimation of φ is performed by establishing "correspondences" between each points of the two sets O_1 and O_2. If both sets have the same cardinal, the iterated closest point algorithm can be used [Besl 1992]. However, in most cases there is no one-to-one correspondence between O_1 and O_2 and one can only assign a probability value to each pair on $O_1 \times O_2$, which yields a fuzzy correspondence table instead of a binary table. The motion function can be estimated together with the fuzzy correspondence in a joint estimation algorithm (see [Chui 2003] for a thin-plate spline model).

    The deformation process we explained in previous section allows the user to dispose of

two important knowledge. First we dispose of the 3-D models V_s of the coronary tree at each phase of the cardia cycle. Moreover, the estimation of the coronary tree at each phase using our deformable allows the construction of time-dependent sequences which describe the displacements of each point of the deformable tree. In other words, we have the following sequences at our disposal:

$$\forall \ell \in \{1, \ldots, L\}, \quad (v_\ell^1, \ldots, v_\ell^S). \tag{4.19}$$

Those sequences provide a one to one correspondence between each point of each coronary 3-D model V_s and each point of V_1, which gives crucial information about the support deformation functions φ_s, $s \in \{2, \ldots, S\}$. The motion deformation functions is estimated according to the following assumption:

$$\forall (s, \ell) \in \{2, \ldots, S\} \times \{1, \ldots, L\}, \quad \varphi_s(v_\ell^s) \simeq v_\ell^1. \tag{4.20}$$

In addition to (4.20), the motion functions φ_s are assumed to belong to a parametric functional space, which in our work are written as follows:

$$\varphi_s : \begin{bmatrix} x \\ y \\ z \end{bmatrix} \longmapsto \begin{bmatrix} x + \sum_{m=1}^{|\mathcal{M}|} \alpha_{X,s}^m b_m(x,y,z) \\ y + \sum_{m=1}^{|\mathcal{M}|} \alpha_{Y,s}^m b_m(x,y,z) \\ z + \sum_{m=1}^{|\mathcal{M}|} \alpha_{Z,s}^m b_m(x,y,z) \end{bmatrix} = \begin{bmatrix} x \\ y \\ z \end{bmatrix} + \Delta_{\alpha_s}(x,y,z), \tag{4.21}$$

where $\mathcal{M}$ is a set of index of a uniform grid on Ω, and each b_m is a cubic B-spline centered on $(x_m, y_m, z_m) \in \mathcal{M}$. The displacement function Δ_{α_s} belongs to a functional space spanned by the b_m's. We defined b_m as in [Jacobson 2006]:

$$\forall m \in \{1, \ldots, |\mathcal{M}|\}, \quad \forall (x,y,z) \in \Omega, \quad b_m(x,y,z) = b(x - x_m)b(y - y_m)b(z - z_m),$$

with

$$\forall t \in \mathbb{R}, \quad b(t) = \begin{cases} |t|^3/2 - t^2 + 2/3 & : \quad |t| \le 1 \\ -(|t| - 2)^3/6 & : \quad 2 \ge |t| > 1 \\ 0 & : \quad |t| > 2 \end{cases} .$$

Let us denote $\alpha_s = \left\{ \left(\alpha_{X,s}^m, \alpha_{Y,s}^m, \alpha_{Z,s}^m \right) \right\}_{m=1}^{|\mathcal{M}|}$ the motion parameters at phase s and let us rename φ_s to φ_{α_s}. The estimation of each α_s has to be carried out following our assumptions on φ_{α_s} (see (4.20) and (4.21)). In addition other criteria on α_s are taken into consideration in order to control the regularity of each φ_{α_s} function. Basically, the estimation of each α_s can be performed by minimizing the functional

$$\psi(\alpha_s) = \sum_{\ell=1}^{L} \|\varphi_{\alpha_s}(v_\ell^s) - v_\ell^1\|^2 + \mu \sum_{m \sim m'} \|\alpha_s^m - \alpha_s^{m'}\|^2 + \nu \|\alpha_s\|^2, \tag{4.22}$$

where μ and ν are positive values, and the second sum is taken over neighboring points in $\mathcal{M}$. Equation (4.22) can be rewritten in a matrix formulation:

$$\psi(\alpha_s) = (\mathbf{B}(V_s)\mathbf{a}_s + \mathbf{v}_s - \mathbf{v}_1)^T(\mathbf{B}(V_s)\mathbf{a}_s + \mathbf{v}_s - \mathbf{v}_1) + \mu\mathbf{a}_s^T\mathbf{C}^T\mathbf{C}\mathbf{a}_s + \nu\mathbf{a}_s^T\mathbf{a}_s, \qquad (4.23)$$

where $\mathbf{a}_s$ (resp. $\mathbf{v}_s$) denotes α_s (resp. V_s) reshaped into a vector, $\mathbf{B}(V_s)$ is a matrix that is expressed in term of $(b_m(v_\ell^s))_{\ell,m}$ and $\mathbf{C}$ is a differential operator. A vector $\mathbf{a}_s$ that minimizes (4.23) must fulfill the following equation:

$$\left(\mathbf{B}(V_s)^T\mathbf{B}(V_s) + \mu\mathbf{C}^T\mathbf{C} + \nu\mathbf{I}\right)\mathbf{a}_s = \mathbf{B}(V_s)^T(\mathbf{v}_1 - \mathbf{v}_s). \qquad (4.24)$$

In practical case, the size of the motion grid $\mathcal{M}$ is small compared to the voxel grid $\mathcal{I}$ whose size is astronomical. For example, if $\mathcal{M}$ is a $8 \times 8 \times 8$ grid, then $\mathbf{B}(V_s)^T\mathbf{B}(V_s) + \mu\mathbf{C}^T\mathbf{C} + \nu\mathbf{I}$ is a 1536×1536 matrix, whose inverse can be computed easily, which leads to

$$\mathbf{a}_s = \left(\mathbf{B}(V_s)^T\mathbf{B}(V_s) + \mu\mathbf{C}^T\mathbf{C} + \nu\mathbf{I}\right)^{-1}\mathbf{B}(V_s)^T(\mathbf{v}_1 - \mathbf{v}_s).$$

If the size of $\mathcal{M}$ is too large, then (4.22) has to be minimized iteratively.

In [Blondel 2004, Blondel 2006], the author uses a 3-D+t B-spline model for the registration. The estimation of its parameters is carried out via the minimization of a cost function that includes a time regularity term. In our work, each motion function φ_s are estimated independently. However they are estimated from the coronary 3-D models V_s that are estimated from one to another according to our deformation model. Therefore, for all $s \in \{2, \ldots, S\}$, V_s is close to V_{s-1} and the time regularity becomes intrinsic.

4.4.5 Tomographic reconstruction

Once each motion function φ_{α_s} is at our disposal, one can compute the support deformation matrix W_s according to (4.9). For better readability, we shall rename $\mathbf{W}_s$ to $\mathbf{W}(\alpha_s)$. Let us recall notations from section 4.4.1. Our aim is is to solve the inverse problem with motion compensation (4.8):

$$\forall s \in \{1, \ldots, S\}, \quad \mathbf{g}_s = \mathbf{P}_{\Theta_s}\mathbf{W}(\alpha_s)\mathbf{f}_1, \qquad (4.25)$$

where $\mathbf{g}_s$ denotes the observed projections at angles $\Theta_s = \{\vartheta_{1,s}, \ldots, \vartheta_{N,s}\}$, $\mathbf{P}_{\Theta_s}$ is the corresponding cone-beam projector, and $\mathbf{f}_1$ is the object function coordinates in the voxel basis $(u_i^n, w_i^n)_{i=1}^n$. Inverse problem (4.25) can be rewritten with matrix concatenation:

$$\mathbf{g} = \mathbf{P}\mathbf{W}(\alpha)\mathbf{f}_1, \qquad (4.26)$$

with

$$\mathbf{PW}(\alpha) = \left[\begin{array}{c} \mathbf{P}_{\Theta_1} \mathbf{W}(\alpha_1) \\ \vdots \\ \mathbf{P}_{\Theta_S} \mathbf{W}(\alpha_S) \end{array} \right].$$

As stated in equation (4.26), the linear inverse problem is more or less equivalent to the static inverse problem (2.10),

$$\mathbf{Pf} = \mathbf{g},$$

using several regularization methods or image prior distribution (see section 2.3.2). For most of them, the approach consists in minimizing the defect

$$\|\mathbf{Pf} - \mathbf{g}\|^2 + \gamma \mathrm{p}(\mathbf{f})$$

where $\mathrm{p}(\mathbf{f})$ is a term that comes from a regularization of the generalized inverse of $\mathbf{P}$ or is a log-likelihood of an image *a priori* distribution. More generally, p can be interpreted as a penalty term, that is designed to enhance properties on $\mathbf{f}$. In (4.26), we are dealing with the object coordinates $\mathbf{f}_1$ in a voxel basis. As $\mathbf{f}_1$ can be interpreted as a sampled version of the object function at phase $s = 1$, similar penalty term can be considered. In this section, we admit that

$$\forall i \in \{1, \dots, n\}, \quad (\mathbf{f}_1)_i = u_i^n(f_1) \geq 0,$$

which means the image has only positive values. Our reconstruction method is then based on

$$\text{minimize} \quad \Psi(\mathbf{f}_1) = \|\mathbf{PW}(\alpha)\mathbf{f}_1 - \mathbf{g}\|^2 + \gamma \mathrm{p}(\mathbf{f}_1) \tag{4.27}$$

$$\text{with} \quad \forall i \in \{1, \dots, n\}, \quad (\mathbf{f}_1)_i \geq 0.$$

Moreover, we consider that a voxel value $(\mathbf{f}_1)_i$ is null if it is located in an empty area (in the background) and positive if it is located on an object.

In this manuscript, we introduced a new penalty term, which is based on the 3-D reconstructed centrelines as phase $s = 1$. As the 3-D models sequences $(V_s)_{s \in S}$ is a useful tool for the motion estimation, the 3-D model V_s gives also crucial information about the object at phase $s = 1$. In section 4.2.1 we mentioned that the support of the object function f_1 coincides with the coronary arteries. As a consequence, it is reasonable to admit that $\mathbf{f}_1 = (u_1(f_1), \dots, u_n(f_1))^T$ is null outside of a neighborhood of V_1. Our penalty term is then design to penalize high u_i^n values that are located far from V_1, and is calculated as follows:

$$\mathrm{p}_{\text{vessels}}(\mathbf{f}_1) = \sum_{i=1}^{n} \Delta_i(V_1)(\mathbf{f}_1)_i^{\beta},$$

where $\Delta_i(V_1)$ is a square distance between voxel i and the 3-D centrelines V_1 and $\beta > 0$. If i is located far from the centrelines, the $\Delta_i(V_1)$ value is large and a minimizer of (4.28) is more likely to have a small $(\mathbf{f}_1)_i$ value. On the contrary, if voxel i is located near of the centrelines, the $\Delta_i(V_1)$ value is small and a high $(\mathbf{f}_1)_i$ value is not penalized. The β value has also its influence on the reconstruction: for example, $\beta = 2$ encourage smooth variation on $\mathbf{f}_1$ as $\beta = 1$ allows regular shapes on $\mathbf{f}_1$'s support. In our work, we chose

$$\Delta_i(V) = \min_{\ell=1,\ldots,L} \{d^2((x_i, y_i, z_i), v_\ell)\},$$

where (x_i, y_i, z_i) are the coordinates of the i-voxel in $\mathbb{R}^3$. Let us denote

$$\Delta(V) = (\Delta_1(V), \ldots, \Delta_n(V))^T.$$

The cost function $\Psi(\mathbf{f}_1)$ can be rewritten in a matrix formulation:

$$\Psi(\mathbf{f}_1) = (\mathbf{f}_1 \mathbf{PW}(\alpha) - \mathbf{g})^T (\mathbf{PW}(\alpha)\mathbf{f}_1 - \mathbf{g}) + \gamma \Delta(V_1)^T \mathbf{f}_1^\beta, \qquad (4.28)$$

where $\mathbf{f}_1^\beta = \left((\mathbf{f}_1)_1^\beta, \ldots, (\mathbf{f}_1)_n^\beta\right)^T$. Its gradient is equal to

$$\nabla\Psi(\mathbf{f}_1) = 2\mathbf{PW}(\alpha)^T (\mathbf{PW}(\alpha)\mathbf{f}_1 - \mathbf{g}) + \beta\gamma\Delta(V_1) * \mathbf{f}_1^{\beta-1}, \qquad (4.29)$$

where the symbol $*$ denotes the component by component vector product.

4.5 Results on simulated data

4.5.1 Data simulation

In our case we are interested in assessing the performance that can be obtained in an ideal case through simulated data with assumptions similar to those used in [Ruan 1994, Blondel 2006]. We assumed that:

- We have a 3-D model of the coronary at phase $s = 1$ of the cardiac cycle at our disposal.

- We own 80 cone-beam projections uniformly distributed from $0°$ to $120°$ (one projection every $1.5°$).

- The time dependant volume image $\mathbf{f}_t$ is periodical.

- $\mathbf{f}_t$ can be renamed $\mathbf{f}_s$, the volume at phase s of the cardiac cycle.

- The number of cardiac cycles during the acquisition process is equal to 4.

- Each volume $\mathbf{f}_s$ is projected N times at angles $\Theta_s = \{\vartheta_{1,s}, \ldots, \vartheta_{N,s}\}$.

- The projections are gated according to the ECG.

- The 2-D vessel centrelines have been extracted on each of the 2-D projections.

- The background has been removed on each projections.

As the number of cycle is equal to 4 and the number of projections is equal to 80, the number of phases S is equal to $80/4 = 20$. Each volume $\mathbf{f}_s$ is projected 4 times at angles $\Theta_s = \{\vartheta_{1,s}, \vartheta_{2,s}, \vartheta_{3,s}, \vartheta_{4,s}\}$, and each angle is defined by

$$\forall (n, s) \in \{1, 2, 3, 4\} \times \{1, \ldots, S\}, \quad \vartheta_{n,s} = (s - 1)\Delta\vartheta + (n - 1)\frac{120}{N} = 3(s - 1)/2 + 30(n - 1).$$

For example, phase $s = 1$ is projected at angles $\Theta_1 = \{0°, 30°, 60°, 90°\}$, phase $s = 2$ at $\Theta_2 = \{1.5°, 31.5°, 61.5°, 91.5°\}$ and so on. We simulated 3-D volumes of two coronary trees at 20 different cardiac phases, using 3-D centrelines $V_1, \ldots, V_{20}$ that had been previously extracted from a 3-D dynamic sequence acquired on a 64-slice GE LightSpeed CT coronary angiography [Yang 2006]. This sequence included 20 volumes reconstructed at every 5% of the RR interval. The reconstructed volumes correspond to the left and right coronary trees(see figure 4.1). Each 3-D model V_s of the left (resp. right) coronary tree has the same vessel structure $\mathcal{V}_{\text{left}}$ (resp. $\mathcal{V}_{\text{right}}$), which consists of 6 branches and 99 points (resp. 2 branches and 57 points). We worked independently on each coronary tree.

The simulated dynamic volume is a sequence of binary functions $\mathbf{f}_s : \mathcal{I} \to \{0, 1\}$, such that $(\mathbf{f}_s)_j = 1$ if the j-th voxel is located in a tube centered on the 3-D centrelines V_s and $(\mathbf{f}_s)_j = 0$ in the opposite case (see figure 4.2 and 4.3). For memory reasons, we limited our work to $192 \times 192 \times 192$ uniform grid and the vessel radius is equal to one voxel. Thus, as each volume $\mathbf{f}_s$ has null outside of the vessels, there is no need for a background removal operation on the 2-D projections.

We used the extracted 3-D V_1 as our reference tree at phase $s = 1$. To simulate the 2-D centerlines, we performed geometric projections of the 3-D models $V_2, \ldots, V_{20}$ using the projector $\mathcal{P}_{\vartheta_{n,s}}^{\text{geom}}$ defined in (4.4) (see figure 4.4 and figure 4.5). Thus, 2-D centerlines do not have to be extracted from the projections.
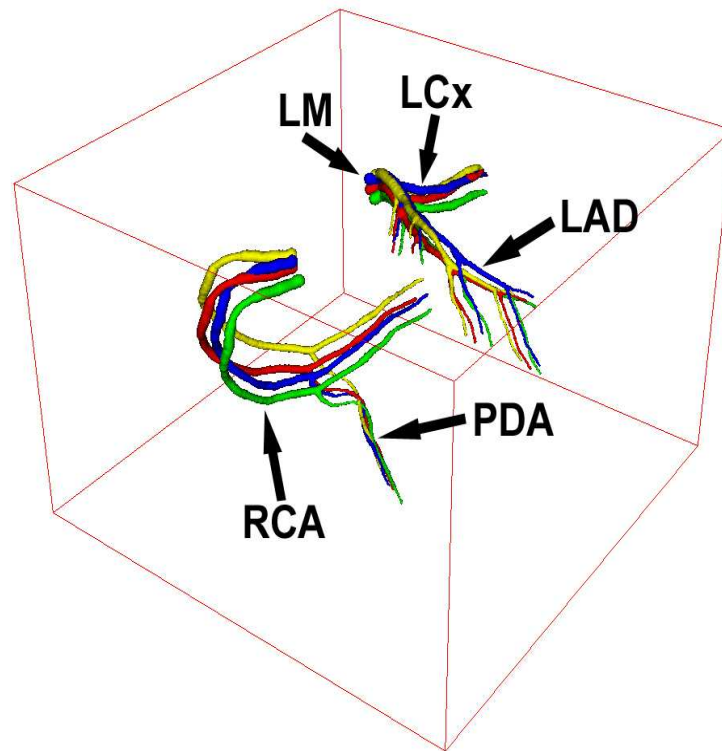
Figure 4.1: Extracted 3-D volumes at different phases of the RR interval. Each color corresponds to a different phase: yellow: 0%, red: 20%, green: 40%, blue: 80%.
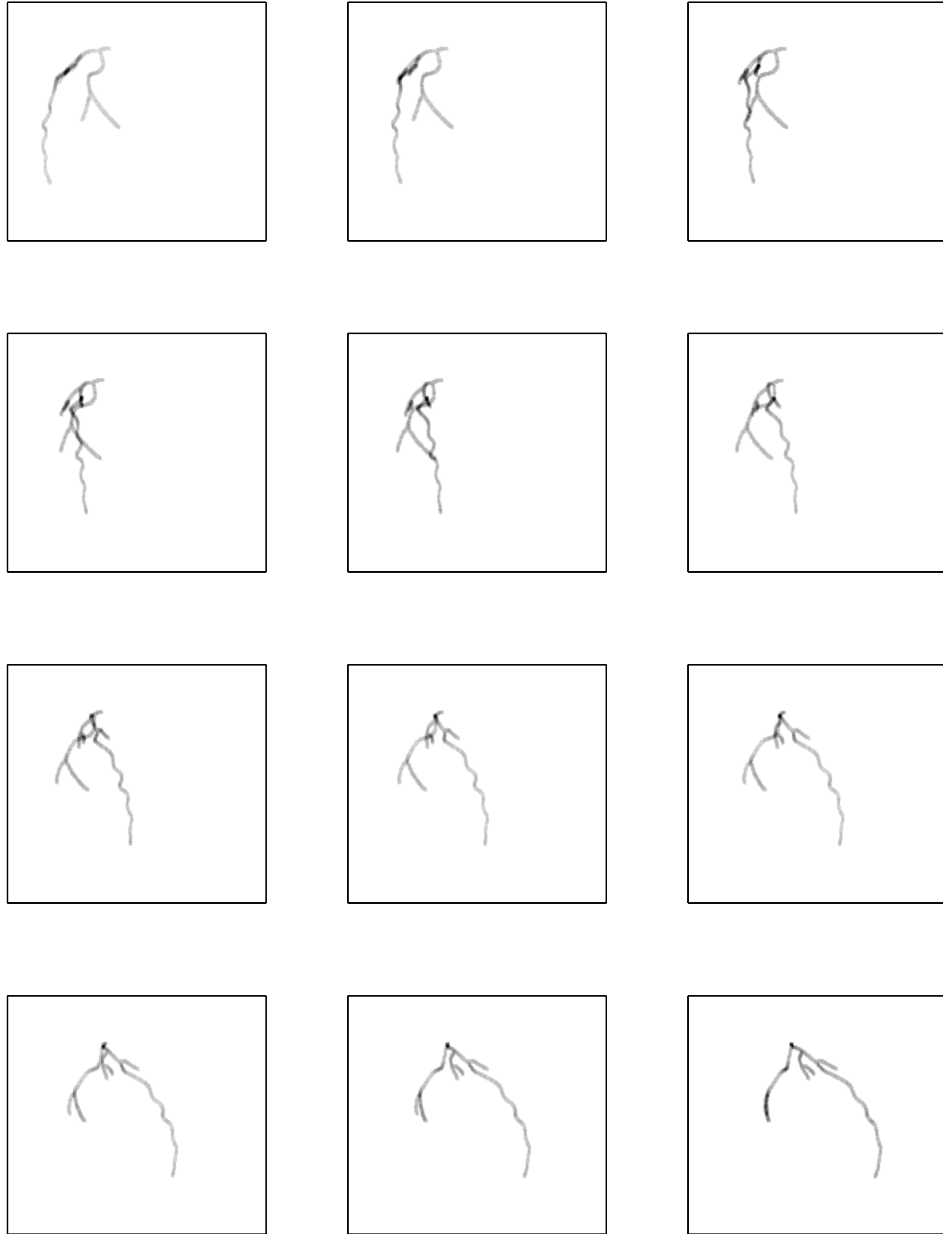
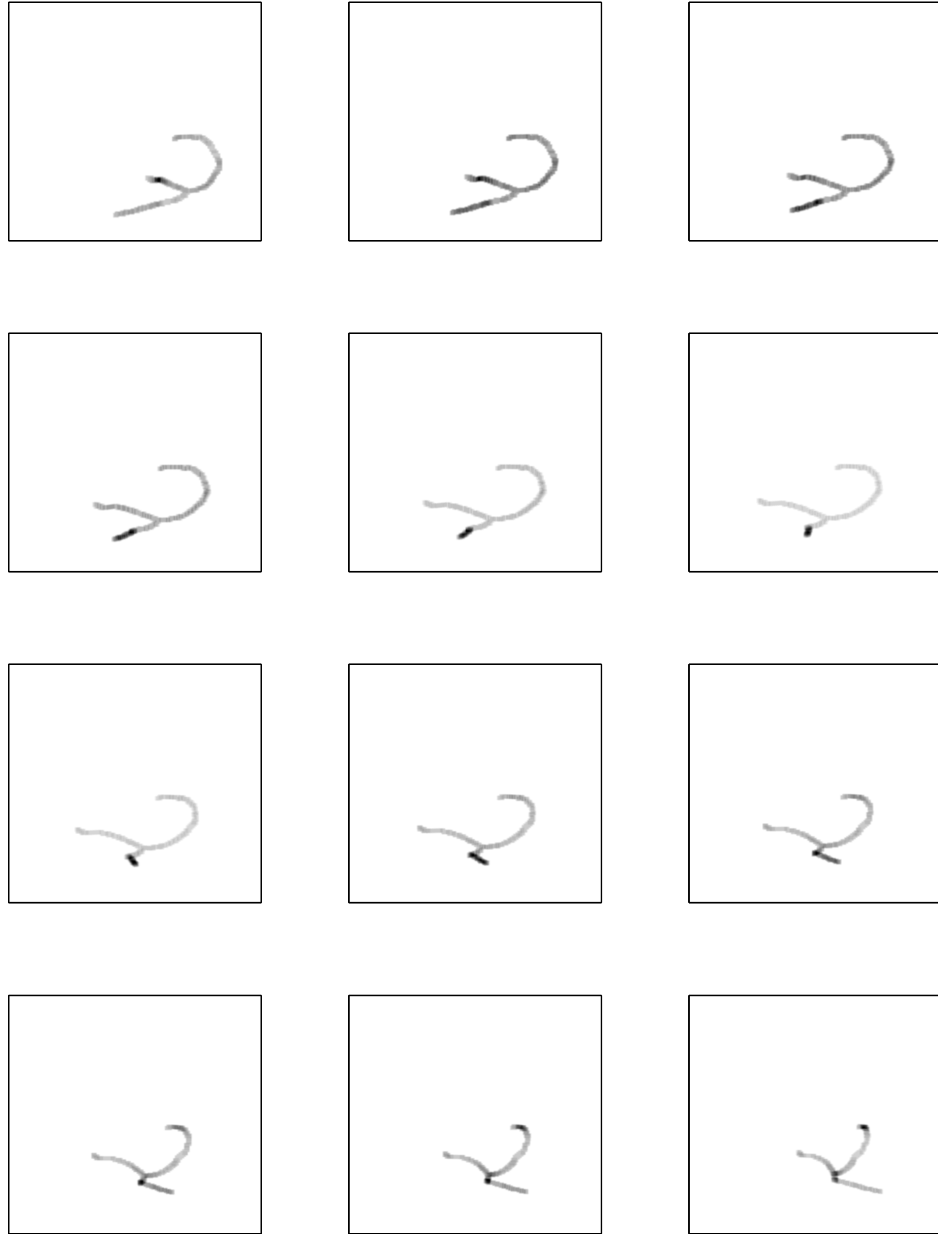Figure 4.2: 12 projections of the left coronary tree simulated binary volume at phase $s = 1$, from 10° to 120°.

Figure 4.3: 12 projections of the right coronary tree simulated binary volume at phase $s = 1$, from $10°$ to $120°$.
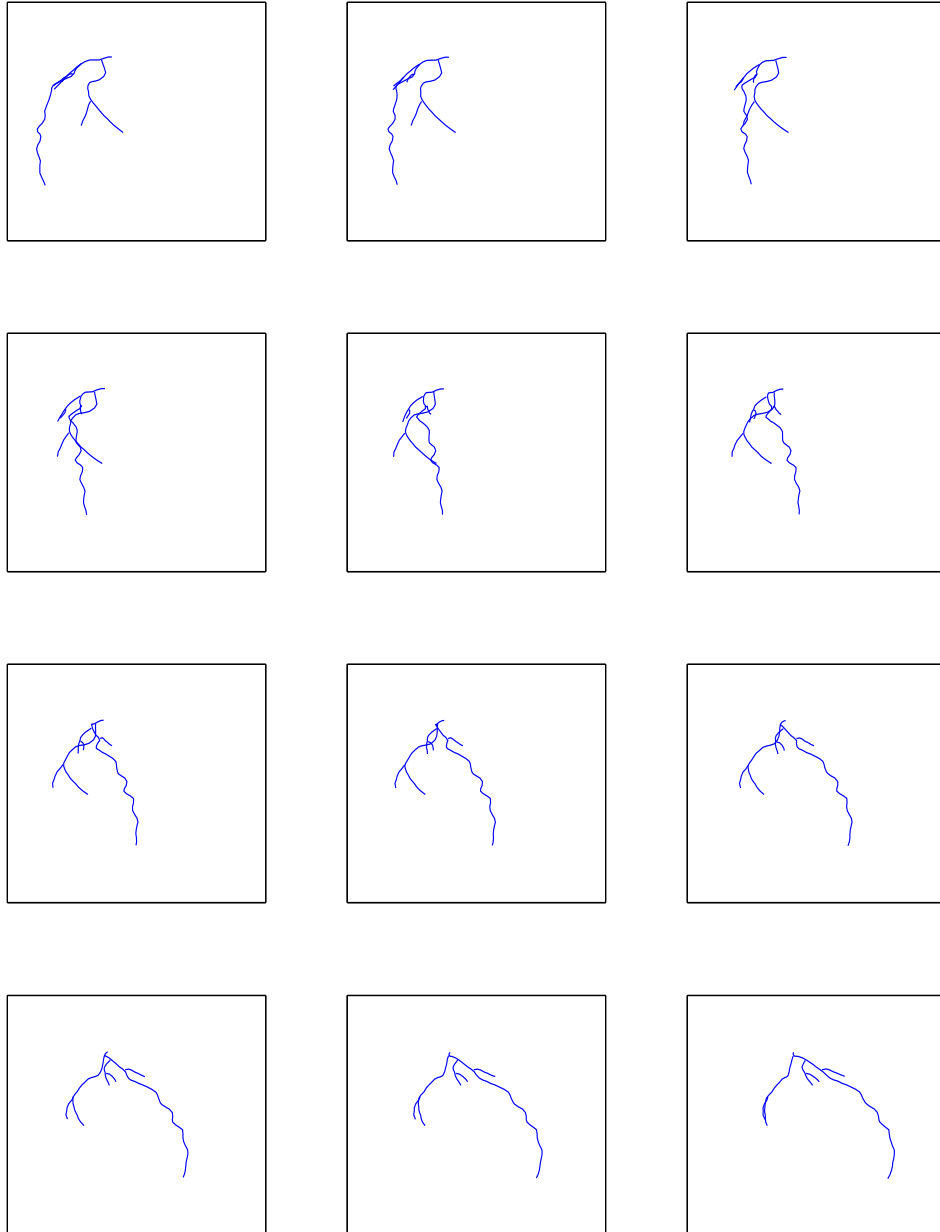
Figure 4.4: 12 extracted centrelines of the projected left coronary tree simulated binary volume at phase $s = 1$, the projections being taken from $10°$ to $120°$.
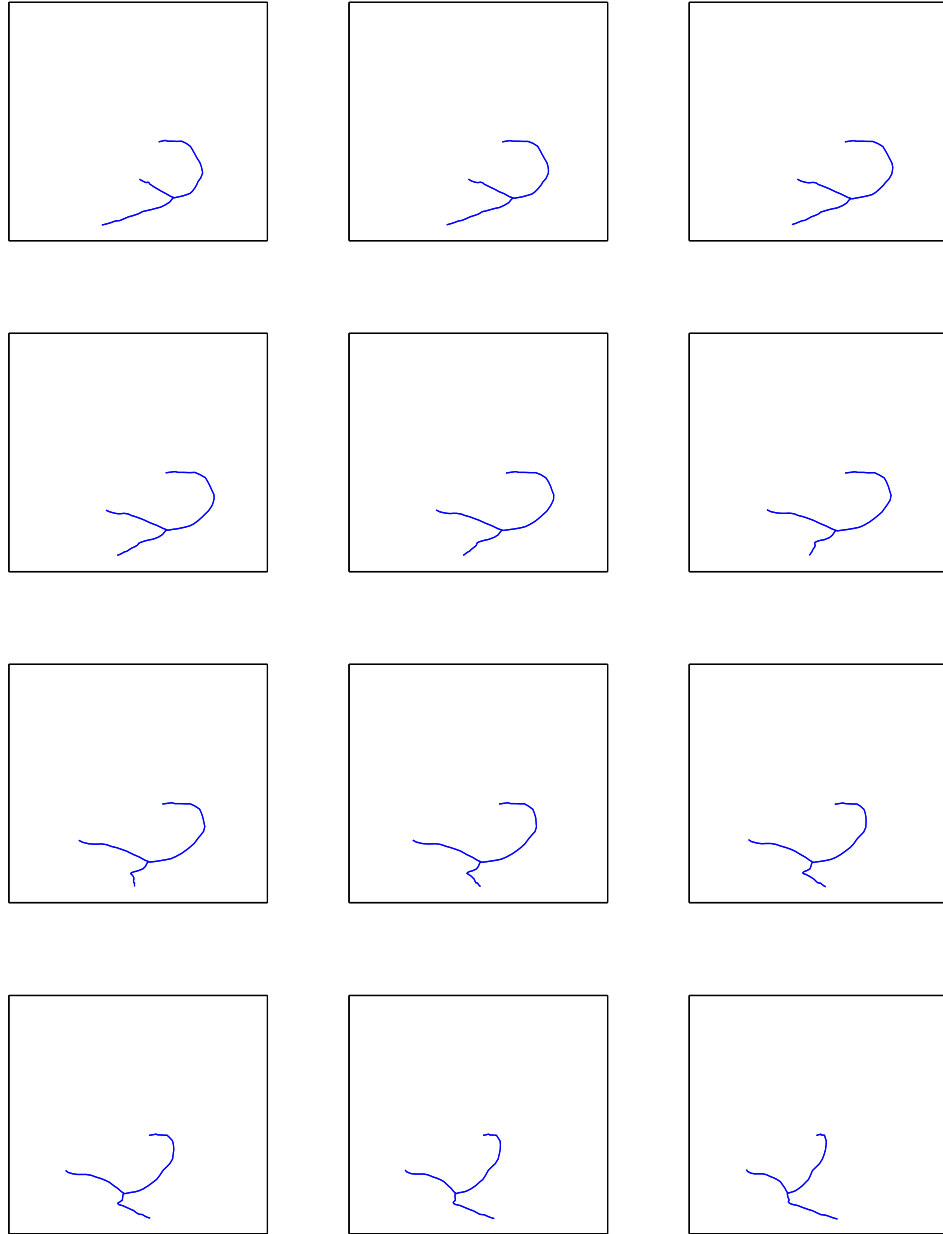
Figure 4.5: 12 extracted centrelines of the projected right coronary tree simulated binary volume at phase $s = 1$, the projections being taken from $10°$ to $120°$.
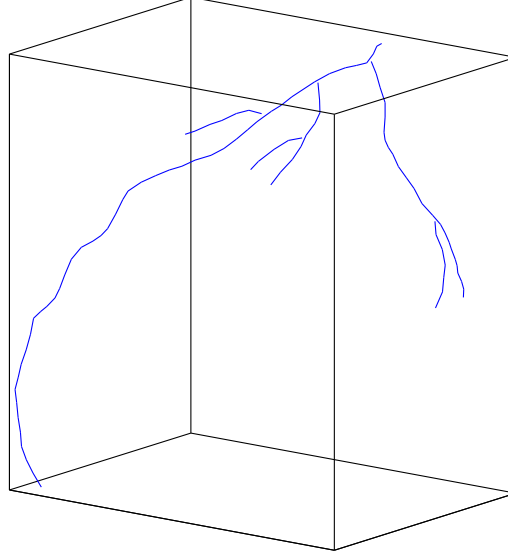
Figure 4.6: Original 3-D model of the left coronary tree at phase $s = 1$. This 3-D model was used as the starting tree V_1 in our deformation process.

4.5.2 Centrelines reconstruction

We here present the results of the deformation algorithm presented in section 4.4. We used the extracted centrelines at phase $s = 1$ to represent the starting 3-D model V_1 (see section 4.5.1 and figure 4.6.). The deformable model algorithm shall start from this 3-D skeleton. Its topological structure is defined according to its 6 branches (see section 4.4.3). We used the vessel labeling on projections as well as (4.13) for the 2-D distance on extracted vessels.

Several aspects of the algorithm must be considered:

- The number of terms $n_{\min}$ in the sum which defines the 2-D distance function D_ϑ (see (4.12)) must be set up correctly. A too large $n_{\min}$ values would force the distance function $D_\vartheta(h)$ to consider to many 2-D vessel point in the neighborhood of h. In that situation, w may converge to an "average target" which might not belong to a 2-D centreline. On the contrary, if $n_{\min}$ is too small, w may converge to a wrong target. In this work, we chose $n_{\min} = 4$. This value shows the best results.
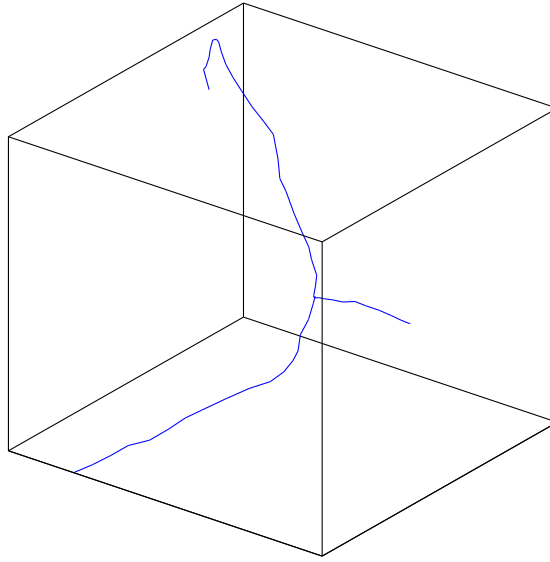
Figure 4.7: Original 3-D model of the right coronary tree at phase $s = 1$. This 3-D model was used as the starting tree V_1 in our deformation process.

- The choice the the smoothness control function $\mathbf{F}_i$, $i = 1, 2, 3$ is of a major importance. The 3 proposed functions (see section 4.4.3.2) have been tested.

- For each $\mathbf{F}_i$, the κ value must be chosen carefully, in order to obtain a good tradeoff between vessels smoothness and data fidelity.

- The λ value determines the displacement speed of each 3-D point of the 3-D deformable model. In this work, we fixed $\lambda = 0.1$.

In order to evaluate the performance of each deformation method, we must define a suitable score function. Let us say that we wish to estimate the 3-D model V_s, starting from the initial 3-D model V_1. Note that in our algorithm, V_s is estimated with the deformation algorithm starting from V_{s-1}. However, its robustness can be better evaluated if the deformation is performed between non-consecutive phases. Let V be any 3-D coronary model. We defined the score of $V = \{v_1, \ldots, v_L\}$ with respect to phase s as the mean distance of each point v_ℓ to its target v_ℓ^s:

$$\varepsilon_s(V) = \frac{1}{L} \sum_{\ell=1}^{L} \|v_\ell - v_\ell^s\|. \tag{4.30}$$

We tested the three smoothness cost functions $\mathbf{F}_1$, $\mathbf{F}_2$ and $\mathbf{F}_3$ for different values of κ. Our tests were performed for deformations of the starting tree V_1 to V_5 with 20 iterations. We also added gaussian centered noise with a standard deviation σ to the 2-D centrelines coordinates in each direction on each projections, to simulate (roughly) the effects of gating errors and centrelines extractions inaccuracies. Results are displayed in table 4.1 and table 4.2 for the regularization cost functions $\mathbf{F}_1$ and $\mathbf{F}_3$, and in tables 4.3 and 4.4 for $\mathbf{F}_2$. Visualizations of the deformation process are displayed in figure 4.8 and figure 4.9. The centrelines are included in a cube whose sides length are equal to 180mm.

In each of these table the symbol ∞ means that the algorithm has diverged. This phenomenon occurs when the κ value is too large. So far it appears that $\mathbf{F}_3$ with $\kappa = 3$ gave the best results. Nevertheless, one should perform more test to assess the performances of this method for linear combinations of the $\mathbf{F}_i$ and see if any complementary effect occurs.

4.5.3 Motion estimation

Once the sequence of coronary 3-D centrelines $V_1, \ldots, V_{20}$ has been recovered, the sequence of parameters $(\alpha_s)_{s=1}^{S}$ is estimated by minimizing the quadratic cost function (4.22). The process
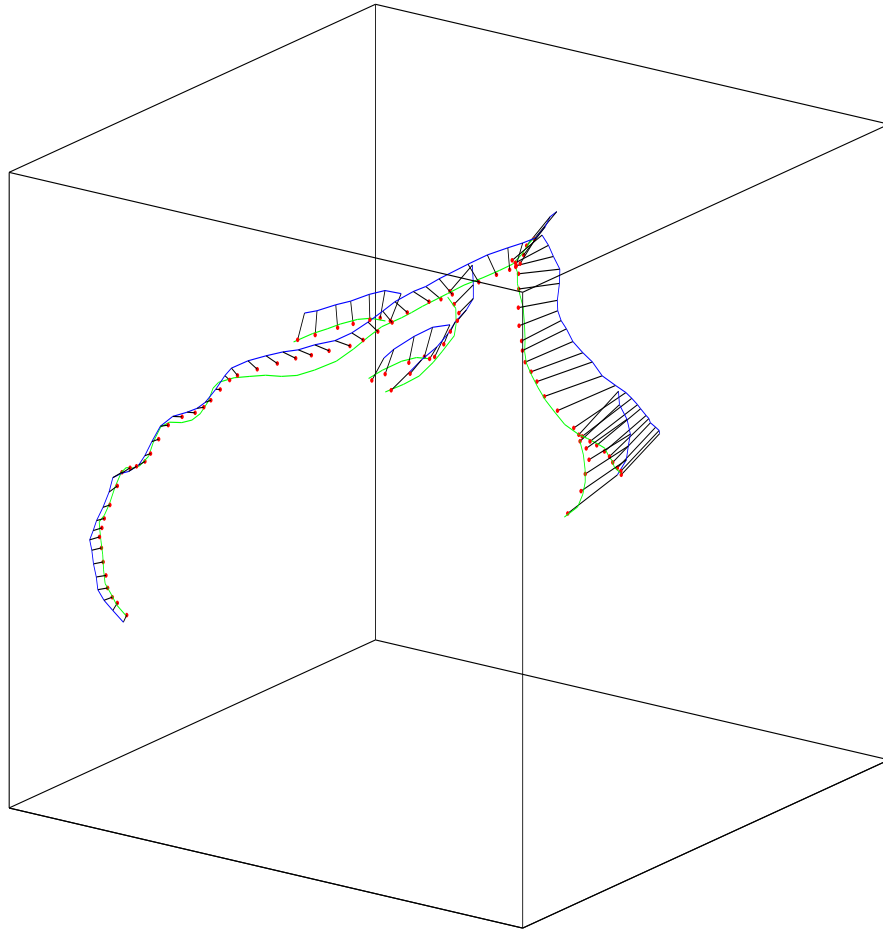
Figure 4.8: Result of the deformation process between V_1 (in blue) and V_5 (in green), for the left coronary tree. The red points represent the deformed 3-D model V_1.
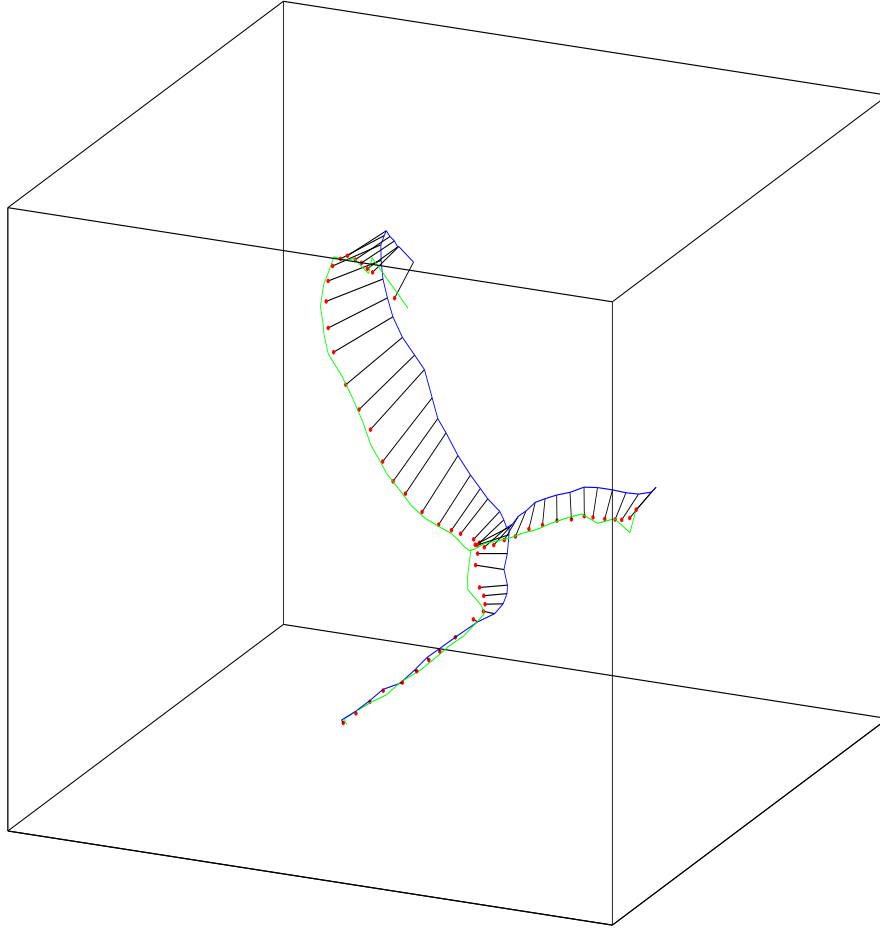
Figure 4.9: Result of the deformation process between V_1 (in blue) and V_5 (in green), for the right coronary tree. The red points represent the deformed 3-D model V_1.

Table 4.1: Values of ε_5 using $\mathbf{F}_1$ and $\mathbf{F}_3$, for the left coronary tree (in mm) for different values of κ.

$\star$		$\kappa = 0.1$	$\kappa = 1$	$\kappa = 2$	$\kappa = 3$	$\kappa = 4$	$\kappa = 5$	$\kappa = 6$	$\kappa = 7$
$\sigma = 0$	$\mathbf{F}_1$	1.57	1.45	1.43	1.40	1.43	1.51	∞	∞
	$\mathbf{F}_3$	1.60	1.38	1.19	1.00	1.10	1.15	∞	∞
$\sigma = 3$	$\mathbf{F}_1$	1.67	1.47	1.47	1.45	1.47	1.59	∞	∞
	$\mathbf{F}_3$	1.75	1.41	1.25	1.06	1.17	1.24	∞	∞
$\sigma = 6$	$\mathbf{F}_1$	1.73	1.62	1.55	1.54	1.57	1.65	∞	∞
	$\mathbf{F}_3$	1.87	1.54	1.34	1.18	1.21	1.26	∞	∞

Table 4.2: Values of ε_5 using $\mathbf{F}_1$ and $\mathbf{F}_3$, for the right coronary tree (in mm) for different values of κ.

$\star$		$\kappa = 0.1$	$\kappa = 1$	$\kappa = 2$	$\kappa = 3$	$\kappa = 4$	$\kappa = 5$	$\kappa = 6$	$\kappa = 7$
$\sigma = 0$	$\mathbf{F}_1$	2.19	2.12	2.12	1.96	2.04	2.12	∞	∞
	$\mathbf{F}_3$	2.19	2.04	1.79	1.70	1.79	1.96	∞	∞
$\sigma = 3$	$\mathbf{F}_1$	2.26	2.19	2.12	2.04	2.04	2.12	∞	∞
	$\mathbf{F}_3$	2.26	2.04	1.96	1.87	1.87	1.96	∞	∞
$\sigma = 6$	$\mathbf{F}_1$	2.65	2.26	2.26	2.04	2.04	2.12	∞	∞
	$\mathbf{F}_3$	2.26	2.12	1.96	1.96	1.96	2.04	∞	∞

Table 4.3: Values of ε_5 using $\mathbf{F}_2$ for the left coronary tree (in mm) for different values of κ.

$\star$	$\kappa = 0.01$	$\kappa = 0.15$	$\kappa = 0.2$	$\kappa = 0.25$	$\kappa = 0.3$	$\kappa = 0.35$
$\sigma = 0$	1.60	1.35	1.33	1.34	∞	∞
$\sigma = 3$	1.62	1.32	1.31	1.40	∞	∞
$\sigma = 6$	1.69	1.54	1.50	1.56	∞	∞

is dependent on the choice of the pair of parameters (μ, ν). In order to find the optimal pair, the initial centreline V_1 must be compared to each transformation of V_s by, the mapping φ_{α_s}, *i.e.* by evaluating the defect

$$\varepsilon_1(\varphi_{\alpha_s}(V_s)) = \frac{1}{L} \sum_{\ell=1}^{L} \|\varphi_{\alpha_s}(v_\ell^s) - v_\ell^1\|.$$

Table 4.4: Values of ε_5 using $\mathbf{F}_2$ for the right coronary tree (in mm) for different values of κ.

$\star$	$\kappa = 0.01$	$\kappa = 0.15$	$\kappa = 0.2$	$\kappa = 0.25$	$\kappa = 0.3$	$\kappa = 0.35$
$\sigma = 0$	2.26	2.19	2.12	2.12	2.12	2.12
$\sigma = 3$	2.26	2.19	2.19	2.12	2.12	2.12
$\sigma = 6$	2.33	2.26	2.19	2.19	2.19	2.19

Table 4.5: $\varepsilon_1(\varphi_{\alpha_s}(V_s))$ values (in mm) for s in $\{2, \ldots, 10\}$, for the left coronary tree.

s	2	3	4	5	6	7	8	9	10
$\varepsilon_1(\varphi_{\alpha_s}(V_s))$	0.80	0.96	1.36	1.47	1.50	1.62	1.72	1.76	1.78

for different values of s. This defect evaluates the square difference between V_1 and the transformation of V_s with φ_{α_s}. So far the best values we obtains were for $\mu = 0.001$ and $\nu = 0.1$. We shall use these values for the rest of this work. Note that these optimal parameters are strongly data-dependant and may be different from one data set to another. The results of the transformations with these parameter values are displayed in table 4.5 and table 4.6, as well as in figure 4.10 and figure 4.11.

We can notice that as phase s is close to end of systole (50% of the RR interval), the difference between V_1 and V_s becomes larger and the mapping φ_{α_s} becomes less accurate, especially for the right coronary tree which is affected by a strong motion.

4.5.4 Tomographic reconstruction

4.5.4.1 Motion Computation

The computation of the motion matrix $\mathbf{W}(\alpha_s)$ is a major issue and requires investigations. It directly depends on the voxel basis (u_i, w_i) and on the motion model φ_{α_s}. In this work, we

Table 4.6: $\varepsilon_1(\varphi_{\alpha_s}(V_s))$ values (in mm) for s in $\{2, \ldots, 10\}$, for the right coronary tree.

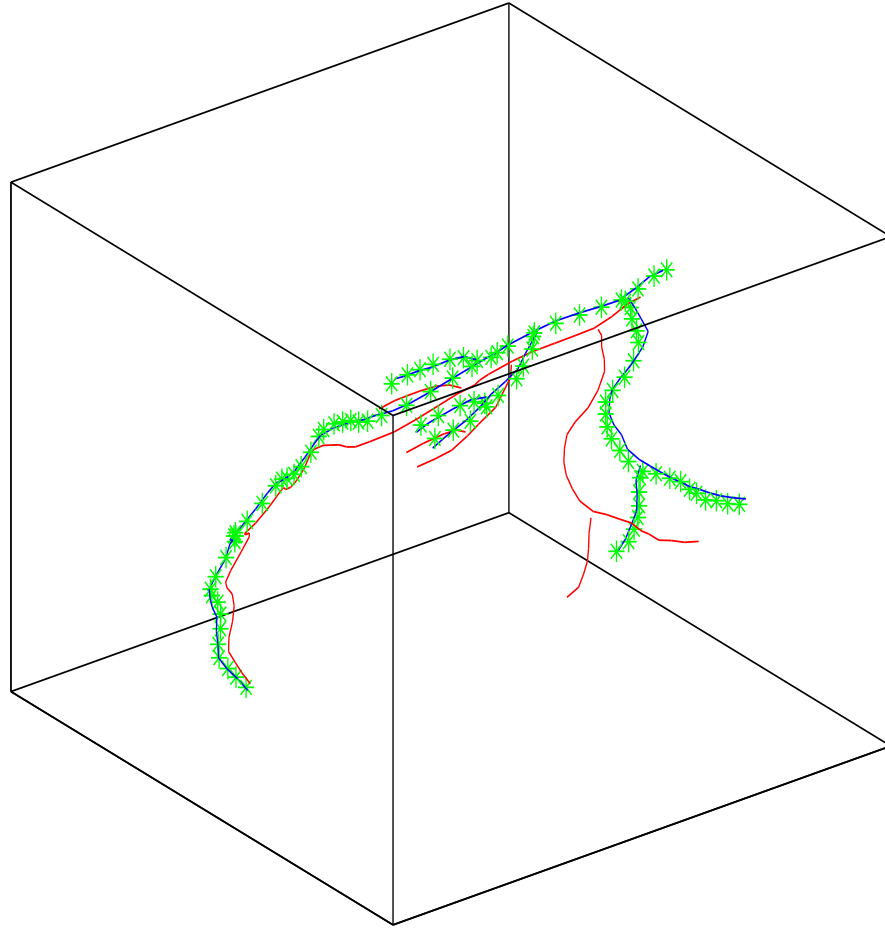| s	2	3	4	5	6	7	8	9	10
$\varepsilon_1(\varphi_{\alpha_s}(V_s))$	0.95	1.01	1.07	1.84	2.60	2.60	2.59	2.70	2.93

Figure 4.10: Transformation of V_6 (left coronary tree) with φ_{α_6}. The blue (resp. red) centreline corresponds to V_1 (resp. V_6). The green dots correspond to the transformation of V_6 with φ_{α_6}
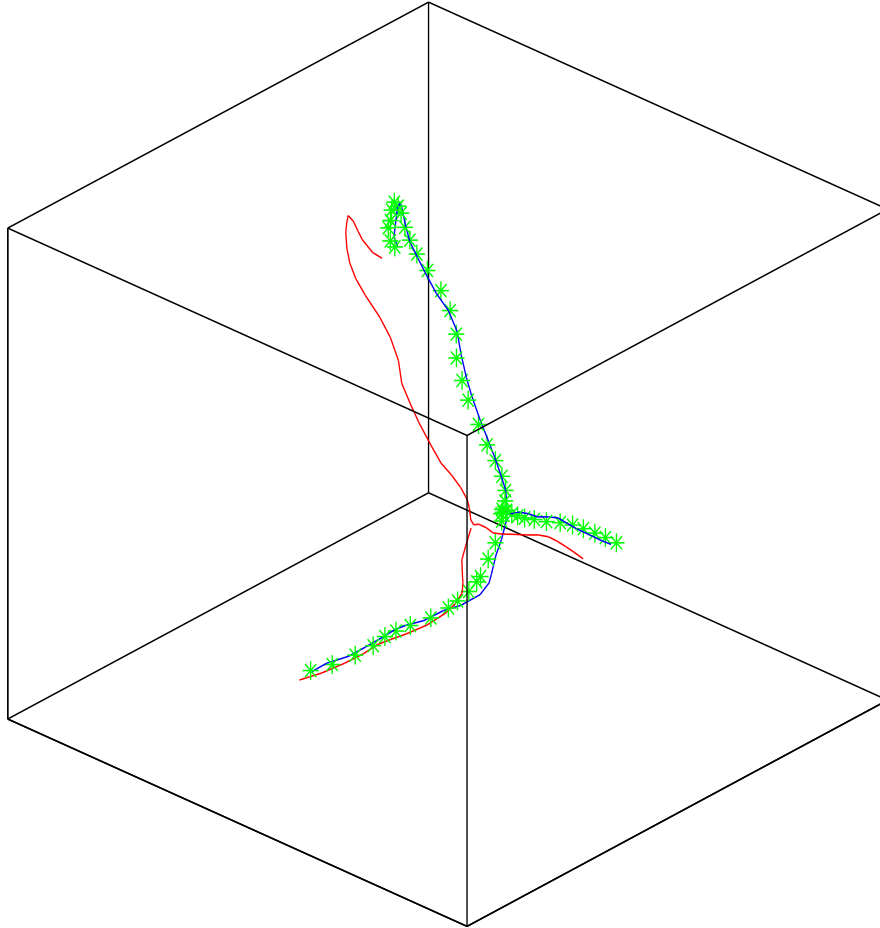
Figure 4.11: Transformation of V_6 (right coronary tree) with φ_{α_6}. The blue (resp. red) centreline corresponds to V_1 (resp. V_6). The green dots correspond to the transformation of V_6 with φ_{α_6}

used the voxel basis given in example 6, that is to say

$$\forall i \in \mathcal{I}, \quad w_i^n(x) = \begin{cases} 1 & \text{if } x \in \aleph_i^n \\ 0 & \text{otherwise} \end{cases}$$

and

$$u_i^n(f) = \frac{1}{\text{vol}(\aleph_i^n)} \int_{\aleph_i^n} f(x) \mathrm{d}\lambda(x).$$

The motion matrix $\mathbf{W}(\alpha_s)$ is therefore defined by

$$\forall (i,j) \in \{1, \ldots, n\}^2, \quad \mathbf{W}(\alpha_s)_{j,i} = \frac{1}{\text{vol}(\aleph_j)} \int_{\aleph_j} \mathbb{1}_{\aleph_i}(\varphi_{\alpha_s}(x)) \mathrm{d}\lambda(x). \tag{4.31}$$

We can see that the calculation of the integral in (4.31) directly involves the set $\varphi_{\alpha_s}^{-1}(\aleph_i)$. Since the B-spline model we chose for φ_{α_s} is not invertible, it cannot be calculated analytically. However, it can be approximated as follows: let $x_{j,1}, \ldots, x_{j,6}$ be the six centers of the six edges of voxel cube $\aleph_j$. Then we have

$$\mathbf{W}(\alpha_s)_{j,i} = \frac{1}{\text{vol}(\aleph_j)} \int_{\aleph_j} \mathbb{1}_{\aleph_i}(\varphi_{\alpha_s}(x)) \mathrm{d}\lambda(x) \simeq \frac{1}{6} \sum_{k=1}^{6} \mathbb{1}_{\aleph_i}(\varphi_{\alpha_s}(x_{j,k})).$$

Once the parameters α_s are estimated, the $\varphi_{\alpha_s}(x_{j,k})$ values can be pre-computed and the matrix calculation $\mathbf{W}(\alpha_s)\mathbf{u}$ can be efficiently performed.

4.5.4.2 Reconstruction error

Let $\mathbf{f}_1^*, \ldots, \mathbf{f}_{20}^*$ be the real volumes at phase $s = 1, \ldots, 20$ that we wish to estimate. We shall recall notations from section 4.2.2, section 4.4 and section 4.4.5 which are

$$\mathbf{P} = \begin{bmatrix} \mathbf{P}_{\Theta_1} \\ \vdots \\ \mathbf{P}_{\Theta_{20}} \end{bmatrix}, \quad \mathbf{PW}(\alpha) = \begin{bmatrix} \mathbf{P}_{\Theta_1}\mathbf{W}(\alpha_1) = \mathbf{P}_{\Theta_1} \\ \vdots \\ \mathbf{P}_{\Theta_{20}}\mathbf{W}(\alpha_{20}) \end{bmatrix}.$$

Let us denote $\mathbf{g}_{\text{dyn}}$ the set of projections affected by the motion:

$$\mathbf{g}_{\text{dyn}} = \begin{bmatrix} \mathbf{g}_1 \\ \vdots \\ \mathbf{g}_{20} \end{bmatrix} = \begin{bmatrix} \mathbf{P}_{\Theta_1}\mathbf{f}_1^* \\ \vdots \\ \mathbf{P}_{\Theta_{20}}\mathbf{f}_{20}^* \end{bmatrix}$$

is the vector of the 80 projections performed as the object is affected by motion. Let $\mathbf{f}_1$ be an estimation of $\mathbf{f}_1^*$. We shall use the following reconstruction error function:

$$\epsilon(\mathbf{f}_1, \mathbf{f}_1^*) = \frac{\|\mathbf{f}_1 - \mathbf{f}_1^*\|}{\|\mathbf{f}_1^*\|}.$$

Note that this error cost function may take high values for volume whose support is small, **as it is the case here for vessels**. Let

$$\mathbf{g}_{\text{static}} = \mathbf{P}\mathbf{f}_1^*$$

be the 80 projections of the initial volume $\mathbf{f}_1^*$ (not affected by any motion). As references scores, we performed several reconstruction using a MAP method, with the following image prior distribution on $\mathbf{f}_1$ (see sections 1.3.3 and 2.3.2.4 for details):

$$\mathbf{p}_\beta(\mathbf{f}_1) = \sum_{i \sim j} |(\mathbf{f}_1)_i - (\mathbf{f}_1)_j|^\beta,$$

with $\beta = 1$. Let $c \in \{l, r\}$ be the left/right index: $c = l$ (resp. $c = r$) for the left (resp. right) coronary tree, and $j \in \{1, 2\}$ be the method index: $j = 1$ (resp. $j = 2$) for the MAP reconstruction (resp. for the reconstruction with our vessel prior).

1. A first score is calculated by performing a static reconstruction of the object $\mathbf{f}_1$, by solving inverse problem

$$\mathbf{g}_{\text{static}} = \mathbf{P}\mathbf{f}_1$$

   using an MAP reconstruction method with the image prior we mentioned above:

$$\text{minimize} \quad \Psi_{\text{static},1}(\mathbf{f}_1) = \|\mathbf{P}\mathbf{f}_1 - \mathbf{g}_{\text{static}}\|^2 + \gamma \mathbf{p}_\beta(\mathbf{f}_1)$$
$$\text{with} \quad \forall i \in \{1, \dots, n\}, \quad (\mathbf{f}_1)_i \geq 0.$$

   The obtained score is denoted $\mathfrak{R}_{\text{static}}(c, 1)$.

2. A second score is calculated by performed by solving the same inverse problem

$$\mathbf{g}_{\text{static}} = \mathbf{P}\mathbf{f}_1$$

   by minimizing our cost function that includes our vessel prior:

$$\text{minimize} \quad \Psi_{\text{static},2}(\mathbf{f}_1) = \|\mathbf{P}\mathbf{f}_1 - \mathbf{g}_{\text{static}}\|^2 + \gamma \mathbf{p}_{\text{vessels}}(\mathbf{f}_1)$$
$$\text{with} \quad \forall i \in \{1, \dots, n\}, \quad (\mathbf{f}_1)_i \geq 0,$$

   in order to evaluate the performances of our vessel prior. The obtained score is denoted $\mathfrak{R}_{\text{static}}(c, 2)$.

3. A third reference score is calculated by solving the dynamic tomographic inverse problem

$$\mathbf{g}_{\text{dyn}} = \mathbf{P}\mathbf{f}_1$$

by performing the optimization problem

$$\text{minimize} \quad \Psi_{\text{dyn,1}}(\mathbf{f}_1) = \|\mathbf{P}\mathbf{f}_1 - \mathbf{g}_{\text{dyn}}\|^2 + \gamma \mathrm{p}_\beta(\mathbf{f}_1)$$
$$\text{with} \quad \forall i \in \{1, \dots, n\}, \quad (\mathbf{f}_1)_i \geq 0,$$

which is a MAP reconstruction using the dynamic data with no motion compensation. The obtained score is denoted $\mathfrak{R}_{\text{dyn}}(c, 1)$.

4. A fourth reference score is calculated by solving the dynamic tomographic inverse problem

$$\mathbf{g}_{\text{dyn}} = \mathbf{P}\mathbf{f}_1$$

by performing the optimization problem

$$\text{minimize} \quad \Psi_{\text{dyn,2}}(\mathbf{f}_1) = \|\mathbf{P}\mathbf{f}_1 - \mathbf{g}_{\text{dyn}}\|^2 + \gamma \mathrm{p}_{\text{vessels}}(\mathbf{f}_1)$$
$$\text{with} \quad \forall i \in \{1, \dots, n\}, \quad (\mathbf{f}_1)_i \geq 0,$$

which is a minimization problem that includes our vessel prior, using dynamic data with no motion compensation. The obtained score is denoted $\mathfrak{R}_{\text{dyn}}(c, 2)$.

5. A fifth score is a reconstruction by solving

$$\text{minimize} \quad \Psi_{\text{gated,1}}(\mathbf{f}_1) = \|\mathbf{P}_{\Theta_1}\mathbf{f}_1 - \mathbf{g}_1\|^2 + \gamma \mathrm{p}_\beta(\mathbf{f}_1)$$
$$\text{with} \quad \forall i \in \{1, \dots, n\}, \quad (\mathbf{f}_1)_i \geq 0,$$

which is a gated MAP reconstruction using gated projections of $\mathbf{f}_1$ at angles $\Theta_1 = \{\vartheta_{1,1}, \vartheta_{2,1}, \vartheta_{3,1}, \vartheta_{4,1}\}$. The obtained score is denoted $\mathfrak{R}_{\text{gated}}(c, 1)$.

6. A sixth score is calculated solving the same minimization problem, with our vessel prior:

$$\text{minimize} \quad \Psi_{\text{gated,2}}(\mathbf{f}_1) = \|\mathbf{P}_{\Theta_1}\mathbf{f}_1 - \mathbf{g}_1\|^2 + \gamma \mathrm{p}_{\text{vessels}}(\mathbf{f}_1)$$
$$\text{with} \quad \forall i \in \{1, \dots, n\}, \quad (\mathbf{f}_1)_i \geq 0.$$

The obtained score is denoted $\mathfrak{R}_{\text{gated}}(c, 2)$.

7. A seventh score is calculated by performing a motion compensated method using the image prior p_β:

$$\text{minimize} \quad \Psi_{\text{comp},1}(\mathbf{f}_1) = \|\mathbf{PW}(\alpha)\mathbf{f}_1 - \mathbf{g}_{\text{dyn}}\|^2 + \gamma p_\beta(\mathbf{f}_1)$$

$$\text{with} \quad \forall i \in \{1, \dots, n\}, \quad (\mathbf{f}_1)_i \geq 0.$$

The obtained score is denoted $\mathfrak{R}_{\text{comp}}(c, 1)$.

8. A eighth and last score corresponds to our method, *Reconstruction with Motion Compensation using a Vessel Prior* (see [Bousse 2009]), which is the minimization process described in section 4.4.5:

$$\text{minimize} \quad \Psi_{\text{comp},2}(\mathbf{f}_1) = \|\mathbf{PW}(\alpha)\mathbf{f}_1 - \mathbf{g}_{\text{dyn}}\|^2 + \gamma p_{\text{vessels}}(\mathbf{f}_1)$$

$$\text{with} \quad \forall i \in \{1, \dots, n\}, \quad (\mathbf{f}_1)_i \geq 0.$$

The obtained score is denoted $\mathfrak{R}_{\text{comp}}(c, 2)$.

All these minimization problem were solved using a gradient descent method, and the algorithm initialization was set to

$$\mathbf{f}_1^{\text{init}} = 0 \in \mathbb{R}^{n^3}.$$

The difference between this initialization and the solution $\mathbf{f}_1^*$ we are seeking is very large, and this fact combined with the gradient descent method may lead to the convergence to local minima of the defect functions that are wrong solutions of our problem, as we will discuss in section 4.5.4.3. The corresponding values are displayed in tables 4.7 and 4.8

Table 4.7: Reference scores for tomographic reconstruction of the left coronary tree.

$\mathfrak{R}_{\text{static}}(l, 1)$	$\mathfrak{R}_{\text{static}}(l, 2)$	$\mathfrak{R}_{\text{dyn}}(l, 1)$	$\mathfrak{R}_{\text{dyn}}(l, 2)$	$\mathfrak{R}_{\text{gated}}(l, 1)$	$\mathfrak{R}_{\text{gated}}(l, 2)$	$\mathfrak{R}_{\text{comp}}(l, 1)$	$\mathfrak{R}_{\text{comp}}(l, 2)$
17%	14 %	70%	58%	48%	47%	57%	39%

Table 4.8: Reference scores for tomographic reconstruction of the right coronary right tree.

$\mathfrak{R}_{\text{static}}(r, 1)$	$\mathfrak{R}_{\text{static}}(r, 2)$	$\mathfrak{R}_{\text{dyn}}(r, 1)$	$\mathfrak{R}_{\text{dyn}}(r, 2)$	$\mathfrak{R}_{\text{gated}}(r, 1)$	$\mathfrak{R}_{\text{gated}}(r, 2)$	$\mathfrak{R}_{\text{comp}}(r, 1)$	$\mathfrak{R}_{\text{comp}}(r, 2)$
13%	15%	88%	73%	54%	50%	88%	41%

The optimal γ value for each reconstruction is equal to 2.5, and this value was used to calculate these reference scores. In figure 4.12 (resp figure 4.14) are displayed 4 projections

of the left (resp. right) coronary tree, using a motion compensated MAP reconstruction. In figure 4.13 (resp. figure 4.15) we show the reconstruction of the left (resp. right) coronary tree using our method: motion compensated reconstruction using a vessel prior. On these 4 figures we can clearly see the effect of our vessel prior.

4.5.4.3 Discussion

The first expected result is the following: in each case (left or right coronary tree, MAP reconstruction or reconstruction using our vessel prior), the reconstruction gives the best results when the object is not affected by motion as the projections are performed. These values $\mathfrak{R}_{\text{static}}(c, j)$, can be considered as lower boundeness scores for the 2 proposed image prior. The second expected result is that the worst reconstruction scores are $\mathfrak{R}_{\text{dyn}}(c, j)$, which clearly shows the effect of the motion cannot be neglected if the whole set of projections is to be used. Finally, for both coronary tree and both reconstruction method, we have

$$\forall (c, j) \in \{l, r\} \times \{1, 2\}, \quad \mathfrak{R}_{\text{dyn}}(c, j) > \mathfrak{R}_{\text{gated}}(c, j),$$

which means that the reconstruction is more accurate when using gated projection at angles $\Theta_1 = \{\vartheta_{1,1}, \ldots, \vartheta_{4,1}\}$ rather than using the full set of projections with no motion compensations. The rest of the discussion depends on the coronary tree we are working on.

The left coronary tree: two conclusions can be drawn:

1. For reconstruction with our vessel prior, we have

$$\mathfrak{R}_{\text{gated}}(l, 2) > \mathfrak{R}_{\text{comp}}(l, 2),$$

which means that it is better to consider the full set of projections with motion compensation rather than gated projections at angles $\Theta_1 = \{\vartheta_{1,1}, \ldots, \vartheta_{4,1}\}$. Note that $\mathfrak{R}_{\text{comp}}(l, 2) = 39\%$, which correspond to our proposed method, is the best score we obtained on the left coronary tree.

2. MAP reconstruction gives better results when using gated projections at angles $\Theta_1 = \{\vartheta_{1,1}, \ldots, \vartheta_{4,1}\}$ rather than considering the full set of projections with motion compensation. This observation is in contradiction with the previous one, and can be explained by the fact that the motion parameter estimation α is not accurate enough. In order to verify this assumption, we propose the following experiment: for all s in $\{2, \ldots, 20\}$, let

$$\mathbf{f}_s(\alpha) = \mathbf{W}(\alpha)\mathbf{f}_1^*, \quad \mathbf{g}_s(\alpha) = \mathbf{P}_{\vartheta_s}\mathbf{f}_s(\alpha)$$
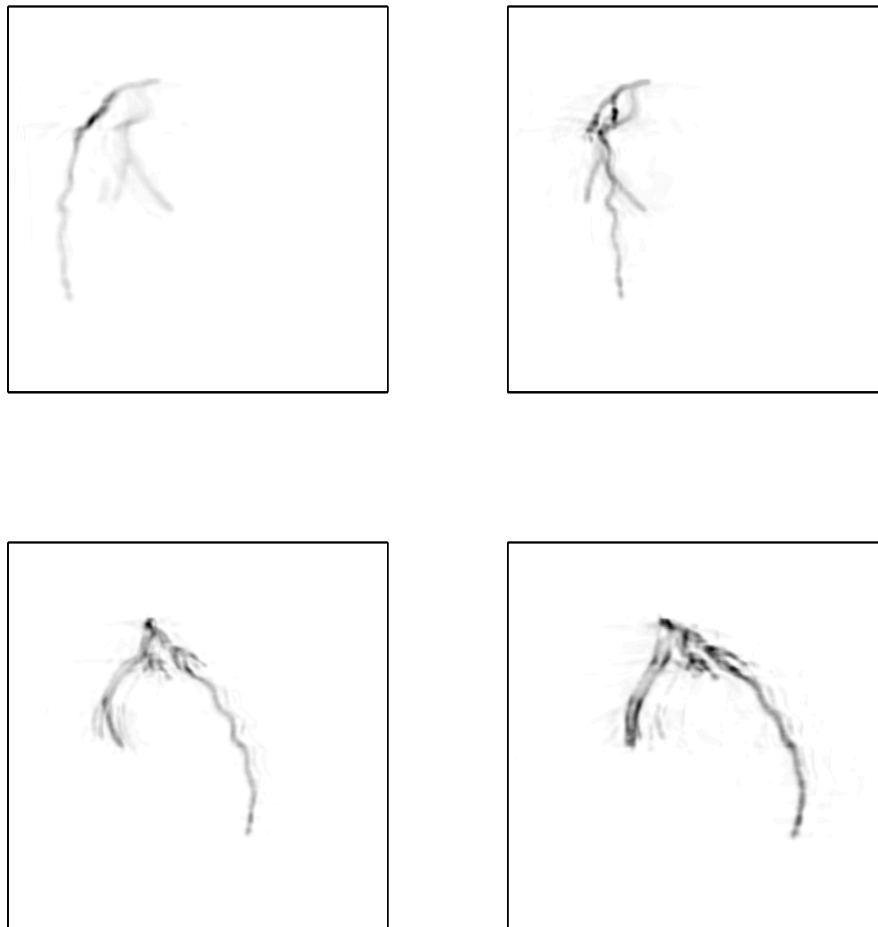
Figure 4.12: Motion compensated MAP reconstruction of the left coronary tree

Figure 4.13: Motion compensated reconstruction using our vessel prior of the left coronary tree

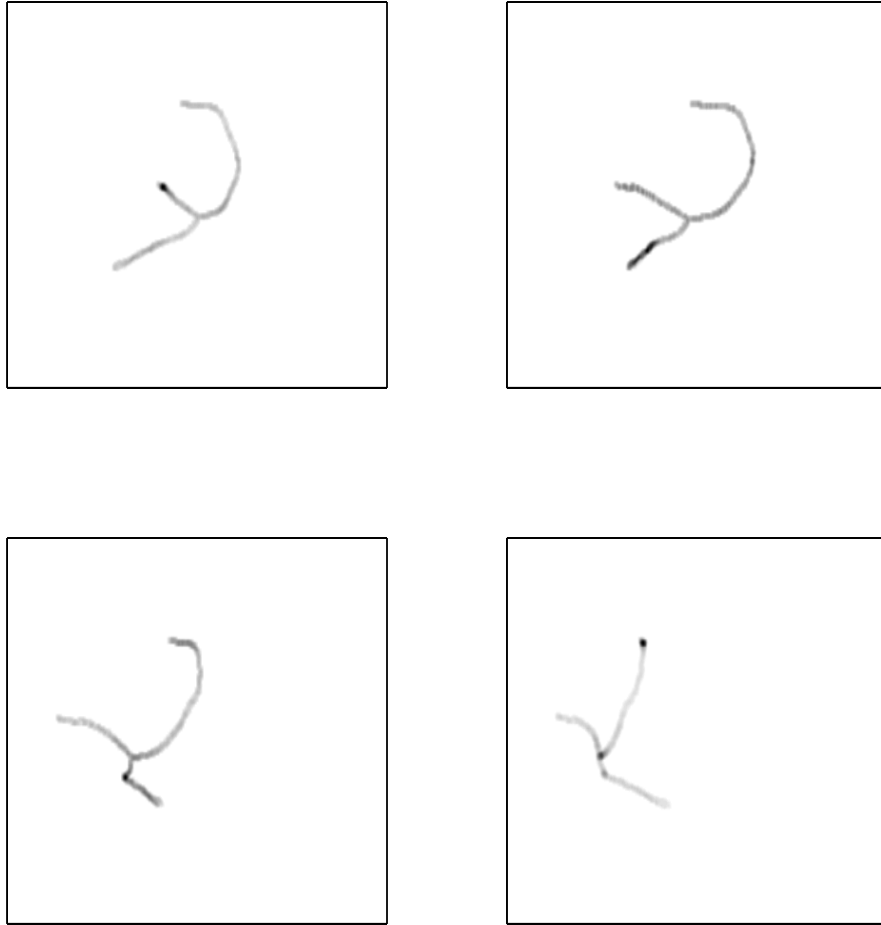Figure 4.14: Motion compensated MAP reconstruction of the right coronary tree

Figure 4.15: Motion compensated reconstruction using our vessel prior of the right coronary tree

and

$$\mathbf{g}_{\mathrm{dyn}}(\alpha) = \begin{bmatrix} \mathbf{g}_1 \\ \mathbf{g}_2(\alpha) \\ \vdots \\ \mathbf{g}_{20}(\alpha) \end{bmatrix}.$$

$\mathbf{g}_{\mathrm{dyn}}(\alpha)$ is the projection vector of a dynamic object $\mathbf{f}_1^*, \mathbf{f}_2(\alpha), \ldots, \mathbf{f}_{20}(\alpha)$ whose motion is fully determined by the operator $\mathbf{W}(\alpha)$, which is known in this situation. We now perform the following optimization:

$$\text{minimize} \quad \Psi_{\alpha,1}(\mathbf{f}_1) = \|\mathbf{P}\mathbf{W}(\alpha)\mathbf{f}_1 - \mathbf{g}_{\mathrm{dyn}}(\alpha)\|^2 + \gamma \mathrm{p}_\beta(\mathbf{f}_1)$$

$$\text{with} \quad \forall i \in \{1, \ldots, n\}, \quad (\mathbf{f}_1)_i \geq 0.$$

The reconstruction score we obtain is

$$\widetilde{\mathfrak{R}}_{\mathrm{comp}}(l, 1) = 42\% < \mathfrak{R}_{\mathrm{gated}}(l, 1) = 48\%.$$

Moreover, solving

$$\text{minimize} \quad \Psi_{\alpha,2}(\mathbf{f}_1) = \|\mathbf{P}\mathbf{W}(\alpha)\mathbf{f}_1 - \mathbf{g}_{\mathrm{dyn}}(\alpha)\|^2 + \gamma \mathrm{p}_{\mathrm{vessels}}(\mathbf{f}_1)$$

$$\text{with} \quad \forall i \in \{1, \ldots, n\}, \quad (\mathbf{f}_1)_i \geq 0$$

leads to a reconstruction error $\widetilde{\mathfrak{R}}_{\mathrm{comp}}(l, 2) = 29\%$.

These results show that for both method (MAP or reconstruction with our vessel prior), if the motion is well estimated, the reconstruction gives the best results with 80 projections and motion compensation.

The right coronary tree: the two observations we mentioned for the left coronary tree are also valid for the right coronary tree. The best score is the one obtained with our proposed method: $\mathfrak{R}_{\mathrm{comp}}(r, 2) = 41\%$. We also observe a very large error for the MAP reconstruction with motion compensation, $\mathfrak{R}_{\mathrm{comp}}(r, 1) = 88\%$ which is far much larger than the MAP reconstruction using gated projection ($\mathfrak{R}_{\mathrm{gated}}(r, 1) = 54\%$). We therefore performed the same test as for the left coronary tree. We obtained the two following results:

$$\widetilde{\mathfrak{R}}_{\mathrm{comp}}(r, 1) = 88\%, \quad \widetilde{\mathfrak{R}}_{\mathrm{comp}}(r, 2) = 35\%.$$

As for the left coronary tree, the results are improved for the motion compensated reconstruction using our vessel prior when the motion is known. However, there are no improvement for

the motion compensated MAP reconstruction. We interpret this phenomenon by the fact that the motion amplitude is larger for the right coronary tree which may lead any gradient descent method applied on $\Psi_{\alpha,1}(\mathbf{f}_1)$ to converge to a local minimum. This conjecture is confirmed by two facts:

1. The minimization of $\Psi_{\alpha,2}(\mathbf{f}_1)$ and $\Psi_{\mathrm{comp},2}(\mathbf{f}_1)$ with a gradient descent method converge to correct minimizers, according to the reconstructions error $\widetilde{\mathfrak{R}}_{\mathrm{comp}}(l,2) = 29\%$ and $\mathfrak{R}_{\mathrm{comp}}(r,2) = 41\%$. This may be due to our vessel prior $\mathrm{p}_{\mathrm{vessels}}$ which force the minimizers to be close to $\mathbf{f}_1^*$.

2. If the initialization $\mathbf{f}_1^{\mathrm{init}}$ is set to be equal to the real volume $\mathbf{f}_1^*$, the algorithm converges to a solution whose reconstruction error is close to zero. This means that $\Psi_{\alpha,1}(\mathbf{f}_1)$ has a local minimum in a neighborhood of $\mathbf{f}_1^*$.

Considering these local minima issue and our method, it could be interesting to follow this reconstruction process: starting the reconstruct using our motion compensated method that includes the vessel prior and for the q_0 first iterations, in order to approach the right minimum, then switch to a motion compensated MAP reconstruction.

4.6 Conclusion

In this chapter we presented a three stages method for coronary arteries tomographic reconstruction from a full rotational X-ray sequence. Let us summarize the steps we have been going through:

- Estimation of coronary 3-D centrelines at each cardiac phase using a deformable coronary 3-D model

- Estimation of a B-spline motion motion function which maps any coronary 3-D centreline to the one at the first cardiac phase

- Motion compensated tomographic reconstruction based on a penalized least-squares method, which includes a vessel prior

The first stage is the most difficult since it involves strong data pre-treatment: first of all, the initial coronary 3-D model has to be well estimated, which is itself a research topic in coronary 3-D reconstruction. Second, the 2-D centrelines must be extracted on each projection, vessel

endpoints must be identified and the branches must be labeled. In practical case, it is quite common that vascular segments are missing, which could be a real issue for the data fidelity term we used. This difficulty can be partially overcome if an algorithm is able to determine whether if 2-D centrelines are missing or not, by comparing the 2-D data to the 3-D model. If this knowledge is at our disposal, it can be taken into consideration by weighting the data fidelity terms in order to lower the importance of 2-D distance values of points concerned by missing data. This issue has to be investigated in our further work. Third, projections have to be gated according to the ECG. This step is based on the fact that the dynamic volume is periodic with respect to the time. Obviously, this statement may not hold when cardiac disorders are present. Such comments can be applied to all imaging modalities which use an ECG synchronization.

The second stage depends on the results of the first one only. If 3-D models are well reconstructed, the motion estimation is easily performed thanks to the one to one correspondence between each 3-D models throughout a least-square optimization problem.

The last stage main issue is the data pre-treatment as well: the back ground has to be removed on each projections. The least-squares minimization problem is subject to local but is overcome by our vessel prior. This vessel prior depends on the first 3-D model which is assumed to be known.

For all these reasons, we only have been able to work on simulated data and we cannot conjecture about its efficiency on a real data set. However, in this chapter we have clearly proven the role played by motion compensation in rotational angiography, especially the fact that the results are more satisfying if the volume is to be reconstructed from a full data set with motion compensation rather than using a few gated projections only, as it is more commonly performed. We have also proven that if the motion is well compensated, the reconstruction error is comparable to the one obtained from a static reconstruction using a full rotational X-ray sequence.

Conclusion

This work has addressed the tomographic reconstruction by first introducing the generic aspects of inverse problems which represent its theoretical basis. The choice of algebraic formulation has been motivated by several reasons. It allows to deal with the reconstruction problem independently of the geometry we consider (parallel, fan or cone beam) and to get a general matrix formulation. The introduction of penalty functions or prior on the object is easy and can provides a regular reconstruction. Another advantage is brought by its capability to incorporate deformation functions of the support, something that analytical methods can not do, at least easily. In cardiac angiography, the motions are complex and difficult to represent by parametric models (e.g. a family of deformations defined with only few parameters). We have developed in this basic frame some new theorems in the infinite-dimensional case (chapter 2) and formulated the dynamic tomographic inverse problem in a new way (chapter 2).

The practical situation which has been considered is the dynamic reconstruction applied to coronary arteries. We are aware that simplifications have been made at different levels. The aim in fact was to determine the performances that could be expected in an almost ideal case. This is only possible through simulations and our simulations of course simplified the problem at hand. For instance, we reduced the resolution of the projection images and subsequently the resolution of the structure of interest. The justification was of course the computational resources required (data storage but also number of operations). The computation load is one characteristic among others which has to be taken into account. Another example can be taken from the data and the object. The latter means that the coronary tree can not be reduced to 5 or 6 branches, as we did, small segments bringing anatomical references useful for the clinical interpretation even if no intervention can be carried out on them due to their sizes. The data, e.g projections, are much more complex: they contain the enhanced vessels but at the same time the contributions of the all tissues (especially but not limited to the

bones) traversed by the X-rays. Standard techniques applied in the past were based on mask subtraction which are not considered by now. The multiple components of real data make more difficult the extraction of centerlines and their tracking over the space and time. Conversely, the solution used for motion estimation should very likely be improved and thus a new balance established between complexity of the projection contents and robustness of motion estimation. The simulations can be made more realistic by adding noise, non-stationary background and estimation errors, but the evaluation on real data is required anyway.

Another perspective is offered by the alternatives described chapter 4. Without coming to all of them, the preliminary attempt, based on a first reconstruction of the vessels from few, ECG synchronized, projections and then the use of the projection image sequence, is promising. Several schemes can be designed from that. For example, and for illustration purpose only, assuming that the first reconstruction is not error free (false structures, rough approximation of the vessel supports, etc.) but has however some relevance, we can extract the 3-D skeletons, re-project them onto the next projection images ("next" means here in space and time), estimate the motion, compensate it to improve the first reconstruction (outliers should be eliminated too), and reiterate the process over the full projection image sequence. Another way would be to perform multiple reconstructions from few views like before and then match the resulting 3-D objects to estimate the motion field and compensate for it.

To go further, the future of cardiac imaging is open from our point of view. MRI, US and MDCT will be part of it. The trends for X-ray systems are clearly visible but they also involve some important limitations. At the technological level, the next step would be ideally to merge the concept of X-ray rotational with the Multidetector CT, in other words, the extension of the 64–128 detectors system to a full 2-D detectors CT. The advantages are obvious: faster acquisition rates, less or none translation of the bed. Some drawbacks can be anticipated however, among which the concerns about X-ray irradiation (the option to modulate the energy used is of course of interest here) and the lost of interventional capability if the system is not open such as MRI devices. Solutions to some of these problems are nevertheless possible by reducing the energy delivered and using more sensitive detectors. If we accept the idea that X-ray systems will continue to improve while reducing their side-effects, then, one of the most challenging topic will remain to image the small structures of the heart, the coronary arteries, the veins and perhaps tomorrow, the valves.

Appendix A

A blob-based tomographic reconstruction of 3D coronary trees from rotational X-ray angiography

Jian Zhou[a,b,c,d], Alexandre Bousse[a,b,c,d], Guanyu Yang[a,b,c,d], Jean-Jacques Bellanger[b,c,d],Limin Luo[a,d], Christine Toumoulin[b,c,d] and Jean-Louis Coatrieux[b,c,d]

[a]Laboratory of Image Science and Technology (LIST), Southeast University, Nanjing, China;
[b]INSERM, U642, Rennes, France;
[c]Université de Rennes 1, LTSI, Rennes, France;
[d]Centre de Recherche en Information Biomédicale Sino-français (CRIBs), Rennes, France.

abstract

A method is proposed for a 3D reconstruction of coronary networks from rotational projections that departs from motion-compensated approaches. It deals with multiple views extracted from a time-stamped image sequence through ECG gating. This statistics-based vessel reconstruction method relies on a new imaging model by considering both the effect of background tissues and the image representation using spherically-symmetric basis functions, also called 'blobs'. These blobs have a closed analytical expression for the X-ray transform, which makes easier to compute a cone-beam projection than a voxel-based description. A

Bayesian maximum *a posteriori* (MAP) estimation is used with a Poisson distributed projection data instead of the Gaussian approximation often used in tomography reconstruction. A heavy-tailed distribution is proposed as image prior to take into account the sparse nature of the object of interest. The optimization is performed by an expectation-maximization like (EM) block iterative algorithm which offers a fast convergence and a sound introduction of the non-negativity constraint for vessel attenuation coefficients. Simulations are performed using a model of coronary tree extracted from multidetector CT scanner and a performance study is conducted. They point out that, even with severe angular undersampling (6 projections over 110 degrees for instance) and without introducing a prior model of the object, significant results can be achieved.

keywords

cone-beam, coronary, reconstruction, X-ray, angiography, blob, maximum *a posteriori*.

A.1 Introduction

Coronary arterial disease is a major cause of mortality especially in Europe and the US. Quantitative and accurate characterization of stenoses (length, cross-sectional area) as well as their location within the whole coronary network is thus of major importance for diagnosis and treatment. The 3D reconstruction of arterial trees enhanced with contrast agent has attracted much attention for years using 2D angiographic image sequences with fairly high time resolution. This problem has been addressed first through computer vision approaches using mono- and bi-plane systems with epipolar techniques and feature matching in order to find corresponding primitives and retrieve their 3D geometry. However, the resolution of this ill-posed problem requires either a prior model [Garreau 1991], additional views [Venaille 1992], or the joint use of motion [Ruan 1994]. All the reported methods rely on a robust and accurate detection capable to provide in a first step the vessel centerlines, which is difficult to obtain without a significant user interaction (refer to [Coatrieux 1994] for a review). The availability of X-ray C-arm imaging systems opens now new perspectives for this reconstruction. While the clinician already gets more insights into the full 3D anatomy during the rotation of the C-arm (covering up to 180–240 degrees within a 7–8 seconds), the full 3D reconstruction may take benefit of a higher number of projections (150–200) by using tomographic methods. Several options can be considered. One first consists to perform a motion-compensated tomographic reconstruction,

inspired from Bonnet's work [Bonnet 2003], using the motion of the coronary arteries previously estimated by means of computer vision methods [Blondel 2006]. Such method is highly dependent on a critical pre-processing step and on the reliability of the motion estimate. Another way is to carry out the reconstruction from very few views (typically 5–8), corresponding to a single cardiac phase, selected by ECG-gating. A 3D reconstruction of centerlines has been proposed by exploring the 3D voxelized space, region growing and reprojection [Jandt 2007]. A fully iterative method has been reported in [Hansis 2007, Movassaghi 2007] by minimizing the L1-norm of the reconstructed image and a regularization based on vesselness and Gibbs smoothing priors.

This contribution describes an iterative reconstruction using a block sequential regularized EM (expectation-maximization) algorithm (BSREM) [Pierro 2003] for maximizing a regularized Poisson likelihood estimation, where the update is multiplicative. Instead of using a voxel basis, we consider a spherically-symmetric basis function (*i.e* the blob basis), the Kaiser-Bessel (KB), which has shown attractive properties [Lewitt 1990]. A 3D realistic phantom data set has been built using a coronary tree extracted from MDCT volume image. Cone beam projections have been computed from this phantom, with and without a background added coming from real angiographic projections. A performance study has then been conducted in terms of convergence, reconstruction error.

A.2   Method

The imaging geometry used in most recent rotational X-ray angiography systems is a cone-beam geometry. We consider a monoenergetic X-ray source, the ideal projection function due to this point source is:

$$Y(\mathbf{u};\,\theta(t)) \propto \exp\left\{-\int \underline{\mu}\left(\mathcal{T}(\theta(t))\left[\mathbf{x}_0 + s \cdot \frac{\mathbf{x}_d(\mathbf{u}) - \mathbf{x}_0}{\|\mathbf{x}_d(\mathbf{u}) - \mathbf{x}_0\|}\right];\,t\right)\mathrm{d}s\right\} \qquad (A.1)$$

where $\mathbf{u} = [u_1, u_2]' \in \mathbb{R}^2$, $\mathbf{x}_0 = [0, -d, 0]'$ and $\mathbf{x}_d(\mathbf{u}) = [u_1, D-d, u_2]'$ (where d is the distance from the source to the center of rotation, and D the source-to-detector distance), $\|\cdot\|$ is the standard Euclidean norm. $\mathcal{T}(\theta(t))$ is the three-dimensional rotation transform:

$$\mathcal{T}(\theta(t)) = \begin{bmatrix} \cos(\theta(t)) & -\sin(\theta(t)) & 0 \\ \sin(\theta(t)) & \cos(\theta(t)) & 0 \\ 0 & 0 & 1 \end{bmatrix} \qquad (A.2)$$

where $\theta(t)$ gives the projection angle at time t. The term $\underline{\mu}(\mathbf{x}; t)$ ($\mathbf{x} \in \mathbb{R}^3$) represents the total linear X-ray attenuation coefficient corresponding to the sum of the contribution of the dyed blood vessels of interest μ and the background tissue μ_{b}, *i.e.*

$$\underline{\mu}(\mathbf{x}; t) = \mu(\mathbf{x}; t) + \mu_{\mathrm{b}}(\mathbf{x}; t). \tag{A.3}$$

In real cases, data acquisition is usually done with several discrete time instances, e.g. $\{t_1, \ldots, t_K\}$. By letting $\theta_k \equiv \theta(t_k)$ ($k = 1, \ldots, K$), we have a projection sequence $\{Y(\mathbf{u}; \theta_k)\}$. From equation (A.3), we see that both arteries and background tissues are projected. The contribution of background tissues is significant in angiogram, and cannot be ignored. One conceptually simple way is to acquire additional projection images of background tissues, denoted by $\{Y_{\mathrm{b}}(\mathbf{u}; \theta_k)\}$, and to perform logarithmic subtractions: $\log Y_{\mathrm{b}}(\mathbf{u}; \theta_k) - \log Y(\mathbf{u}; \theta_k)$. However, this is unrealistic since, at least, it requires that the X-ray system has a very accurate repositioning so that it can provide two spatially matched sequences. In addition, any patient motion between the acquisitions will produce artifacts due to incomplete subtraction. An alternative solution is to numerically approximate the background and then subtract it.

In this paper, we adopt this latter strategy with a slightly different implementation. Suppose we already have virtual background images $\hat{Y}_{\mathrm{b}}(\mathbf{u}; \theta_k)$. Instead of a logarithmic subtraction as shown previously, we propose the following approximation for the kth projection image:

$$Y(\mathbf{u}; \theta_k) \propto \hat{Y}_{\mathrm{b}}(\mathbf{u}; \theta_k) \exp\left\{ -\int \mu\left(\mathcal{T}(\theta_k) \left[\mathbf{x}_0 + s \cdot \frac{\mathbf{x}_d(\mathbf{u}) - \mathbf{x}_0}{\|\mathbf{x}_d(\mathbf{u}) - \mathbf{x}_0\|} \right]; t_k \right) \mathrm{d}s \right\}. \tag{A.4}$$

The challenge still remains when performing a direct reconstruction using $\{Y(\mathbf{u}; \theta_k)\}$. The vessel attenuation coefficient function μ is a function of time, depending on, e.g. the distribution of contrast agent, and much more important, the motion of vessels during the acquisition procedure. These effects lead to the inconsistency in projection data. We will consider in this paper that the attenuation within the vessel is constant over time and that all other motions (due to patient movement or respiration) can be neglected. Since the cardiac motion is relatively regular and periodical, through ECG gating, we are able to choose several projections from a rotational sequence which correspond to the same 3D heart motion. We have limited our reconstruction study to a single instant within a cardiac phase. We assume $Y(\mathbf{u}; \underline{\theta_k})$'s consist of $\underline{K}$ selected projection images. Further, we can use $\mu(\mathbf{x})$ instead of $\mu(\mathbf{x}; t_k)$ for conciseness. Now the task turns to how these selected angiographic images $Y(\mathbf{u}; \underline{\theta_k})$'s can be utilized to reconstruct $\mu(\mathbf{x})$ of interest.

As stated, this problem is close to the conventional static tomography reconstruction with, however, critical features: 1) Since a usual examination of coronary angiography is often taken in a relatively short time period (e.g. typically no more than four or five cardiac cycles), the number of consistent projections is small (*i.e.* $\underline{K}$ is small, usually less than 6), and projections may not be equally spaced; 2) For relatively low X-ray exposition, the angular scanning is severely limited (e.g. for a typical C-arm rotational X-ray angiography system, the dynamic angle range is less than $180°$). This is sharply in contrast to the conventional cone-beam tomography in which a normal scanning covers a full range of $360°$. Therefore, a direct 3D reconstruction of vessel from rotational X-ray angiography is indeed a very ill-posed problem. In the following section, we will discuss our approximation solution.

A.2.1 System Model

We transform the above problem into the discrete domain. A single projection image can be discretized and stored lexicographically in one vector. All projection vectors can be stacked one by one, leading to a large data vector $\mathbf{Y} = [Y_1, \ldots, Y_N]'$ (where N is the total number of projection data, and the prime represents the vector or matrix transpose). Only noisy data can be obtained and we assume that these data are independent random variables whose ensemble means, according to (A.4), can be expressed as

$$\bar{Y}_i(\mathbf{u}) \propto Y_{\mathrm{b}i} \exp\left\{-[\mathbf{A}\mathbf{u}]_i\right\} \tag{A.5}$$

for all $i = 1, \ldots, N$, where $Y_{\mathrm{b}i}$ is the ith element of the background image vector $\mathbf{Y}_{\mathrm{b}}$, $\mathbf{u} = [\mu_1, \ldots, \mu_J]'$ (where J is the length of $\mathbf{u}$) is a discrete representation of vessel attenuation coefficient function $\mu(\mathbf{x})$, $\mathbf{A}$ is the cone-beam projection operator, and $[\cdot]_i$ returns the ith entry of a vector in brackets.

Without loss of generality, we study here the vessel reconstruction within a cubic field of view. A typical image representation is to consider the piecewise continuous attenuation function $\mu(\mathbf{x})$ defined over the cubic region. It can be written as the superposition of scaled and shifted copies of the basis function $\Psi(\mathbf{x})$, as follows:

$$\mu(\mathbf{x}) = \sum_{j=1}^{J} \mu_j \Psi(\mathbf{x} - \mathbf{x}_j) \tag{A.6}$$

where $\{\mathbf{x}_j\}$ $(j = 1, \ldots, J)$ form a set of spatial basis locations (or grid points as well). There are many choices of basis functions, one of which is: $\Psi(\mathbf{x}) = 1$, if $\|\mathbf{x}\|_\infty \le 1/2$ else $\Psi(\mathbf{x}) = 0$

(assuming that the grid spacing is unitless 1). This is the so-called voxel basis that has a constant density inside the voxels. From a signal processing standpoint, it only provides, however, a poor interpolation. Instead of using voxel basis, we consider in this paper another basis family: the spherically-symmetric basis function (also known as the blob basis) which has the following general form:

$$\Psi(\mathbf{x}) = \mathcal{B}(\|\mathbf{x}\|) \tag{A.7}$$

where $\mathcal{B}(\cdot)$ is a circularly symmetric kernel. The concept of blob in tomography has been applied for image reconstruction, e.g. [Matej 1996, Daube-Witherspoon 2001, Wang 2004] etc. It is also widely used in the area of volume visualization, e.g. volume rendering [Muraki 1991]. An important blob basis is known as the Kaiser-Bessel (KB) kernel, which has shown certain attractive properties [Lewitt 1990]. It can be written as

$$\mathcal{B}_{m,\alpha,R}(r) = \begin{cases} \frac{1}{I_m(\alpha)} \left(\sqrt{1-(r/R)^2}\right)^m I_m\left(\alpha\sqrt{1-(r/R)^2}\right) & |r| \leqslant R \\ 0 & \text{otherwise} \end{cases} \tag{A.8}$$

where $I_m(\cdot)$ denotes the modified Bessel function of the first kind of order m, R is the radius of the blob, α is a non-negative real number controlling the shape of the blob. Usually, we take $m > 0$ so that the blob has $m-1$ continuous derivatives at the boundary.

A blob-based forward projection operator $\mathbf{A}$ can be determined according to the basic definition of X-ray projection (A.4). For one element a_{ij}, using the X-ray transform of the blob function at location $\mathbf{x}_j$ along the ith ray path Γ_i, we have

$$a_{ij} = \int_{\Gamma_i} \mathcal{B}_{m,\alpha,R}(\|\mathbf{x} - \mathbf{x}_j\|) \mathrm{d}\ell. \tag{A.9}$$

Since the X-ray transform of a KB kernel leads to another KB like kernel, *i.e.*

$$\underline{\mathcal{B}}_{m,\alpha,R}(r) = R\sqrt{\frac{2\pi}{\alpha}} \frac{I_{m+1/2}(\alpha)}{I_m(\alpha)} \mathcal{B}_{m+1/2,\alpha,R}(r), \quad |r| \leq R, \tag{A.10}$$

it follows that

$$a_{ij} = \underline{\mathcal{B}}_{m,\alpha,R}(\text{dist}[\mathbf{x}_j, \Gamma_i]) \tag{A.11}$$

with $\text{dist}[\mathbf{x}_j, \Gamma_i]$ the distance between the grid point j and the ray Γ_i.

A.2.2 Image MAP estimation

The commonly used maximum likelihood (ML) estimation finds an image reconstruction that maximizes the probability distribution of the projections, as well as the likelihood distribution.

The likelihood distribution, denoted by $\log \Pr(\mathbf{Y}|\mathbf{u})$, is characterized by the imaging model. Since the nature of X-ray observations is a counting process, this paper considers a Poisson likelihood

$$\log \Pr(\mathbf{Y}|\mathbf{u}) \propto \sum_i \{-\bar{Y}_i(\mathbf{u}) + Y_i \log(\bar{Y}_i(\mathbf{u}))\} \tag{A.12}$$

where terms independent of $\mathbf{u}$ has been ignored. The choice of this model is also due to another interpretation of the log-Poisson likelihood term which is the so-called *Kullback-Leiber* (KL) distance. The KL distance provides a measure of dissimilarity between two vectors $\mathbf{p}$ and $\mathbf{q}$, is defined by

$$\mathrm{KL}(\mathbf{p}, \mathbf{q}) = \sum_i \{p_i \log(p_i/q_i) - p_i + q_i\}. \tag{A.13}$$

Now letting $p_i = Y_i$ and $q_i = \bar{Y}_i(\mathbf{u})$ and also ignoring terms independent of $\mathbf{u}$, it can be shown that $\log \Pr(\mathbf{Y}|\mathbf{u}) \equiv -\mathrm{KL}(\mathbf{Y}, \bar{\mathbf{Y}}(\mathbf{u}))$ where $\bar{\mathbf{Y}}(\mathbf{u}) = [\bar{Y}_1(\mathbf{u}), \ldots, \bar{Y}_N(\mathbf{u})]'$. The proposed Poisson model is not specific: even for non-Poisson data, we are still able to seek a ML solution for which the likelihood term can be represented by $\Pr(\mathbf{Y}|\mathbf{u}) \propto \exp\{-\mathrm{KL}(\mathbf{Y}, \bar{\mathbf{Y}}(\mathbf{u}))\}$.

However, due to the typical limits in fidelity of data, ML estimates are often unstable, and have to be improved. Usually a unique and stable estimate is sought by incorporating prior information on the original image $\mathbf{u}$, leading to the well known Bayesian MAP estimation. In the MAP estimation, we are interested in the maximum of the posteriori distribution $\Pr(\mathbf{u}|\mathbf{Y})$. Using Bayes's rule, we rewrite $\Pr(\mathbf{u}|\mathbf{Y})$ as $\Pr(\mathbf{u}|\mathbf{Y}) \propto \Pr(\mathbf{Y}|\mathbf{u}) \Pr(\mathbf{u})$ where $\Pr(\mathbf{u})$ represents the image prior distribution. Then, the MAP estimation is found as

$$\hat{\mathbf{u}}_{\mathrm{MAP}} = \arg \max_{\mathbf{u}} \{\log \Pr(\mathbf{Y}|\mathbf{u}) + \log \Pr(\mathbf{u})\}. \tag{A.14}$$

The image prior is certainly the key to any MAP estimation. It can not only provide a stable solution but also improve the quality of reconstruction, e.g. by suppressing artifacts due to limited angle projections. One prior defined over a discrete grid system relates to the discrete Markov random field (MRF) on which a roughness measure can be constructed from local neighborhoods. Typically, $\Pr(\mathbf{u})$ has the following generic form

$$\Pr(\mathbf{u}) \propto \exp\{-\beta U(\mathbf{u})\} \tag{A.15}$$

where $U(\mathbf{u})$ is the energy function, and β an adjustable parameter. Let $\mathcal{N}_j$ be the neighborhoods of the jth grid. The energy function can be written as

$$U(\mathbf{u}) = \sum_j \sum_{s \in \mathcal{N}_j} \omega_{js} \phi(\mu_j - \mu_s) \tag{A.16}$$

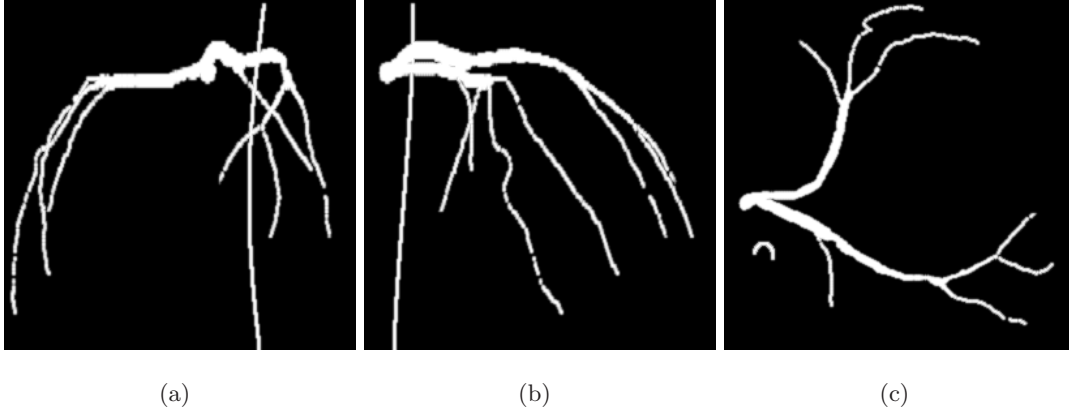| (a) | (b) | (c) |

Figure A.1: Computer simulated phantom. Figures from left to right are maximum intensity projections along three axes, x,y,z respectively.

where ω_{js} is the weight for the pair of grid points j and s. ϕ is the potential function, measuring the interaction between the two grid points. In coronary angiography, vessels having branch-like structures occupies a very small part of the volume, so a sparse object prior is of relevance. Now, consider the distribution of local neighborhood differences, *i.e.* $\mu_j - \mu_s$: it should be sharply peaked around zero, due to the contribution of most smooth areas, and have broad tails representing the contribution of the vessels (in particular their edges). Consequently, a sparse object prior can be modeled by a heavy-tailed distribution. With this in mind, we selected a potential function $\phi(t) = |t|$. The corresponding penalty relates to the Laplacian distribution that belongs to the family of heavy-tailed distribution. Another advantage is that the resulting $R(\mu)$ is close to the total variational (TV) regularization that is powerful for noise smoothing while edge preserving.

A.3   Simulation study

A.3.1   Materials

The experiments have been conducted using phantom data. The reference left coronary arteries were extracted from a volume of cardiac MSCT reconstructions [Yang 2006]. Figure refFIG:2 shows three maximum-intensity projections of the phantom along the three axes. Stenotic areas and a simulated catheter were also added.

    The imaging protocol used in this paper was adapted from the C-arm rotational X-ray
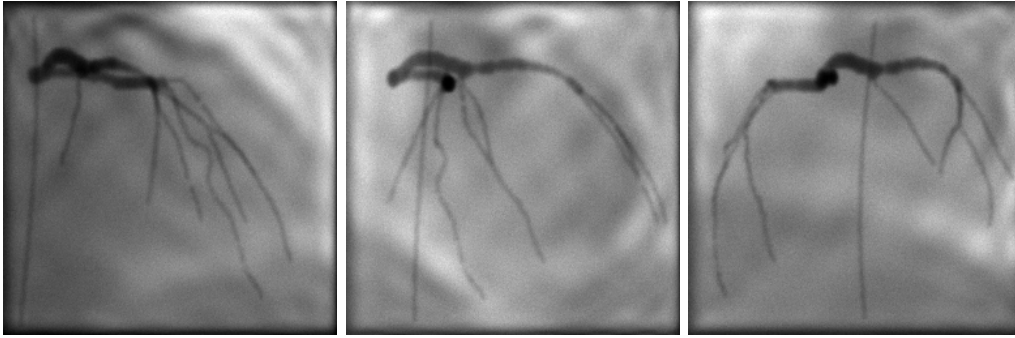
Figure A.2: Simulated noisy projection images at angle: (a)$-29.0°$, (b) $18.2°$, and (c) $65.4°$, respectively.

coronary angiography Siemens AXIOM-Artis system. The detector plane, 140^2 mm^2, which was sampled uniformly into 512^2 pixels. All reconstructions have been performed in a volume of (110 mm)^3. This field of view was also uniformly sampled into 128^3 grid points that served as blob locations. According to our discussion on the choice of blob basis, we have used $m = 2$, $\alpha = 6.0$, and $R = 1.5$ blob spacing for the calculation of operator $\mathbf{A}$. Six cone-beam vessel projection images, without background tissues, uniformly spaced over the range $120°$ were first generated (the starting angle is $-29.0°$). Then, we used the method of low order polynomials approximation to create the required background images $\hat{\mathbf{Y}}_{\mathrm{b}}$ (called later on the "true backgound") from some real angiography images acquired separately on the Siemens device. The mean observation data were produced according to the model (A.4). Poisson noisy data were then generated, which were used for reconstructions. Figure A.2 shows some examples of noisy projection images at different angular views.

A.3.2 Reconstruction

We focus our study on the iterative reconstruction algorithm. The image reconstruction was performed by BSREM [Pierro 2003]. In this algorithm, a fully iteration is divided into a set of subiterations, each being performed sequentially using one of the predetermined blocks of measurement data. In our simulation study, the data within each projection image were grouped into one block. Therefore, this leads to a total number of six blocks. The BSREM algorithm is an extension of RAMLA (row-action maximum likelihood algorithm) [Browne 1996] for maximizing a regularized Poisson likelihood estimation as (A.14). They relate to the well-known algebraic reconstruction technique (ART) [Gordon 1970], but the update is multiplicative

(rather than additive) and a grouped projection can be performed simultaneously. BSREM has been shown even faster with guaranteed global convergence properties [Pierro 2003].

A.3.3 Influence of background images

As discussed in Section 2, one can construct a set of new measurement data by using logarithm substraction. Let $\tilde{\mathbf{Y}} = -\log(\mathbf{Y}/\hat{\mathbf{Y}}_{\mathrm{b}})$. Then, $\tilde{\mathbf{Y}}$ serves as the approximate observations of projections $\mathbf{Au}$. In [Blondel 2006, Hansis 2007], the authors have used $\tilde{\mathbf{Y}}$ to reconstruct the vessels of interest. This method was evaluated in this paper and compared with our strategy as expressed in (A.4). While the resulting data $\tilde{\mathbf{Y}}$ cannot be Poisson distributed, we still can use the BSREM algorithm but the data fidelity term should be interpreted as the KL distance, yielding a modified BSREM for image reconstruction from the presubtracted measurement data. We named it here the PreSub.+BSREM algorithm.

For comparison, we introduced two measures of error: 1) the global mean square error defined by

$$\mathrm{MSE}_{global}(n) = \frac{\|\hat{\mathbf{u}}^n - \mathbf{u}^{\mathrm{ref}}\|^2}{\|\mathbf{u}^{\mathrm{ref}}\|^2} \times 100\% \qquad (A.17)$$

which provides the normalized percentage error between the nth iteration $\hat{\mathbf{u}}^n$ and the reference volume $\mathbf{u}^{\mathrm{ref}}$. 2) the vessel mean square error denoted by $\mathrm{MSE}_{vessel}(n)$ defined in a similar way except that the error is only measured within the support of vessels instead of the entire field of view.

Table A.1 shows the global MSE values of the two different algorithms at several selected iteration number. We see that the smaller MSE_{global} can be obtained by the proposed BSREM. This possibly means that the logarithm substraction operation imposed before data processing may destroy the optimality of statistical based iterative algorithm, leading to a suboptimal one in terms of global mean square error. Figure A.3 shows the evolution of MSE_{vessel} during the iteration progress. Again, BSREM without pre-logarithm substraction shows a slight better

Table A.1: Comparison of MSE_{global} values (%) for PreSub+BSREM and BSREM (both with $\beta = 0$) at several iterations.

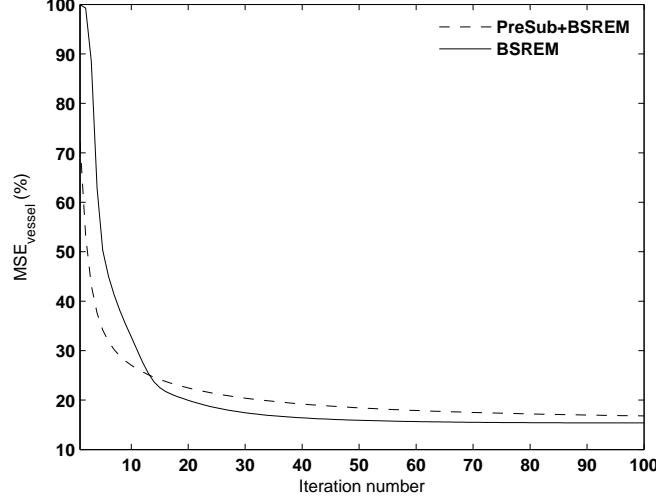| #Itr.	5	30	70	100
PreSub+BSREM	36.7	22.3	19.3	18.5
BSREM	52.1	18.7	16.6	16.5

performance.

Figure A.3: A comparison of MSE_{vessel} for PreSub+BSREM and BSREM ($\beta = 0$ for both algorithms) as the function of iteration. Here uses true background images $\hat{\mathbf{Y}}_{\text{b}}$.

As mentioned already, the background images are usually unavailable in practice, and they can only be estimated from the measured data. To obtain virtual projection images of background tissues, we have adapted the method used in [Blondel 2006, Hansis 2007]. First, we created the binary vessel mask. This is can be done by thresholding. Second, a morphological closure operation was applied to the noisy projection images to remove vessels. Here, the structure element was a disk whose radius has been chosen large enough to cover the blood vessels. Then, a virtual background image is obtained by combining the original projection image and the filtered image: the virtual background image takes the pixel value from the filtered image if the pixel belongs to a vessel according to the binary vessel mask images, otherwise we use the value on the original projection image. Figure A.4 shows some results when creating one virtual background image from the projection image at angle $-5.4°$.

The estimated background images, denoted by $\bar{\hat{\mathbf{Y}}}_{\text{b}}$, were combined with either BSREM or PreSub.+BSREM to investigate the effect of background tissues on reconstructions. Figure A.5 compares the maximum intensity projection images with either true or virtual background images. Noise and artifacts are clearly shown and this confirms that the accuracy of background images does affect the reconstruction quality. Nevertheless, they are mainly found in background regions, and most of the vascular structures can be preserved. Table A.2 lists some

MSE_{vessel} values yielded by the two approaches. The results seem to justify the same fact that the proposed BSREM can behave better than the one with pre-logarithm subtraction. However, it can be observed that the mean square error becomes larger over iterations. This is a common feature of iterative ML estimation that can produce an overfit to noisy data, leading to degeneration of reconstruction. An introduction of regularization (or setting $\beta > 0$ as well) should improve the solution and will be discussed next.

Figure A.4: Figures from left to right are 1) the projection image at angle $-5.4°$; 2) the corresponding binary vessel mask where the white color indicates the valid vessel regions. 3) the projection image after a morphological closure filtering with a disk type structure element of radius size 10 pixels; 4) the resulting virtual background image.

A.3.4   Choose image prior

This section evaluates the impact of the prior model on the 3D vessel reconstruction. From our former analysis, here the main task of prior is to reduce the background noise while preserving main vascular structures undestroyed. The comparison has been conducted between a heavy-tailed model and a non-heavy-tailed model. For the latter, we used the Gaussian quadratic prior model (where $\phi(t) = |t|^2$). The choice of parameter β is essential due to its smoothing effects. On the other hand, for a specific prior, the choice of β also can be different. Thus,

Table A.2: Comparison of MSE_{vessel} values (%) yielded by PreSub+BSREM and BSREM (both with $\beta = 0$ and estimated background image $\bar{\hat{\mathbf{Y}}}_b$) over iterations.

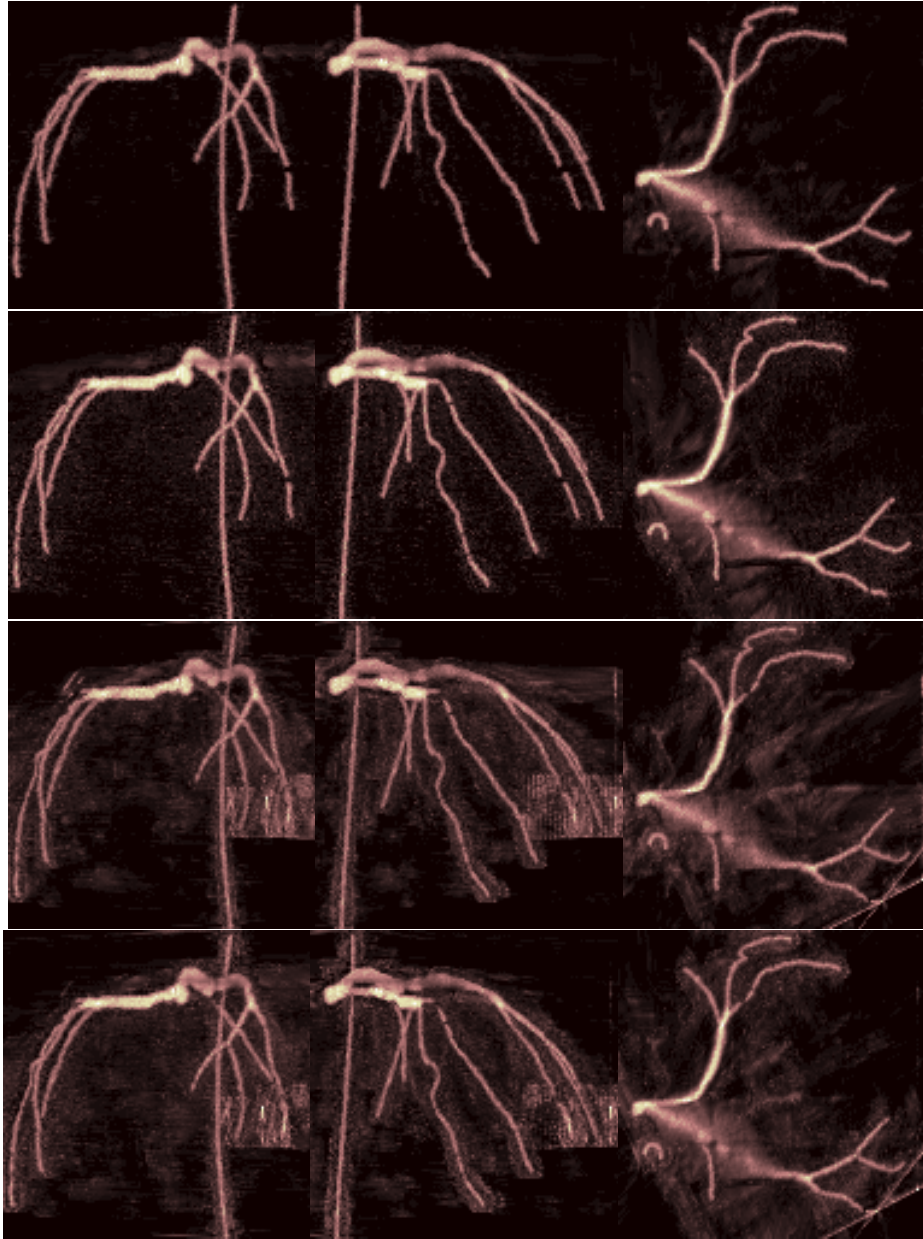| #Itr.	5	30	70	100
PreSub+BSREM	39.9	27.2	28.8	29.7
BSREM	57.4	26.1	27.7	27.2

Figure A.5: From top to bottom: maximum intensity projection images of reconstructions by using: BSREM (with $\hat{\mathbf{Y}}_{\mathrm{b}}$), PreSub+BSREM (with $\hat{\mathbf{Y}}_{\mathrm{b}}$), BSREM (with $\bar{\hat{\mathbf{Y}}}_{\mathrm{b}}$) and Pre-Sub+BSREM (with $\bar{\hat{\mathbf{Y}}}_{\mathrm{b}}$), respectively. ($\beta = 0$ for all algorithms)

for a fair comparison, we selected these model-based parameter with the aim to minimize the MSE_{vessel} error. More precisely, we chose several β values and recorded the corresponding the minima MSE_{vessel} value of reconstruction during iterations. We can trace out the relationship
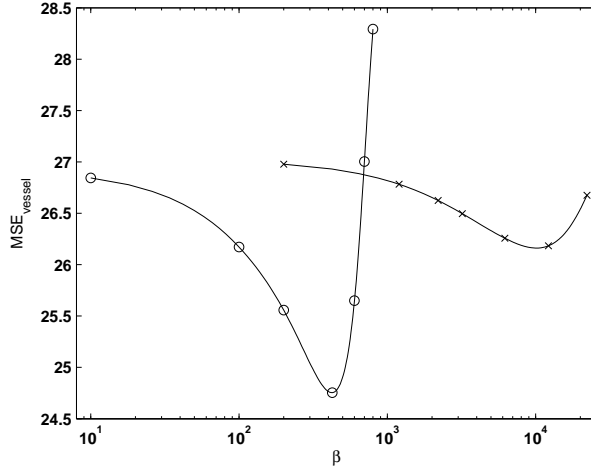
Figure A.6: A comparison of the minimum MSE$_{vessel}$ changes as a function of parameter β yielded by BSREM using different priors: quadratic prior (-×-) and total variation like prior (-○-). These two curves are generated by interpolation where discrete samples are indicated by symbols, *i.e.* circles and crosses. The optimal β values are approximately $\beta = 10^{4.0}$ for the quadratic prior, and $\beta = 10^{2.62}$ for TV-like prior.

on the β and MSE$_{vessel}$ plane. An interpolation between discrete samples is then made to predict a global optimal β. Figure A.6 shows two curves related to different priors. In our experiments, the optimal β for the quadratic prior is close to $10^{4.0}$ while for a TV-like prior it is about $10^{2.62}$. Note that the global minimum MSE$_{vessel}$ yielded by a TV-like prior is smaller than a quadratic prior, which points out the advantage of TV-like prior over a quadratic one in terms of reconstruction performance.

The results (MIP images) are displayed in figure A.7. It is clear that the introduction of prior leads to a successful suppression of background artifacts (Note that here we used the virtual background image instead of the true one). From a visual point of view, we also see that the sparse prior, as well as the TV-like prior, can provide even better result (a clear comparison from the top-to-down MIP images). Figure A.8 shows further visual comparisons by using 3D vessel surface rendering. All surfaces are rendered by using the same isosuface values extracted from various reconstructed volumes. Again a better result is obtained by the proposed TV-like prior. However, it is worth to note that both priors still fail to reconstruct some vessel parts marked with circles in figure A.8. Thus, the introduction of prior models
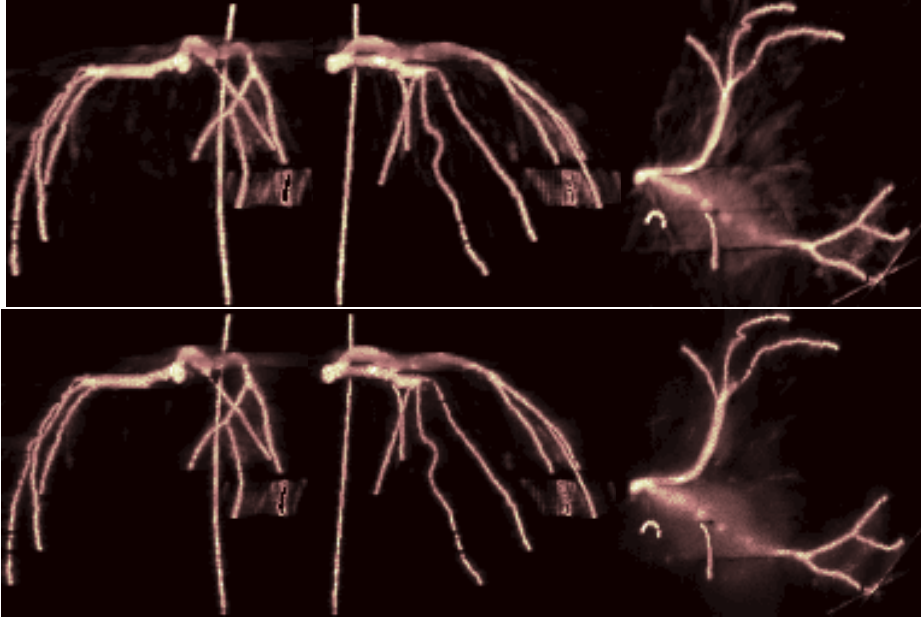
Figure A.7: A comparison of MIP of image reconstruction from BSREM using: the quadratic prior with $\beta = 10^{4.0}$ (the first row) and the TV-like prior with $\beta = 10^{2.62}$ (the second row).

may not fulfil the requirements due to the incomplete rotational X-ray scanning.

A.3.5 The effect of data inconsistency

Till now, the used projection images were motion free data (*i.e.* the same cardiac phase). In real case, the key assumption relies on the fact that the coronary network is observed exactly in the same position for different views: The reproducibility of the heart cycle and the temporal sampling may introduce some spatial shift. In other words, some inconsistency may exist. Two main motions were examined: rotation and translation. We simulated this data mismatch to explore how it affects the reconstruction. The heart rotation has been simulated by using a random bias, denoted by ϵ_{angle}, added to the projection angle. For translation, since the cardiac motion is mainly dominated by a up-down movement, we used a random up-down displacement $\epsilon_{displacement}$ to change the real vessel position when generating each projection image. We only studied the BSREM algorithm with the TV-like prior, and the virtual background images were estimated according to the same method described before. No pre-subtraction was used.

Figure A.9(a) plots about the changes of MSE_{vessel} against the maximum magnitude
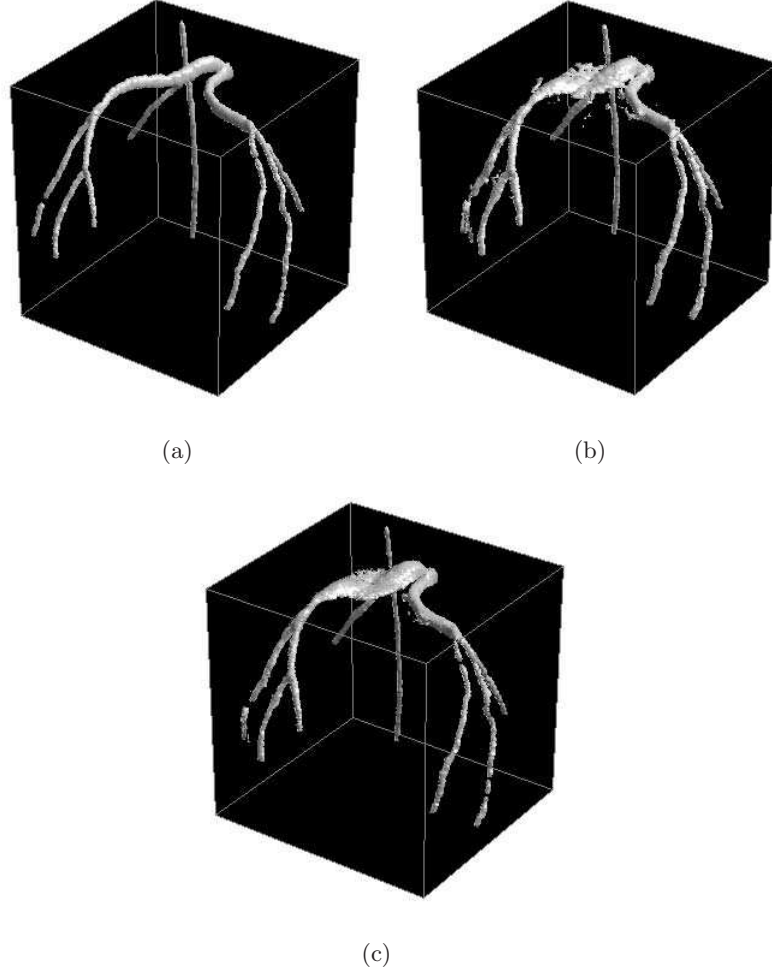
(a) (b)

(c)

Figure A.8: 3D vascular surface rendering using true vessel data (a), and data reconstructed by BSREM with the quadratic prior (b), and the TV-like prior (c).

of ϵ_{angle}, *i.e.* Δ_{angle}. Note that ϵ_{angle} is the uniform random number within the range $[-\Delta_{angle}, +\Delta_{angle}]$. We see clearly that the mean square error increases with error in angle. For an amount of $5°$ bias in angle, it results in almost three times larger error in reconstruction. Figure A.9(b) shows the relationship between MSE_{vessel} and the object displacement error $\epsilon_{displacement}$ (note also that $\epsilon_{displacement}$ is the uniform random number within the range $[-\Delta_{displacement}, +\Delta_{displacement}]$). The same behavior can be observed. They both show that if the assumption made does not hold, a significant degeneration in the quality of reconstruction can be anticipated.

A.4 Discussion and conclusion

We have described in this paper a method for the 3D reconstruction of coronary networks from sparse projections acquired through a rotational system within a limited angle rotation. This approach, applied in a first step in static conditions by assuming an error-free ECG gating, is based on a statistical modelling, blob basis functions (Kaiser-Bessel) and makes use of a block iterative algorithm (BSREM, block sequential regularized expectation-maximisation). Simulations have been performed by means of a realistic phantom representing an arterial tree extracted from a MDCT dataset in order to have a ground truth. The performance of the method has been assessed by using global statistics (mean square values over the reconstructed volume or over the vessel spatial support). The reconstructions that have been reported show some promising features. They also allow quantifying the influence of the background and the sensitivity to imprecise synchronization resulting in object misregistration (simulated by small translation and rotation errors).

It must be said that the reconstruction of coronary network remains a difficult problem in X-ray imaging (including the MDCT) for several reasons among which: the small size of the objects (few millimeters), the many structures contributing to the background, the
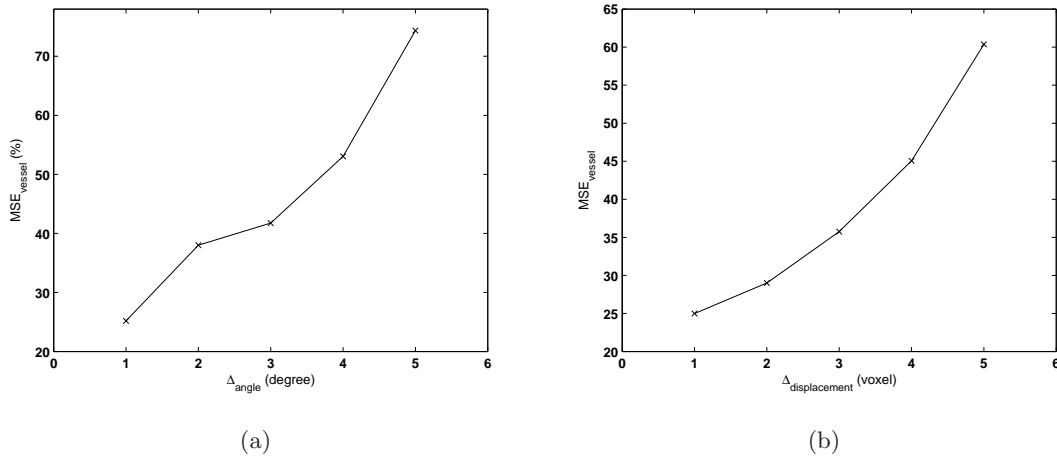

Figure A.9: (a) The changes of MSE$_{vessel}$ with Δ_{angle} when using the proposed BSREM algorithm coupled with a TV-like prior. Here, the β value is $10^{2.5}$. (b) MSE$_{vessel}$ evolution when varying $\Delta_{displacement}$ using the proposed BSREM algorithm coupled with a TV-like prior. Here, the β value is $10^{2.5}$.

patient movements, the ballistic inaccuracies and the time-varying heart cycle. Although this work-in-progress has been limited to a cone beam static situation, it opens a path to deal with dynamic reconstruction. In contrast to approaches that call first for 3D motion field estimation with feature matching, the solution that we are currently developing is based on a fully homogeneous tomographic frame. The availability of 3D dataset (single volume or time indexed multiple volumes) as shown here should serve as an initialization step for further refinements.

A.5   Acknowledgments

Bibliography

[Besl 1992] P.J. Besl and N.D. McKay. *A method for registration of 3-D shapes.* IEEE Trans. Pattern Anal. Mach. Intell., vol. 14, no. 2, pages 239–256, 1992. 69

[Block 1984] M. Block, Y.H. Liu, L.D Harris, R.A. Robb and E.L. Ritman. *Quantitative analysis of a vascular tree model with the dynamic spatial reconstructor.* J. Comput. Assist. Tomogr., vol. 8, pages 390–400, 1984. 52

[Blondel 2004] C. Blondel. *Modélisation 3D et 3D+T des artères coronaires à partir de séquences rotationnelles de projections rayons X.* PhD thesis, Université de Nice Sophia Antipolis, march 2004. 53, 59, 71

[Blondel 2006] C. Blondel, G. Malandain, R. Vaillant and N. Ayache. *Reconstruction of coronary arteries from a single rotational X-ray projection sequence.* IEEE Trans. on Med. Im., vol. 25, no. 5, pages 653–663, may 2006. 52, 53, 59, 71, 73, 105, 112, 113

[Bonnet 2003] Stephane Bonnet, A. Koenig, S. Roux, P. Hugonnard, R. Guillemaud and Pierre Grangeat. *Dynamic X-ray computed tomography.* Proceedings of the IEEE, vol. 91, no. 10, pages 1574–1587, 2003. 42, 45, 105

[Bouman 1993] C. Bouman and K. Sauer. *A generalized gaussian image model for edge-preserving MAP estimation.* IEEE Trans. on Im. Proc., vol. 2, no. 3, pages 296–310, 1993. 17

[Bousse 2008] A. Bousse, J. Zhou, G. Yang, J.-J. Bellanger and C. Toumoulin. *Motion estimation in X-ray rotational angiography using a 3-D Deformable coronary tree model.* In Computer in Cardiology, Bologna, Italy, 2008. 54

[Bousse 2009] A. Bousse, J. Zhou, G. Yang, J.-J. Bellanger and C. Toumoulin. *Motion compensated tomographic reconstruction of coronary arteries in rotational angiography.* To appear in IEEE Trans. on Biomed. Im., 2009. 54, 92

[Bracewell 1967] R.N. Bracewell and A.C. Riddle. *Inversion of fan-beam scans in radio astronomy.* The Astrophysical Journal, vol. 150, pages 427–434, 1967. 29

[Brezis 1999] H. Brezis. Analyse fonctionnelle : théorie et applications. Dunod, Paris, 1999. 1

[Browne 1996] J. Browne and A.R. De Pierro. *A row-action alternative to the EM algorithm for maximizing likelihood in emission tomography.* IEEE Trans. Med. Imaging, vol. 15, pages 687–699, 1996. 111

[Chen 2000] S.J. Chen and J.D. Carroll. *3-D reconstruction of coronary arterial tree to optimize angiographic visualization.* IEEE trans. on Med. Im., vol. 19, no. 4, pages 318–336, april 2000. 52

[Chui 2003] H. Chui and A. Rangarajan. *A new point matching algorithm for non-rigid registration.* Comput. Vis. Image Underst., vol. 89, no. 2-3, pages 114–141, 2003. 63, 69

[Clerc 2006] M. Clerc. Particle swarm optimization. ISTE, 2006. 60

[Coatrieux 1994] J.-L. Coatrieux, M. Garreau, R. Collorec and C. Roux. *Computer vision approaches for the three dimensional reconstruction of coronary arteries: review and prospect.* Critical Reviews Biomed. Eng., vol. 22, no. 1, pages 1–38, 1994. 52, 104

[Coppini 1991] G. Coppini, M. Demi, R. Mennini and G. Valli. *3-D knowledge driven reconstruction of coronary trees.* Med. Biol. Eng. Comput., pages 535–542, 1991. 52

[Cormen 2001] T.H. Cormen, C.E. Leiserson, R.L. Rivest and C. Stein. Introduction to algorithms. MIT Press and McGraw-Hill, 2001. 60

[Crawford 1996] C.R. Crawford, K.F. King, C.J. Ritchie and J.D. Godwin. *Respiratory compensation inprojection imaging using a magnification and displacement model.* IEEE trans. on Med. Im., vol. 15, pages 327–332, 1996. 45, 53

[Daube-Witherspoon 2001] M.E. Daube-Witherspoon, S. Matej and J.S. Karp. *Assessment of image quality with a fast fully 3D reconstruction algorithm.* In Proceedings of Nuclear Science Symposium Conference Record, volume 4, pages 2238–2242, 2001. 108

[Davison 1981] M.E. Davison. *A singular value decomposition for the radon transform in n-dimensional euclidean space.* Numerical Functional Analysis and Optimization, vol. 3, no. 3, pages 321–340, 1981. 24

[Defrise 1994] M. Defrise and R. Clack. *A cone-beam reconstruction algorithm using shift-variant filtering and cone-beam backprojection.* IEEE Trans. on Med. Im., vol. 13, pages 186–195, march 1994. 26

[Faugeras 1996] O. Faugeras and L. Robert. *What can two images tell us about a third one?* International Journal of Computer Vision, vol. 18, no. 1, pages 5–20, 1996. 52

[Federer 1969] H. Federer. Geometric measure theory. New York: Springer-Verlag, 1969. 19

[Feldkamp 1984] L.A. Feldkamp, L.C. Davis and J.W. Kress. *Pratical cone-beam algorithm.* Optical Society of America, 1984. 34

[Fessler 1989] J.A. Fessler, D. Nishimura and A. Macowski. *Model-based 3-D reconstruction of branching vessels.* In Engineering in Medicine and Biology Society, volume 2, pages 561–562, 1989. 52

[Fessler 1991] J.A. Fessler and A. Macovski. *Object-based 3-D reconstruction of arterial trees from magnetic resonance angiograms.* IEEE trans. on Med. Im., vol. 10, pages 25–39, march 1991. 52

[Garreau 1991] M. Garreau, J. L. Coatrieux, R. Collorec and C. Chardenon. *A knowledge-based approach for 3-D reconstruction and labeling of vascular networks from biplane angiographic projections.* IEEE trans. on Med. Im., vol. 10, pages 122–131, june 1991. 52, 65, 104

[Gordon 1970] R. Gordon, R. Bender and G.T. Herman. *Algebraic reconstruction techniques (ART) for three-dimensional electron microscopy and x-ray photography.* Journal of Theoretical Biology, vol. 29, pages 471–482, 1970. 111

[Grangeat 2002a] P. Grangeat. La tomographie : fondements mathématiques, imagerie microscopique et imagerie industrielle. Lavoisier, 2002. 27

[Grangeat 2002b] P. Grangeat, A. Koenig, T. Rodet and S. Bonnet. *Theoretical framework for a dynamic cone-beam reconstruction algorithm based on a dynamic particle model.* Physics in Medicine & Biology, vol. 47, no. 15, pages 2611–2625, July 2002. 42, 45, 53

[Green 1990] P.J. Green. *Bayesian reconstructions from emission tomography data using a modified EM algorithm.* IEEE Trans on Med. Im., vol. 9, no. 1, pages 84–93, march 1990. 38

[Hadamard 1902] J. Hadamard. *Sur les problèmes aux dérivées partielles et leur signification physique.* In Princeton University Bulletin, pages 49–52, 1902. 1

[Haigron 2004] P. Haigron, M.E. Bellemare, O. Acosta, C. Goskü, C. Kulik, K. Rioual and A. Lucas. *Depth-map-based scene analysis for active navigation in virtual angioscopy.* IEEE Trans. on Medical Imaging, vol. 23, no. 11, pages 1380–1390, 2004. 53

[Hansis 2007] E. Hansis, D. Schäfer, M. Grass and O. Dössel. *An iterative method for the reconstruction of the coronary arteries from rotational X-ray angiography.* In SPIE Med. Im., volume 6510, pages 651026.1–651026.10, 2007. 36, 53, 54, 105, 112, 113

[Hiroshima 2001] K. Hiroshima, R. Funakami, K. Hiratsuka, J. Nishino, T. Odaka, H. Ogura, T. Fukushima, Y. Nishimoto, M. Tanaka, H. Ito and K. Yamamoto. *Digital subtraction angiogram registration method with local distortion vectors to decrease motion artifact.* Journal of Biomedical Informatics, vol. 34, no. 3, pages 182–194, 2001. 52

[Ingle 1988] J.D.J. Ingle and S.R. Crouch. Spectrochemical analysis. Prentice Hall, Englewood Cliffs, NJ, 1988. 20

[Jacobson 2005] M.W. Jacobson and J.A. Fessler. *Fast interpolation operations in non-rigid image registration.* In J. M. Fitzpatrick and J. M. Reinhardt, editeurs, Medical Imaging 2005: Image Processing. Edited by Fitzpatrick, J. Michael; Reinhardt, Joseph M. Proceedings of the SPIE, volume 5747 of *Presented at the Society of Photo-Optical Instrumentation Engineers Conference*, pages 764–774, 2005. 63, 69

[Jacobson 2006] M.W. Jacobson. *Approaches to motion-corrected PET image reconstruction from respiratory gated projection data.* PhD thesis, The University of Michigan, Ann Arbor, MI, USA, 2006. 41, 47, 53, 63, 70

[Jandt 2007] U. Jandt, D. Schäfer, V. Rasche and M. Grass. *Automatic generation of 3D coronary artery centerlines using rotational X-ray angiography.* In SPIE Med. Im., 2007. 105

[Jin 2005] M. Jin, Y. Yang and M.N. Wernick. *Reconstruction of cardiac-gated dynamic SPECT images.* In ICIP05, volume 3, pages 752–755, 2005. 47, 48

[Kaczmarz 1937] S. Kaczmarz. *Angenäherte Auflösung von Systemen linearer Gleichungen.* Bull. Internat. Acad. Polon. Sci., pages 335–357, 1937. 36

[Katsevich 2003] A. Katsevich. *A general scheme for contructing inversion algorithms for cone beam CT.* International journal of Mathematics and Mathematical Sciences, vol. 21, pages 1305–1321, 2003. 26

[Klein 2000] G.J. Klein, B.W. Reutter and R.H. Huesman. *4D affine registration models for respiratory-gated PET.* In Nuclear Science Symposium Conference Record, IEEE, volume 2, 2000. 69

[Koller 1995] T. Koller, G. Gerig, G. Székely and D. Dettwiler. *Multiscale detection of curvilinear structures in 2-D and 3-D image data.* In Proceedings of Fifth International Conference on Computer Vision, pages 864–869, 1995. 52

[Kybic 2003] J. Kybic. *Fast parametric elastic image registration.* IEEE trans. on Im. Proc., vol. 12, no. 11, pages 1427–1442, november 2003. 69

[Lewitt 1990] R. Lewitt. *Multidimensional digital image representation using generalized Kaiser-Bessel window functions.* J. Opt. Soc. Am. A., vol. 7, pages 1834–1846, 1990. 105, 108

[Louis 1989] A.K. Louis. Inverse und schlecht gestellte Probleme. Teubner, Stuttgart, 1989. 2, 7, 35

[Louis 1990] A.K. Louis and P. Maas. *A mollifier method for linear operator equations of the first kind.* Inverse Problems, vol. 6, pages 427–440, 1990. 7

[Maes 1997] F. Maes, A. Collignon, D. Vandermeulen, G. Marchal and P. Suetens. *Multi-modality image registration by maximization of mutual information*. IEEE trans. on Med. Im., vol. 16, no. 2, pages 187–198, april 1997. 69

[Matej 1996] S. Matej and R. Lewitt. *Practical considerations for 3D image reconstruction using spherically symmetric volume elements*. IEEE Trans. on Med. Imaging, vol. 15, pages 68–78, 1996. 108

[Movassaghi 2007] B. Movassaghi, M. Grass, D. Schäfer, V. Rasche, O. Wink, G. Schoonenberg, J.Y. Chen, J. A. Garcia, B. M. Groves, J. C. Messenger and Carroll J. D. *4D coronary reconstruction based on retrospectively gated rotational angiography: first in-human results*. In SPIE Med. Im., volume 6509, 2007. 105

[Muraki 1991] S. Muraki. *Volumetric shape desciption of range data using 'Blobby Model'*. Computer Graphics, vol. 25, pages 227–235, 1991. 108

[Narayanan 2007] R. Narayanan. *Diffeomorphic transformations for automatic multi-modality image registration*. PhD thesis, University of Michigan, 2007. 62

[Nashed 1987] M.Z. Nashed. *A new approach to classification and regularization of illposed operator equations*. Engl, H.W. and C.W. Groetsch (eds.): Inverse and Ill-posed Problems. Academic Press, Orlando, pages 53–75, 1987. 3

[Natterer 1986] F. Natterer. The mathematics of computerized tomography. Wiley, Chichester, 1986. 21, 22, 23, 24, 26, 32, 33, 36

[Natterer 1999] F. Natterer. *Numerical methods in tomography*. Acta Numerica, vol. 8, pages pp. 107–142, 1999. 22

[Peckar 1998] W. Peckar, C. Schnorr and K. Rohr. *Non-nigid image registration using a parameter-free elastic model*. In British Machine Vision Conference, 1998. 69

[Pellot 1994] C.P. Pellot, A. Herment, M. Sigelle, P. Horain, H. Maitre and P. Peronneau. *A 3-D reconstruction of vascular structures from two x-ray angiograms using an adapted simulated annealing algorithm*. IEEE Trans. on Med. Im, vol. 13, pages 48–60, march 1994. 52

[Pierro 2003] A. De Pierro and M.E.B. Yamagishi. *Fast scaled gradient decomposition methods for maximum likelihood transmission tomography.* In Conference of the IEEE Engineering in Medicine and Biology Society, volume 1, pages 829–832, 2003. 105, 111, 112

[Radon 1917] J. Radon. *Über die Bestimmung von Funktionen durch ihre Integralwerte längs gewisser Mannigfaltigkeiten.* Ber. Verh. Sach. Akad., vol. 69, pages 262–277, 1917. 23

[Ramm 1996] A.G. Ramm and A.I. Katsevich. The Radon transform and local tomography. CRC Press, 1996. 34

[Rieder 2000a] A. Rieder, R Dietz and T. Schuster. *Approximate inverse meets local tomography.* Mathematical methods in the applied sciences, vol. 23, no. 15, pages 1373–1387, 2000. 34

[Rieder 2000b] A. Rieder and T. Schuster. *The approximate inverse in action with an application to computerized tomography.* SIAM J. Num. Anal., vol. 30, pages pp. 1909–1929, 2000. 10, 12, 24

[Rieder 2001] A. Rieder. *Principles of reconstruction filter design in 2D-computerized tomography.* Contemporary Mathematics, vol. 278, 2001. 30, 31

[Rieder 2003a] A. Rieder. Keine Probleme mit Inversen Problemen. Vieweg Friedr. + Sohn Ver, 2003. 7, 22, 24

[Rieder 2003b] A. Rieder and T. Schuster. *The approximate inverse in action II: convergence and stability.* Math. Comp., vol. 72, pages pp. 1399–1415, 2003. 10, 12

[Rieder 2004] A. Rieder and T. Schuster. *The approximate inverse in action III: 3D-Doppler tomography.* Numerische Mathematik, vol. 97, pages 353–378, 2004. 10, 13, 34

[Roche 1998] A. Roche, G. Malandain, X. Pennec and N. Ayache. *Multimodal image registration by maximization of the correlation Ratio.* Rapport technique 3378, INRIA, august 1998. 69

[Roux 2004] S. Roux, L. Desbat, A. Koenig and P. Grangeat. *Exact fan-beam compensated reconstruction formula for time-dependent affine deformations.* Physics in medicine & biology, vol. 49, no. 11, pages 2169–2182, 2004. 42, 45, 53

[Ruan 1993] S. Ruan. *Estimation de mouvement et reconstruction tridimensionnelles en stéréovision : application à l'angiographie biplan.* PhD thesis, Université de Rennes 1, 1993. 52

[Ruan 1994] S. Ruan, A. Bruno and J.-L. Coatrieux. *Three dimensional motion and reconstruction of coronary arteries from biplane cineangiography.* Image and Vision Computing, vol. 12, no. 2, pages 683–689, 1994. 52, 73, 104

[Rudin 1997] W. Rudin. Real and complex analysis. Masson, 1997. 3, 4

[Sabuncu 2005] M. Sabuncu and P.J. Ramadge. *Gradient based optimization of an EMST image registration function.* In Acoustics, Speech, and Signal Processing, (ICASSP apos;05). IEEE International Conference, volume 2, pages 253–256, March 2005. 69

[Schuster 2007] T. Schuster. The method of approximate inverse: theory and applications, volume 1906 of *Lecture Notes in Mathematics.* Springer-Verlag, 2007. 2, 7, 8, 9, 10

[Shechter 2002] G. Shechter, F. Devernay, E. Coste-Maniere and E. R. McVeigh. *Temporal tracking of 3D coronary arteries in projection angiograms.* In SPIE Med. Im., volume 4684, 2002. 52

[Shepp 1974] L.A. Shepp and B.F. Logan. *The Fourier reconstruction of a head section.* IEEE Trans. on Nucl. Sci., pages 21–43, 1974. 29

[Shu 2006] H.Z. Shu, J. Zhou, G.N. Han, L.M. Luo and J.-L. Coatrieux. *Image reconstruction from limited range projections using orthogonal moments.* Pattern Recognition, 2006. 35

[Smets 1990] C. Smets, F. Vandewerf, P. Suetens and A. Oosterlinck. *An expert system for the labeling and 3-D reconstruction of the coronary arteries from two projections.* Int. J. Cardiac Im., vol. 5, no. 2, pages 145–154, 1990. 52

[Smith 1977] K.T. Smith, D.C. Solmon and S.L. Wagner. *Practical and mathematical aspects of the problem of reconstructing objects from radiographs.* Bull. Amer. Math. Soc., vol. 83, pages 1227–1270, 1977. 23, 34

[Smith 1984] K. Smith. *Inversion of the X-ray transform.* SIAM-AMS Proceeding, vol. 14, pages 41–52, 1984. 34

[Tuy 1983] H.K. Tuy. *An inversion formula for cone-beam reconstruction.* SIAM Journal on Applied Mathematics, vol. 43, no. 3, pages 546–552, 1983. 26

[Venaille 1992] C. Venaille, D. Mishler and J.-L. Coatrieux. *Un algorithme peu contraint d'appariement de primitives courbes par stéréovision trinoculaire.* Rev. Technique–Thomson–CSF, vol. 24, pages 1071–1099, 1992. 104

[Wahle 1996] A. Wahle, H. Oswald and E. Fleck. *3-D heart-vessel reconstruction from biplane angiograms.* IEEE Comput. Graphic. Appl., vol. 16, no. 1, pages 65–73, 1996. 52

[Wang 2001] T.J. Wang and T.W. Sze. *The image moment method for the limited range CT image reconstruction and pattern recognition.* Pattern Recognition, vol. 34, pages 2145–2154, 2001. 35

[Wang 2004] W.L. Wang, W. Hawkins and D. Gagnon. *3D RBI-EM reconstruction with spherically-symmetric basis function for SPECT rotating slat collimator.* Physics in Medicine & Biology, vol. 49, pages 2273–2292, 2004. 108

[Wloka 1987] J. Wloka. Partial differential equations. Cambridge University Press, 1987. 5

[Xie 2004] Z. Xie and G.E. Farin. *Image registration using hierarchical B-splines.* IEEE Trans. on Visual. and Comp. Graph., vol. 10, no. 1, pages 85–94, January 2004. 63, 69

[Yang 2006] G. Yang, A. Bousse, C. Toumoulin and H. Shu. *A multiscale tracking algorithm for the coronary extraction in MSCT angiography.* In EMBS, volume 1, pages 3066–3069, 2006. 52, 59, 74, 110

[Zhou 2008] J. Zhou, A. Bousse, G. Yang, J.-J. Bellanger, L. Luo, C. Toumoulin and J.-L. Coatrieux. *A blob-based tomographic reconstruction of 3D coronary tree from rotational X-ray angiography.* In SPIE Med. Im., volume 9, pages 69132N.1–69132N.12, 2008. 53, 54, 57

List of publications

2009 *Motion Compensated Tomographic Reconstruction of Coronary Arteries in Rotational Angiography*, A. Bousse, J. Zhou, G. Yang, J.-J. Bellanger, C. Toumoulin. To appear in IEEE Transactions in Biomedical Engineering.

2008 *Motion Estimation in X-Ray Rotational Angiography Using a 3-D Deformable Coronary Tree Model*, A. Bousse, J. Zhou, G. Yang, J.-J. Bellanger, C. Toumoulin. To appear in Computer in Cardiology.

A Blob-based Tomographic Reconstruction of 3D Coronary Trees from Rotational X-ray Angiography, J. Zhou, A. Bousse, J.-J. Bellanger, L. Luo, J.-L. Coatrieux. Conference proceedings: SPIE Medical Imaging, 9 (2008), 69132N–69132N12.

2007 *A Bayesian MAP-EM Algorithm for PET Image Reconstruction Using Wavelet Transform*, J. Zhou, J.-L. Coatrieux, A. Bousse, H. Shu , L. Luo, IEEE Transactions on Nuclear Science 54, 5, Part 1 (2007), 1660–1669.

Simulation Environment for the Evaluation of 3D Coronary Tree Reconstruction Algorithms in Rotational Angiography, G. Yang , A. Bousse, C. Toumoulin, H. Shu. Conference proceedings: Annual International Conference of the IEEE Engineering in Medicine and Biology Society, 1 (2007), 4484–4487.

2006 *Coronary Extraction and Characterization in Multi-Slice Computed Tomography*, A. Bousse, C. Boldak, C. Toumoulin, G. Yang, S. Laguitton, D. Boulmier. Innovation et technologie en biologie et médecine ITBM-RBM, 27 (2006), 217–226.

Temporal Tracking of Coronaries in MSCTA by Means of 3D Geometrical Moments, S. Laguitton, C. Boldak, A. Bousse, G. Yang, C. Toumoulin. Conference proceedings: Annual International Conference of the IEEE Engineering in Medicine and Biology Society, 1 (2006), 924–7.

A Multiscale Tracking Algorithm for the Coronary Extraction in MSCT Angiography, G. Yang, A. Bousse, C. Toumoulin, H. Shu. Conference proceedings: Annual International Conference of the IEEE Engineering in Medicine and Biology Society. IEEE Engineering in Medicine and Biology Society, 1 (2006); 3066–9.

2005 *A Level Set Method for Vessel Segmentation in Coronary Angiography*, J. Brieva, E. Gonzalez, F. Gonzalez, A. Bousse, J.-J. Bellanger. Conference proceedings: Annual International Conference of the IEEE Engineering in Medicine and Biology Society, 6 (2005), 6348–51.

Abstract: This work is an application of the inverse problem theory to the motion compensated 3-D reconstruction of coronary arteries from Rot-X data. We first investigate the inverse problem in finite and infinite dimensions. For the finite-dimensional case, we focus on the tomographic inverse problem modeling, by defining the principles of a *voxel basis* and of the projection matrix, in order to obtain a matrix inverse problem formulation. We also investigate the notion of *dynamic tomography* and its related issues. Our discrete formulation, using the voxel basis, allows us to introduce any given diffeormorphism support deformation function in the matrix inverse problem formulation, provided that this deformation is *a priori* known. Our last chapter demonstrates how to estimate coronary arteries motion from ECG gated Rot-X projections, with a coronary 3-D deformable model. The motion is modeled by a B-spline model for point-matching registration. Once the motion is estimated, the tomographic reconstruction is performed at a reference cardiac state throughout a penalized least-squares optimization process including the motion, the penalty term being defined by favouring high intensity values for voxels in the neighborhood of the 3-D centrelines and low intensity values for all other voxels. This method has been tested on simulated data based on 3-D coronary centrelines previously extracted from a MSCT sequence.

Keywords: Inverse Problem, Generalized Inverse, Tomographic Reconstruction, Penalized Least-squares Optimization, Rotational X-ray Angiography, 3-D Coronary centreline, 3-D Coronary Deformable Model, Image Registration, Motion Compensation.

Résumé : Ce travail est une application de la théorie des problèmes inverses à la reconstruction 3-D des artères coronaires avec compensation du mouvement à partir de données Rot-X. Dans un premier temps nous étudions le problème inverse en dimension finie et infinie. En dimension finie nous nous concentrons sur la modélisation du problème inverse en tomographie en définissant la notion de *base de voxels* et de matrice de projection, en vue de pouvoir se ramener à une formulation matricielle du problème inverse. Nous étudions aussi la notion de *tomographie dynamique* et les problèmes qui lui sont liés. Notre formulation discrète permet grâce aux bases de voxels d'inclure n'importe quelle déformation de support étant un difféorphisme dans le problème inverse matriciel, dès lors que cette déformation est connue *a priori*. Dans le dernier chapitre, nous présentons une méthode d'estimation du mouvement utilisant les projections Rot-X synchronisées par rapport à l'ECG, basée sur un modèle déformable 3-D des artères coronaires. Le mouvement est modélisé par des fonctions B-splines. Une fois le mouvement estimé, la reconstruction tomographique à un instant de référence est effectuée par une optimisation aux moindres-carrés qui inclut le mouvement ainsi qu'un terme de pénalité qui favorise les valeurs d'intensités fortes pour les voxels au voisinage de la ligne centrale 3-D, et les faibles valeurs pour les autres. Cette méthode a été testée sur des données simulées basées sur des lignes centrales 3-D préalablement extraites de données MSCT.

Mots-clés : Problème Inverse, Inverse Généralisé, Reconstruction Tomographique, Moindres-carrés Régularisés, Angiographie Rot-X, Ligne Centrale 3-D des Artères Coronaires, Modèle déformable 3-D des Artères Coronaires, Recalage d'Image, Compensation du Mouvement.